DISSERTATIONES CHIMICAE UNIVERSITATIS TARTUENSIS
120

DISSERTATIONES CHIMICAE UNIVERSITATIS TARTUENSIS
120

ARNO RATAS

Energy storage and transfer in dosimetric luminescent materials

TARTU UNIVERSITY PRESS

Institute of Chemistry, Faculty of Science and Technology, University of Tartu, Estonia

Dissertation is accepted for the commencement of the Degree of Doctor of Philosophy in Physical and Analytical Chemistry on July 2nd, 2012 by the Doctoral Committee of the Institute of Chemistry, University of Tartu.

Supervisors: Senior Research Fellow, Dr. Mihhail Danilkin
Research Fellow, Dr. Mihkel Kerikmäe

Opponents: Academician, Professor Enn Mellikov (DSc), Director of Institute of Material Science, Tallinn University of Technology, Estonia (ennm@staff.ttu.ee)

Associate Professor Irina A. Kamenskikh (phys.-math. cand.), Optics and Spectroscopy Chair of Physics Faculty of M.V. Lomonosov Moscow State University (iak@neurok.ru)

Commencement: 31st of August 2012 in Room 1021, 14A Ravila Street, Tartu, at 14:30

This work has been /partially/ supported by Graduate School „Functional materials and technologies“ receiving funding from the European Social Fund under project 1.2.0401.09-0079 in University of Tartu, Estonia

ISSN 1406–0299
ISBN 978–9949–32–077–6 (trükis)
ISBN 978–9949–32–078–3 (pdf)

Tartu Ülikooli Kirjastus
www.tyk.ee
Tellimus nr. 372

CONTENTS

LIST OF ORIGINAL PUBLICATIONS

I. Mihkel Kerikmäe, Mikhail Danilkin, Ivar Jaek, Mare Must, Ando Ots, Lembit Pung, Eed Pärnoja, **Arno Ratas**, Viktor Seeman, Tõnu Tõnutare. OSL and TSL interrelations in $SrSO_4$:Eu. *Radiat. Meas.* **2010**, *45*, 559–561.

II. Mikhail Danilkin, Aime Lust, **Arno Ratas**, Viktor Seeman, Mihkel Kerikmäe. Afterglow kinetics and storage mechanism in CaF_2:Mn (TLD-400). *Radiat. Meas.* **2008**, *43*, 300–302.

III. Mikhail Danilkin, Mihkel Kerikmäe, Aleksei Kirillov, Aime Lust, **Arno Ratas**, Lilli Paama, and Viktor Seeman. Thermoluminescent dosimeter $Li_2B_4O_7$:Mn,Si – a false-dose problem. *Proc. Est. Acad. Sci. Chemistry*. **2006**, *55*, 123–131.

IV. Mikhail Danilkin, Ivar Jaek, Mihkel Kerikmäe, Aime Lust, Hugo Mändar, Lembit Pung, **Arno Ratas**, Viktor Seeman, Sergei Klimonsky, Vyacheslav Kuznetsov. Storage mechanism and OSL-readout possibility of $Li_2B_4O_7$:Mn (TLD-800), *Radiat. Meas.* **2010**, *45*, 562–565.

V. **Arno Ratas**, Mikhail Danilkin, Mihkel Kerikmäe, Aime Lust, Hugo Mändar, Viktor Seeman, Georg Slavin. $Li_2B_4O_7$:Mn for dosimetry applications: traps and mechanisms. *Proc. Est. Acad. Sci.,* accepted for publication.

Author's contribution

Paper I. Thermoluminescence curves measurements. Measuring the dose-dependence of the response of detectors. Data treatment, material discussion. Presentation of the material at the International Conference (15th Solid State Dosimetry Conference SSD15, Delft, the Netherlands, July 8 - 13, 2007).

Paper II. Kinetics measurements including the measuring methods developing. Model discussions and calculations according to suggested model.

Paper III. Thermoluminescence curves measurements, study of the influence of light on false-dose storage. Studies of the role of different impurities and synthesis variations. Discussion of the results and manuscript corrections.

Paper IV. Thermoluminescence curves measurements, study of the dose-dependences of the response of detectors. Data treatment, material discussion.

Paper V. Thermoluminescence curves and thermoluminescence kinetics measurements. Kinetic measurements methods development and correction. Model discussions, literature overview. Calculations according to the suggested model. Experimental material preparation for the manuscript. Manuscript corrections according to reviewer's suggestions.

INTRODUCTION

Luminescence dosimetry is a widely used means of dosimetric measurements, especially for personnel dose monitoring. The radiation energy is absorbed by a material of detector. Some part of the absorbed energy is stored in the form of radiation defects (trapped electrons and holes, radicals, displaced ions). In luminescence dosimetry, the stored energy can be released in the form of light, with the amount of light being proportional to the amount of absorbed radiation energy (absorbed radiation dose). The dosimetric information is obtained by stimulating the release of stored energy either by heating (thermally stimulated luminescence (TSL) dosimetry) or by certain quanta of light (optically stimulated luminescence (OSL) dosimetry). The OSL dosimetry is very attractive due to smaller overall dimensions of a dose-reader compared with TSL dosimetry where a heater is required. One more attractive feature of OSL readout systems is the possibility to read stored dose several times without information losses, while TSL readers clear the dose information during readout. These advantages force the studies of energy storage and release in luminescent materials: the prospective aim of investigations is to create new solid-state luminescent detectors suitable for OSL readout of dose information. To move towards the practical applications, one needs to understand the intrinsic mechanisms of phenomena involved into the basic principles of operation of the object of development. This understanding requires fundamental studies of physics and chemistry of the dosimetric luminescent materials.

Luminescent detectors of radiation should meet several requirements, such as low detection threshold and high sensitivity, the absence of information losses in time (low fading), the absence of false-dose effects due to visible light and near ultraviolet irradiation, a good linearity for dose and wide range of measurements, human tissue equivalence. The latter implies the close to that of human tissue dependence of the absorbed dose on the energy of radiation quanta (or on the energy of particles). This feature depends mostly on the effective atomic number of the material. Actually, the "ideal detector" is not known yet: all the requirements together are scarcely satisfiable within a single material. Thus, lithium tetraborate $Li_2B_4O_7$ is a tissue-equivalent material. When it is doped with either Mn or Ag (or Cu), good radiation detectors can be obtained for personnel dose monitoring. However, these detectors will not be the most sensitive compared to the detectors based on other materials. Also, the range of measurements will not be very wide. Moreover, a false-dose effects of near ultraviolet irradiation can appear in some cases. The most sensitive radiation detectors with good linearity can be made on the basis of $SrSO_4$:Eu. However, this material is not tissue-equivalent and has relatively low upper threshold of the range of measurable doses. CaF_2:Mn measures doses within an extremely wide range but cannot measure low doses with a high accuracy and is not

tissue-equivalent. The dosimetric materials mentioned above are the objects of the present study which is intended to connect the most useful properties of each material with the structural features and physics of radiation-induced processes. A topical guideline of this study is to improve the knowledges on the matter and principles of "an ideal radiation detector". Also, a special attention is paid to the OSL readout possibilities for the materials under investigation. This helps to extend the applications of the luminescent radiation detectors in the field of personnel dosimetry. Thus, the OSL systems of Landauer® are widely known on the market. However, they are based on Al_2O_3 which is not tissue-equivalent, and hence, a need of tissue-equivalent luminescent detectors with OSL readout is not yet satisfied.

The main goal of the present work is to study mechanisms of energy storage and transfer in dosimetric materials $SrSO_4$:Eu, CaF_2:Mn, $Li_2B_4O_7$:Mn in connection with their chemical, crystal, electronic, and defect structure, and also with preparation procedure features. These problems are typical for the material science of luminescent radiation detectors. By solving them, one makes the necessary steps towards creation of better materials. Also, there is a practical goal: to estimate the OSL readout prospects for the materials under investigation. To achieve the goals, both experimental and comparative investigations are undertaken. Luminescence, thermoluminescence, kinetics, optical stimulation spectra measurements, also magnetic susceptibility measurements and EPR studies, in connection with the variations of preparation procedures, compose the experimental part of the present work. The results are compared and critically analysed together with the previously published by other investigators materials, comprising an analytical, or comparative, part of the work.

OVERVIEW OF PUBLICATIONS ON THE MATERIALS UNDER INVESTIGATION

$SrSO_4$:Eu and other sulphates

Strontium sulphate is known as natural mineral celestine, the strontium analogue of barite. The crystal structure is orthorhombic (*Pbnm*). The crystal structure studies of natural minerals celestine, barite, and anglesite are published time to time, and the latest ones are aimed to estimate the influence of cation size on the structure of the SO_4 tetrahedron[1,2]. The lattice structure of $SrSO^4$ is shown in Fig. 1. The illustration is created using "balls-and-sticks" computer program[3].

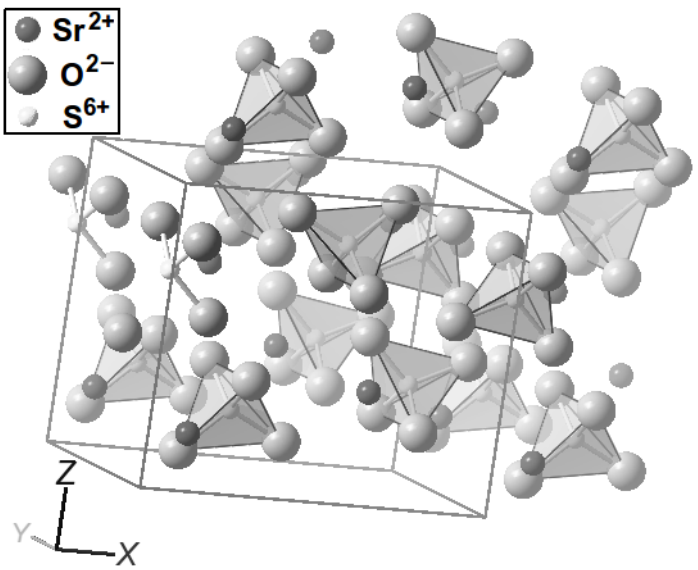

Fig. 1. Ball and stick model of strontium sulphate lattice. A unit cell is outlined with a solid-line parallelepiped. S+4O tetrahedra are marked out with semi-transparent planes. Sizes of balls are not in scale with ionic radii of atoms.

$SrSO_4$:Eu seems to be very attractive dosimetric material, especially for environmental dosimetry systems with OSL-based readout. It is transparent both for its' own luminescence and for the light necessary for optically stimulated readout, it has extremely high sensitivity, and also, it can be safely produced commercially.

Electronic band structure has been studied theoretically only for alkaline metal sulphates, including sulphates with mixed alkali cations[4]. However, the comparative experimental studies of fast intra-band luminescence help one to understand the valence band structure of alkaline-earth metal sulphates, too[5].

Valence band in sulphates is relatively wide (>7 eV[5]) and non-uniform. Density of states varies essentially, so a valence band is split into several sub-bands. However, the separation of the sub-bands is not very large: a strong temperature dependence of fast intrinsic luminescence in many sulphates shows that sub-bands become overlapped with temperature increase[5]. This feature is mostly pronounced in $SrSO_4$, where the structured luminescence bands are observed for fast luminescence only at low temperature[5]. The splitting of a valence band in $CaSO_4$ and $SrSO_4$ has even been disclaimed in the earlier work[6]. When the valence band is essentially split into the separated sub-bands, the holes are usually hardly mobilizable. This complicates the transfer of holes both to traps and to recombination centres. When the valence band is uniform and wide, the transfer of holes and excitons goes easily. However, an immediate excitation of luminescence gives a concurrent channel taking some part of energy and decreasing an amount of charge carriers stored at traps. Hence, a material with rather uniform valence band can be probably a good scintillator but not a very good storage phosphor. $SrSO_4$ has some intermediate structure of a valence band: though it is non-uniform, the sub-bands are overlapping at room temperature. This impedes the transport of holes and excitons but increases the trapping probability for the holes. A back-side of this feature appears when one tries the OSL readout of $SrSO_4$:Eu detectors[7, I]. In general, the valence band structure in $SrSO_4$ is mostly favourable for an "ideal detector".

The energy transport to luminescence centres in alkaline-earth sulphates occurs either directly by "hot" electron-hole pairs or by excitons, and also by the resonance energy transfer from self-trapped excitons[8]. Excitation of impurities to particular levels depends on their positions relative to electronic states of host material[8]. Also, the excitation efficiency is rather different for allowed and forbidden transitions. There are multiple studies of thermoluminescence mechanisms and traps in alkaline-earth sulphates[9-14]. Two different models are suggested for explaining thermoluminescence peaks[10]. The first one implies recombinations at some radiation-induced lattice defect with further energy transfer to luminescent impurity ions[9,10,15]. The other mechanism is connected with charge-transformations of an impurity ion acting as a trap for an electron[10,12,13,14]. We should note that charge-transformations of the impurity ions were observed with high radiation doses exceeding the saturation threshold for the dose-dependence of thermoluminescence response. The radiation-induced redox reactions were accompanied with creation of SO_3^-, O^-, O_3^- and other radicals[10,12,13]. Actually, the radiation-induced decomposition of a host lattice has occurred. Hence, the first mechanism (a resonance energy transfer from lattice defects to impurity ions) is preferable for practical use. This is still more important for OSL readout systems: a severe lattice damage by radiation can be recovered (when possible) only by a high-temperature annealing.

Essential information about thermoluminescence mechanisms can be obtained by EPR studies of radiation-induced defects. There are many papers

describing EPR signals and models of defects, we mention here only some of them[9,13,15–18]. The combined EPR and TSL studies are reported in paper[13]. However, the high radiation doses (self-irradiation by a radioactive impurity ^{241}Am has been used) created multiple radiation defects and resulted in partial decomposition of crystal lattice, thus complicating the recognition of the role of each particular defect in TSL. The EPR defects annealing in connection with TSL was reported in paper[9]. The models of stabilized by cation vacancies hole centres SO_4^- having high annealing temperatures (about 470 K and about 660 K) have been suggested in this paper. However, neither g-tensor values no EPR spectra are presented there. TSL and EPR of $CaSO_4$:Dy,Ag has been described in paper[15]. Ag^+ is shown to act as a hole trap centre being transformed into Ag^{2+} at irradiation and releasing a hole at high temperature (about 600–620 K). The model of recombination centre is based on decomposition of the sulphate-anions into sulphite and oxygen. It is not convincing and could be truth only for very high radiation doses. The EPR of SO_3^- radical has been studied in the natural single crystals of different alkaline-earth sulphates[16]. The samples have not been intentionally irradiated prior to EPR measurements: a dose of natural radiation was high enough in the studied minerals. The thermal decomposition of the SO_3^- radical has not been studied in the paper[16]. The detailed EPR study of radiation-induced defects in natural crystals of $BaSO_4$ and $SrSO_4$ has been undertaken later by the same researcher[17]. The samples were irradiated with very high radiation doses up to 10^6 Gy. The thermal annealing of observed EPR centres has been studied, too. The SO_4^- radicals were shown to release holes at 400 K. The holes are partially captured by the other hole traps (thermally stable SO_3^- radicals are formed), and partially undergo recombination with captured electrons. The most interesting model is given in this work for electron traps. The precursors of the electron traps are sulphate-anions near anion vacancies. With an electron being trapped, such an anion becomes a SO_4^{3-} radical. The model is proved by the measurements of angular dependences of both g-tensor and A-tensor components, using a super-hyperfine structure from the natural isotope of ^{33}S. The SO_4^{3-} radicals are annealed at about 450 K releasing the trapped electrons. The radiation defects could be cleaned also by UV-light irradiation. The latter models seem to be very useful for analysis of our data. We should mention one more EPR study of both pure $CaSO_4$ and doped $CaSO_4$:Dy,P[18]. The SO_4^- hole centres were studied and suggested for EPR-dosimetry due to a wide range of linear response to the radiation dose. There were two different centres observed, one with an orthorhombic symmetry, and another one with an axial symmetry. The axial centre has a higher thermal stability compared with that of the orthorhombic one. The axial centre is supposed to be stabilized by a cation vacancy present due to some trivalent ion impurity.

We can summarize now the most essential results of EPR studies of radiation-induced defects in sulphates. SO_4^{2-} anions can trap either holes or

electrons depending on the effective charge of the closest lattice defect. The trivalent metal impurity ions can stabilize SO_4^{3-} radicals still better than more remote anion vacancies. At the same time, these impurities require the compensation of their positive charge which can be provided by cation vacancies. Cation vacancies, in turn, cause the closest SO_4^{2-} anions to become hole traps with the increased thermal stability. Both hole and electron traps are expected to appear from different sides of a complex of a trivalent impurity ion with a cation vacancy. This arrangement is possible due to relatively large anions separating the charge-compensated pair of defects. Either exciton or correlated electron-hole pair would be efficiently captured here. When either a hole or electron is released in this complex centre, the recombination occurs at a close distance from the impurity ion. Hence, the energy transfer to the impurity ion would occur with a high probability, and the model suggested in papers[9,10,15] seems to be very reasonable.

Both Eu^{2+} and Eu^{3+} ions are detected in alkaline-earth sulphates doped with europium[11,14]. Charge transformations of europium ions are often observed at high radiation doses. However, the models of Eu^{2+} excitation when TSL occurs suggest resonance energy transfer from closely located recombination centres, while charge transformations of europium are regarded to be not connected with TSL in the luminescence band of Eu^{2+}. The redox reactions of europium has been also observed during the synthesis of the luminophors. This is essential point for our further discussions but we return to this point when discussing our own results.

The combined studies of OSL and TSL in $SrSO_4$:Eu were undertaken not so long ago[19]. The researchers measured a linearly-modulated OSL signal. The dosimetric TSL peak and the spectral composition of that peak are the same as in our studies. The researchers suggested two different types of traps being involved in OSL on a basis of the different thermal annealing of two different linearly-modulated OSL components observed in their experiments. The response to a radiation dose of both TSL and OSL demonstrated, however, the same behaviour, with a linear range of both dependences being about 10^2 Gy. The details of energy storage and transfer have not been discussed in this work[19].

Several papers on the studies of $SrSO_4:Sm^{3+}$ thermoluminescent material have been appeared recently[20,21]. The papers are concerning the synthesis of the material and the influence of the preparation conditions on the luminescence properties and on the size of the microcrystals. The thermoluminescence mechanisms are not discussed by the researchers.

CaF_2:Mn as a thermoluminescent material

Calcium fluoride has a cubic face-centered lattice with space group Fm3m and a = b = c = 5.4323 Å. Each Ca^{2+} ion has 8 equidistant F^- neighbours, at the corners of a cube; each F^- ion has 4 equidistant Ca^{2+}

neighbours, at the vertices of a regular tetrahedron (see Fig. 2, the illustration have been created with "balls-and-sticks" computer program[3]). The unit cell of the material is most easily described as a simple cubic lattice formed by the F^- ions where a Ca^{2+} ion is contained in every second cube. The remaining empty cubes (called interstitial or hollow sites) are important for defect formation and diffusion .

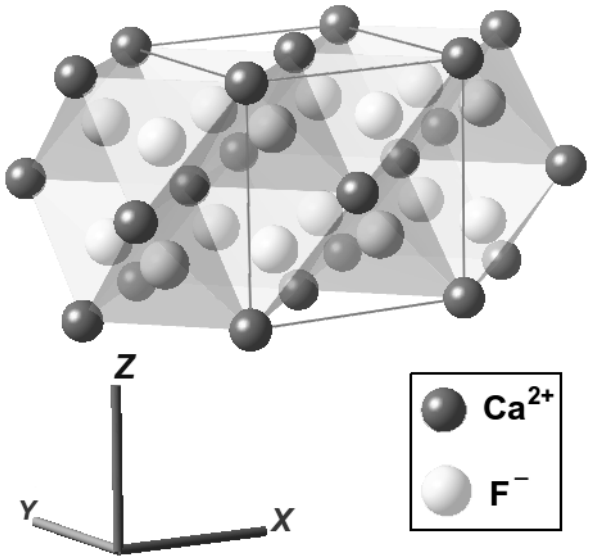

Fig. 2. Ball and stick model of calcium fluoride lattice. A unit cell is outlined with a solid-line parallelepiped. Structural elements are marked out with semi-transparent planes. Sizes of balls are not in scale with ionic radii of atoms.

There are multiple calculations of the electronic structure of CaF_2, however, the correspondence between calculations and experimental data were always desired to be better. We mention here the *ab initio* calculations[22,23] performed recently on the basis of different combined methods. The first one[22] gives a band gap value very close to that obtained experimentally[24], while the second one[23] deals with the larger clusters, and considers the relaxation effects around the calculated defects, though underestimates the band gap value. The both works report the calculations of the energy necessary to create the F-centre (an anion vacancy with a captured electron inside), with the second dealing also with the H-centre (an interstitial fluorine joined with a regular anion into a molecular structure). The result of first calculation gives the energy of 7.87 eV for the F-centre formation[22]. The second calculation considers both lattice relaxations and creation of F-centre and H-centre together[23] yielding the value of 8.17 eV. The both values are well below the band gap (the experimentally estimated band gap is 12.1 eV for direct and 11.8 eV for indirect transitions[24]). This means that the relaxation of elementary excitations in CaF_2 may easily result in fluorine displacement from a regular position. This is experimentally observable, so the

results of calculations[22,23] are rather realistic. The obtained valence band width of 2-2.5 eV is also close to the experimental estimation. Relatively narrow valence band puts some limits on the range of hole transport during their thermalisation. However, there is a particular mechanism of hole transport in CaF_2. The holes in CaF_2 can trapped in the form of different molecular entities. One of them is named V_k centre: two neighbouring fluorine ions from regular sites are shifted towards each other having lost one electron and used the remained common electron to bind one another. V_k centre is also referred to as a "self-trapped hole". *H*-centre is another kind of hole centre: an interstitial fluorine is joint into a molecular entity with a regular anion using a single common electron for binding. Both hole centres are stable at low temperatures, having a possibility to move when the metastable bond breaks and re-arranges with the other regular fluorine ion. In case of *H*-centres, an interstitial fluorine also can be transported by substitutional diffusion. The dynamics of these charged centres in fluorides has been studied many years ago, with the activation energies for the transport of the defects being well-determined[25]. These activation energies are relatively low in pure undoped crystals, and the transport occurs even below room temperature. Both a small width of valence band and "slightly impeded" transport of charge carriers favour the capture of the charge carriers in the vicinity of impurity ions, making CaF_2 a suitable host to create storage luminophors for dosimetric applications.

The studies of CaF_2-based luminescent materials have a long history being spread to several branches. Besides dosimetric applications, CaF_2 doped with both manganese and rare earth ions have been investigated as a model object to study the resonance energy transfer between impurity ions[26-28]. Ce^{3+}–Mn^{2+} and Eu^{2+}–Mn^{2+} energy transfer pairs were studied by different approaches. It is essential to note that the observed resonance energy transfer implies closely spaced pairs being formed regardless to very low concentrations of impurities. At the same time, the thermoluminescence study of CaF_2 doped with Ce and Mn has not revealed energy transfer but rather a concurrence between impurities in the energy storage and distribution[29]. The formation of small clusters of impurities is not a random process in CaF_2. The ordered aggregation was demonstrated for Eu^{3+} and Er^{3+} in CaF_2 by a high-resolution optical spectroscopy[30-32]. The mechanism suggested for ordered clusterization is based on the CaF_2 lattice restructuring in that way which performs charge compensation without a large excess of fluorine. Indeed, the compensation by interstitial negatively charged fluorine has some reasonable concentration limits. When the amount of a trivalent impurity exceeds the possible limits of fluorine stoichiometry disbalance, the other charge-compensation mechanism appears on the scene. This mechanism is based on the ordered arrangement of three groups of defects: the displaced from regular sites into interstitial positions fluorine ions, the corresponding to them fluorine vacancies, and the trivalent impurities. The pattern looks like there were a new crystal structure appeared

and started to grow inside the lattice of CaF_2. This mechanism is proved by very thorough spectroscopic analysis[30-32], and we shall remember it in further discussions.

The thermoluminescence mechanisms in CaF_2:Mn are studied for about half a century. On the one hand, this material is very valuable for thermoluminescent dosimetry. The dose-response linearity in extra wide range[33,34] makes it one of the best materials in environmental dosimetry, being suitable both for routine investigations and for radiation accidents. On the other hand, the energy storage mechanisms are not so easy in this material to catch them at a glance[35]. The low-temperature investigations of CaF_2 doped with either Mn or other 3d transition metal ions (in some cases, with rare-earth ions, too) have included luminescence, radiation-induced absorption and TSL studies[36-40]. The idea of Mn^+ formation due to electron capturing by Mn^{2+} has been suggested in these studies. However, the Mn^+ is not stable at room temperature, and cannot account for the high-temperature dosimetric TSL peaks. Thoroughly measured room-temperature and low-temperature absorption spectra in CaF_2:Mn with different Mn concentrations helped to do the next step. The spectra were measured either before or after γ-irradiation[41,42]. The annealing temperatures of radiation-induced bands have been compared with the dosimetric TSL maxima. The radiation-induced changes in the Mn^{2+} absorption and excitation bands have been accounted for by a radiation-induced F-centre in the close vicinity of Mn^{2+}. The observed evidences are, however, indirect and allow two different explanations[42]. If the observed enhanced transitions are correctly attributed to Mn^{2+}, then the oscillator strength would be increased by a factor of about 10^3 after γ-irradiation. This effect is known to be caused by spin-exchange interaction of Mn^{2+} with some closely situated defect, most usually with F-centre. The authors suggest also alternative explanation: the enhanced optical transitions belong to the perturbed F-centre which is created in the vicinity of Mn^{2+}. The both given explanations turn to the same structure of defect: closely spaced to Mn^{2+} anion vacancy containing an electron. Thermoluminescence occurs when a removed fluorine atom returns back to a regular position near Mn^{2+}, and the energy of this ionic recombination is transferred to Mn^{2+} driving it to the ${}^4T_{1g}$ (${}^4G$) excited state. Radiative transition of excited Mn^{2+} to the ${}^6A_{1g}$ (${}^6S$) ground state yields the luminescence[42]. As we shall see below, this model is very realistic in the part concerning the process of energy release. So, one would ask how the energy is stored. First, we are to explain how the F-centres are created near Mn^{2+}. Second, we are to suggest a very stable lattice defect keeping the removed from regular position fluorine up to a relatively high temperature of dosimetric TSL maximum. The first question can be answered on the basis of published experimental results of other researchers, while the second one will require also the analysis of our own data.

Some general ideas of how the energy is transferred to Mn^{2+} have been formulated in the work reporting the photoluminescence studies of a set of

CaF_2:Mn samples with different Mn concentrations[43]. The direct absorption or reabsorption mechanisms are rejected due to the low oscillator strengths of transitions in Mn^{2+} ions . Direct impact of mobile excitons is rejected due the repelling deformation potential existing around Mn^{2+} ions (Mn^{2+} is smaller than Ca^{2+} which position it occupies). The same reason is given against the hole transfer to Mn^{2+}. Only two favourable mechanisms have been suggested. First, a resonance excitation by energy transfer from the intrinsic recombinations in the lattice. Second, the capture of an electron with transformation into Mn^{+} and subsequent recombination with a hole. The latter mechanism is not suitable for processes above 200 K as the Mn^{+} centres do not survive above that temperature. What concerns a resonance excitation of Mn^{2+}, it could be involved in the first stage of energy storage, taking into account the higher excited states of Mn^{2+}. Transitions from the ground state sub-levels to the excited level ^6D ($3d^4 4s$) are responsible for the excitation bands near 7.9 and 8.6 eV[43]. The excitation of Mn^{2+} to the ^6D ($3d^4 4s$) level could occur by either excitons or electron-hole pairs during thermalisation, before they relax to a self-trapped state. In such case, the repelling deformation barrier around Mn^{2+} would not be an obstacle. The excited Mn^{2+} ion is larger compared to that in the ground state. The excitation and subsequent deactivation of the excited Mn^{2+} would very likely cause the displacement of one of the nearest fluorine atoms to an interstitial position instead of the luminescence. If the CaF_2 lattice is non-uniformly distorted due to clusterization of Mn impurity, one would expect the displacement of a certain fluorine atom to the direction where some more free space exists due to lattice distortions. The energy required for creation of a pair of F-centre and interstitial fluorine is expected to be somewhat smaller in case of a distorted lattice, however, the calculated value of 8.17 eV seems to be low enough to be released near Mn^{2+} by the suggested mechanism. We have now an idea how the close pair of Mn^{2+} and F-centre could be created under excitation. At the next stage, this removed from a regular site fluorine atom should be captured somewhere. To approach this question, let us speak about lattice distortions and their nature.

The Mn^{2+}–F^{-} distances in CaF_2 lattice have been studied both experimentally[44,45] and by *ab initio* calculations[46]. The EPR studies of Mn^{2+} in different fluoride lattices make possible to estimate the distances and character of bonds around Mn^{2+} impurity by hyperfine interactions, namely, by the values of corresponding constants[44]. The local distortions of CaF_2 lattice around Mn^{2+} are expected to account for the EPR data. The EXAFS (Extended X-Ray Absorption Fine Structure) and XANES (X-ray Absorption Near Edge Structure) studies of CaF_2:Mn have revealed the disordering and essential lattice distortions around the Mn^{2+} impurity[45]. The results of *ab initio* cluster calculations[46] have been compared with the experimental EXAFS-XANES studies[45] showing a good correlation of the calculated and experimental data. A significant lattice distortion accompanied with contraction of the closest to Mn^{2+}

F^- ions have been observed by different methods and approaches. The reason of this behaviour of Mn^{2+} in CaF_2 consists in a tendency of Mn to make rather covalent bonds with fluorine in contrast to ionic character of bonds in CaF_2. The local distortions around Mn impurity manifest themselves even as an overall CaF_2 lattice contraction. X-ray diffraction analysis of a set of CaF_2:Mn samples[47] has revealed a systematic decrease of the lattice constant with the increase of the amount of Mn in CaF_2. The TSL curves observed for the same set of samples consist of several peaks[47]. With the increase of Mn amount, the low-temperature peaks were steadily diminished in favour of high-temperature ones. At certain optimum concentration of Mn (about 2.5 m%), there is almost a single TSL peak with a maximum at about 580 K. The lattice constant diminishing correlates with the shift of TSL maxima towards higher temperatures. In the light of previous analysis, the removed at irradiation from a regular site fluorine should be trapped better when the lattice distortions are more pronounced. This will be a starting point for the further analysis based on our experimental data. We shall return to this point when discussing our results.

The OSL and PTTL (photo-transferred thermoluminescence) studies of CaF_2:Mn have revealed the stimulation bands in the UV region with the maximum near 280-300 nm[48]. The UV-irradiation of the sample at 280 nm after TSL readout (annealed up to 670 K) has partially restored the dosimetric TSL maximum near 550 K, making it more uniform. The OSL signal has been measured without special precautions to separate the directly excited luminescence of Mn^{2+} and the recombination-related afterglow. The OSL stimulation efficiency spectra for some known thermoluminescent materials have been measured[49], with the time-resolved separation of afterglow in case of CaF_2:Mn. The maximum of stimulation efficiency has been obtained near 270-280 nm. There are no appropriate models given in these studies to connect the mechanisms of energy release with observed OSL features.

$Li_2B_4O_7$:Mn as a thermoluminescent material

The effective atomic number of lithium tetraborate (Z_{eff} = 7.39) is very close to that of human tissue (Zeff = 7.42). By tissue-equivalence, lithium tetraborate is one of the best among all known host materials for luminescence dosimetry. The variation of response with radiation energy was studied for different detectors both experimentally[50–52] and and by Monte-Carlo simulation[53]. Due to a low effective atomic number, the response of $Li_2B_4O_7$ demonstrates almost energy-independent behaviour (Fig.1 in paper[53]), a similar to behaviour of water.

Hence, it would be a very attractive idea to try the OSL readout with radiation detectors based on lithium tetraborate. This explains the increased amount of efforts to study lithium tetraborate, both doped single crystals and $Li_2B_4O_7$ ceramic-based thermoluminescent detectors. Besides applications in luminescent dosimetry, $Li_2B_4O_7$ is studied also as optical non-linear crystal[55].

Lithium tetraborate has tetragonal body centered unit cell with cell parameters a=0.9475 nm and c=1.0283 nm[54]. There are eight formula units ($Li_2B_4O_7$) in the unit cell and seven atoms in the asymmetric unit: one lithium (Li), two different borons (B1 and B2) and four oxygen atoms (O1, O2, O3 and O4). The space group I41cd generates total of 104 atoms in one unit cell: 16 Li, 16 B1, 16 B2, 16 O1, 16 O2, 16 O3 and 8 O4. By looking the B - O coordination, two type of polyhedral structure elements can be distinguished in the structure: triangles and tetrahedra. All B1 belong to triangles (coordinated by O1, O2 and O3) and all B2 are tetrahedrally coordinated with oxygen atoms. The bridging oxygen between two B + 4O groups is always O4. The lattice structure of lithium tetraborate is illustrated in Fig. 3 created using "balls-and-sticks" computer program[3].

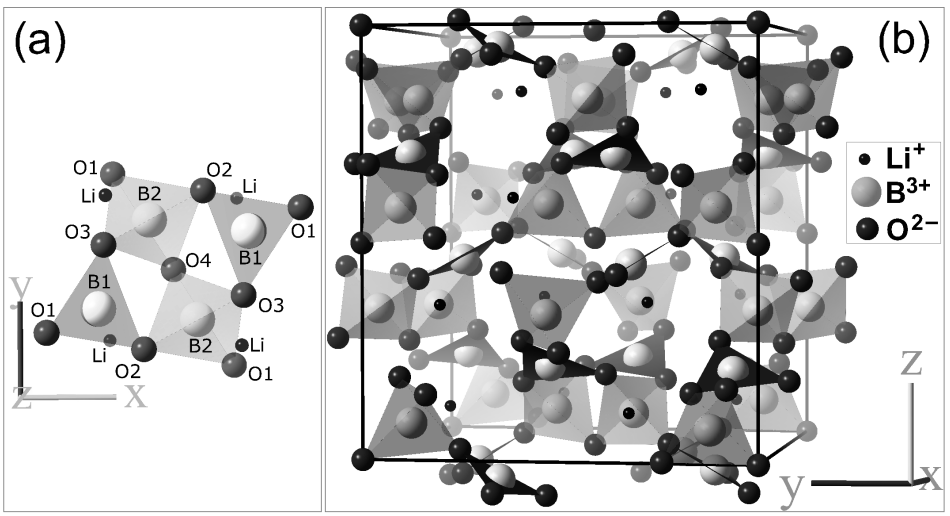

Fig. 3. **(a)** Main crystal motif of lithium tetraborate consisting of two basic elements: two identical planar trigonal (B1+O1+O2+O3) and two identical tetrahedral (B2+O1+O2+O3+O4) groups. Tetrahedral groups have a common vertex O4 and are joined additionally by planar boron-oxygen triangles. Li ions are located in the interstices of boron-oxygen framework. **(b)** Ball and stick model of lithium tetraborate lattice. A unit cell is outlined with a solid-line parallelepiped. Basic elements (B+4O tetrahedra and B+3O triangles) are marked out with semi-transparent planes. Sizes of balls are not in scale with ionic radii of atoms.

It is common to describe the main crystal motif (Fig.3(a)) of lithium tetraborate as a boron-oxygen complex (4B + 9O), consisting of two identical planar trigonal (B + 3O) and two identical tetrahedral (B + 4O) groups. There are total of eight boron-oxygen complexes in the unit cell. The lithium ions stabilize the boron-oxygen framework being distributed in helicoidal voids spreading along the z-axis.

$Li_2B_4O_7$ electronic structure has been also studied extensively, the previous calculations being refined and verified experimentally[56–60]. These studies

elucidated the structure of energetic bands. $Li_2B_4O_7$ has a wide band gap (9 to 10 eV) and structured valence band built up of three sub-bands. Valence band structure implies "heavy" and hardly mobilizable holes. This fact will be important for our further analysis of the features of TSL kinetics and OSL.

Results of a comprehensive EPR and ENDOR study of the trapping centres in undoped $Li_2B_4O_7$ single crystals have been published recently[61]. The samples with both natural and artificial isotopic composition were used for better identification of hyperfine structures and models of paramagnetic centres. The Li vacancy was shown to stabilize a hole at the "bridging" oxygen (a common vertex of two BO_4 tetrahedra, O4 in Fig.3(a)). A hole captured at "bridging oxygen" have demonstrated that it "has nearly equal hyperfine interactions with two adjacent boron nuclei", with the two close sets of lines having yet been distinguished[61]. On our opinion, the small difference between two initially equal B2 - O4 distances have been observed due to the presence of a Li vacancy near one of the two adjacent tetrahedral units. It causes either deformation of one of two adjacent tetrahedra or their orientation displacement. All tetrahedral groups are usually considered to be structurally identical, which is obviously true for the perfect crystal but easily turns wrong in the presence of either intrinsic or impurity lattice defects. Electrons were found to be trapped at boron ions near oxygen vacancies[61]. The holes are shown to leave trapping centres at low temperatures: the corresponding paramagnetic centres do not survive above 90 K[61]. The high-temperature TSL is possible only when impurities are involved in processes.

To make a TLD material, $Li_2B_4O_7$ is usually doped with either Mn or Cu (or Ag). EPR and luminescence of $Li_2B_4O_7$:Cu single crystals have been studied recently[62–64]. Cu^{2+} has been observed by EPR, while Cu^{+} was detected by luminescence. The position of Cu^{2+} in the lattice of $Li_2B_4O_7$ has been deduced from EPR. It has a low symmetry, and should be incorporated close to a regular Li^{+} position but with a distorted surroundings due to displacement of large Cu^{2+} from a regular Li^{+} site. Cu^{+} studied by luminescence has a stronger displacement but causally somewhat a higher symmetry. EPR and optical studies of γ-irradiated $Li_2B_4O_7$:Mn, both single crystals and glass, have revealed different Mn centres[65]. The interpretation of obtained results[65] is not so obvious, however. Also, the high radiation dose (50 kGy) given to sample caused the recharging of Mn and essential radiation damage. Radiation-induced absorption and photoluminescence were studied in $Li_2B_4O_7$:Mn and $Li_2B_4O_7$:Ag single crystals[66]. Very similar radiation-induced bands for $Li_2B_4O_7$:Mn single crystals were observed also in the other work[67]. The samples were given a radiation dose either of 12 kGy with a high-energy (4 MeV) electron beam[66] or γ-radiation dose of 120 kGy[67]. Again, the applied dose was high enough to cause $Mn^{2+} \rightarrow Mn^{3+}$ transformation. Hence, some of the observed radiation-induced absorption bands were connected with manganese transformations at high doses and are not suitable for OSL readout in regular cases.

The TSL (including luminescence spectral composition) was investigated for both $Li_2B_4O_7$:Mn single crystals and glassy samples with different radiation doses and different amounts of added Mn[68]. Reasonable X-ray doses of 1-60 Gy have been used in this work. Two different but very close Mn^{2+} emissions (608 ± 2 and 598 ± 2 nm) were registered for different TSL maxima, with no dependence on radiation dose. The TSL shows practically identical features for crystals with different amount of manganese, but changes drastically in glass samples[68].

The decrease of Mn^{2+} amount (estimated by EPR) at high radiation doses has been demonstrated in our studies [IV.]. At the same time, the amount of Mn^{2+} has been found to be unchanged at doses up to 1-2 kGy. We have studied also X-ray radiation-induced optical absorption and have shown the decrease of dosimetric TSL peak after optical stimulation at 365 nm [IV.]. This fact demonstrates a principal possibility of OSL readout for $Li_2B_4O_7$-based detectors. Recently, both TSL and OSL in $Li_2B_4O_7$:Cu,Ag single crystals have been studied[69]. Despite of using high-quality transparent single crystals, the minimum detectable dose with OSL readout was found to be only about 100 mGy, while 1000 times better value of 0.1 mGy occurred for TSL readout[69]. This fact clearly demonstrates that moving from a principal possibility to practical applications requires to answer several questions. We deal with $Li_2B_4O_7$:Mn trying to answer two of them: What is the storage mechanism of excitation energy in $Li_2B_4O_7$:Mn? How the OSL readout efficiency can be improved? The first question have been already touched in our paper [IV.], and it will be considered once again. What concerns the improvement of readout, $Li_2B_4O_7$:Mn has been modified by doping it with beryllium (patent pending[70]). This modification has opened new approaches, and also initiated the next round of investigations. We shall compare EPR, TSL, kinetics, radiation-induced absorption and OSL stimulation spectra in $Li_2B_4O_7$:Mn and $Li_2B_4O_7$:Mn,Be. The comparative studies help one to apprehend the nature of traps and energy storage mechanisms in these materials.

EXPERIMENTAL

Preparation of materials

Strontium sulphate was obtained by the exchange reaction:

$$2NH_4^+ + SO_4^{2-} + Sr^{2+} + 2NO_3^- = SrSO_4 + 2NH_4^+ + 2NO_3^-$$

The initial solutions were prepared from "pure" grade materials, with the residual impurities having been extracted from the initial solutions by a 8-hydroxyquinoline solution in chloroform prior to sulphate sedimentation . $SrSO_4$ sedimentation was performed at an increased temperature (350–365 K) from an acid mother liquor containing sulphate anions. Eu_2O_3 was dissolved in a hot sulphuric acid and added to a solution before the strontium nitrate adding by a peristaltic pump. The reaction was controlled by adding solutions of both reagents, strontium nitrate and ammonium sulphate, with two independent peristaltic pumps. The precipitate was washed with quartz water and decanted. After drying, the samples were annealed at 1343 K for 1 h under the flowing argon. Typically, the amount of added Eu was 1 mol%. However, the amount of Eu^{2+} entering the $SrSO_4$ lattice depends strongly on synthesis conditions (temperature, concentrations and adding rate of reagent solutions, etc.). To avoid the casual effects, all the TSL and OSL studies were performed using the samples obtained from the same precipitate. Yet for magnetic susceptibility measurements, a set of samples was prepared with different Eu concentrations in the initial solution.

Calcium fluoride was precipitated from solution:

$$Ca^{2+} + 2F^- = CaF_2$$

The co-precipitation of the host material CaF_2 together with MnF_2 was carried out in a specially designed apparatus made of fluoroplast-4. All the initial compounds were of special purity. HF contained less than $1x10^{-5}$ % of heavy and transition metals. $CaCl_2$ contained less than $1x10^{-5}$ % of Al, Cu, Ag, Fe, Mn, Mg, less than $1x10^{-3}$ % of Ba and Sr, and less than $1x10^{-4}$ % of Pb, Bi, Cr, Si. Triply distilled water was used to prepare solutions and mother liquor. Dilute solutions of $CaCl_2$, $MnCl_2$ and HF were added simultaneously at a regulated rate into the reaction vessel using peristaltic pumps. The reaction vessel was kept at an elevated temperature by means of a vapour bath, and the incoming solutions were agitated with a fluoroplast-made stirring rod. The precipitate was aged in the mother solution for 2–3 h. Then the precipitate was decanted and washed carefully, dried, and pre-annealed in air at 673 K for 2 h to remove the traces of water and fluoric acid. Traces of water cause oxidation of Mn^{2+} as well as oxygen traces. To prevent Mn^{2+} from oxidising, the starting materials should be also free of oxygen ($Ca(NO_3)_2$ cannot be used instead of $CaCl_2$). Pre-annealed precipitate was then placed in carbon-glass crucible and fired for 1/2 h at 1423 K in a quartz atmospheric tube under a protective flow of

high-purity (99.999%) argon or nitrogen. When necessary, the finished thermoluminophor was pressed into tablets and fired in a protective atmosphere once again. The resulting concentration of manganese in the finished thermoluminophor depends on the precipitation conditions and on the presence of additional dopants. The excess of F^- ions and a longer ageing time increase the amount of co-precipitated manganese. In order to obtain a co-precipitate of CaF_2–MnF_2 in the form of fine microscopic crystals, one should add the solutions into the reaction vessel very slowly. The most suitable rates of adding solutions were the following: $CaCl_2$ —2.5 ml/min, HF —2.8 ml/min. Ageing time of 2 h appears to be sufficient, as the amount of manganese in the co-precipitate does not increase when the ageing time is increased above 2 h. The optimum concentration of the manganese in the co-precipitated precursor is found to be about 2.1–2.5 mol%. It decreases only slightly after the final firing of the precursor. The real concentrations of Mn were assessed by different analytical methods[47,71], however, the charge states of Mn could be estimated only by measuring magnetic susceptibility (see below). According to these estimations, both Mn^{2+} and Mn^{3+} occur in the obtained material.

Initial lithium tetraborate was obtained by the following reaction:

$$\mathbf{Li_2CO_3 + 4H_3BO_3 = Li_2B_4O_7 + 6H_2O + CO_2}$$

Typical Mn concentration was 0.13–0.26 mol.%. Be concentration was either the same or twice of Mn amount. Manganese carbonate was added at the stage of initial synthesis in water suspension at continuous stirring and heating the mixture. In case of $Li_2B_4O_7$:Mn,Be samples, BeO was added at the same moment as manganese. The water was evaporated completely, and then the residual water and CO_2 were removed by heating at 823 K for 120 minutes under flowing nitrogen. Then, the luminophor was ground in a mortar, and tablets were pressed. The sets of tablets were sintered at different temperatures (1133-1213 K). This procedure resulted in the ceramic samples of $Li_2B_4O_7$:Mn and $Li_2B_4O_7$:Mn,Be. According to XRPD, the samples contain a well-formed crystalline phase. Small crystals are bound together with a glassy phase. The amount of binding glassy phase, however, is very small compared to the amount of polycrystalline material. Several samples were prepared with $KMnO_4$ instead of manganese carbonate. The amount of Mn^{2+} was estimated both by EPR and by measuring magnetic susceptibility of the samples.

Experimental techniques

X-ray powder diffraction (XRPD) method was used for crystal phase analysis and cell parameter determination. XRPD pattern was obtained using a computer-controlled Bragg–Brentano Θ–2Θ powder diffractometer (equipped with a goniometer GUR-5 from diffractometer DRON-1). It has a 180 mm radius and works at 40 kV (20 mA) with *CuKα* (λ=1.5405981 Å) radiation collimated with Soller slits (aperture 2.5˚) and a 1 mm

divergence slit. Soller slits (aperture 1.5˚) were also used in the diffracted beam. A 0.03 mm Ni filter, a 0.25 mm receiving slit and a scintillation detector were used in the step-scanning mode (5 s for each step of 0.02˚2Θ) in the angular range of 8–160˚2Θ. A software system AXES[72] was used to treat raw data (peak detection, fitting with pseudo-Voigt function and cell refinement). For cell refinement, an independent zero angle correction was made and applied to the diffraction angle. Rietveld analysis (computer program FULLPROF[73]) was used to determine the lattice stoichiometry.

TSL curves and kinetics were measured with a home-made TSL reader based on computer-driven thermocontroller OMRON E5CK and PMT FEU-79 equipped with a current-to-frequency converter. The measurements were controlled through a WEB-interface. Measured data were automatically collected and stored at data server. Data statistical refinement and pre-treatment were carried out by a special computer program, written for this particular installation. Typically, the low heating rates of 0.25–0.5 K/s were used.

Decay curves (kinetics) and TSL curves were measured after excitation either with $^{90}Sr/^{90}Y$ β-particles (0.23–0.46 Gy for CaF_2:Mn; 0.12–1.2 Gy for $SrSO_4$:Eu) or with ^{239}Pu α-particles (0.74–7.4 Gy for $Li_2B_4O_7$:Mn ; 0.74–4.43 Gy for $Li_2B_4O_7$:Mn,Be). The kinetics measurements were performed after cleaning the low-temperature peaks (pre-heating 60 s at 523–533 K for CaF_2:Mn, 100 s at 395 K for $Li_2B_4O_7$:Mn, and 240 s at 464 K for $Li_2B_4O_7$:Mn,Be). After pre-heating, the sample was removed from heater surface. Then heater temperature was increased to the desired value, and only after that the sample was placed back onto a heater to measure decay kinetics. The data collected before thermal equilibrium achieved were not used in further analysis. This technique is applicable when the non-equilibrium state lasts less than the time-constant of a fastest decay, and the total time of measurements exceeds 4–5 times the time- constant of a slowest decay exponent.

Spectral composition of the thermoluminescence peaks was measured for $Li_2B_4O_7$:Mn with an optical spectrometer Newport OSM2-100DUV. The spectrometer is equipped with an optical wave-guide. The spectrum in selected range was recorded with a CCD array for known period of time (up to 1 minute). The data were transferred to a computer and corrected for spectral and amplitude sensitivity of CCD elements. During the measurements, the sample was kept at temperature about 660–680 K using an electric heater.

The samples were irradiated either with a first-class ^{239}Pu radiation source (6.02×10^5 α-particles per second, dose rate about 1.23 mGy/s for a 4.5-mm tablet) or with a $^{90}Sr/^{90}Y$ radiation source 6527B (Sweden, about 3 mGy per rotation). Also, an X-ray tube with a tungsten anode (53 kV, 15 mA, dose rate about 32 Gy/s/cm^2) has been used for both dose-dependence measurements and EPR studies.

The optical measurements were performed with a computer-driven double monochromator MChD-2 (LUMEX, Russia, spectral resolution 0.28 nm),

equipped with PMT HAMAMATSU R7400U-04, pre-amplifier and voltmeter with a computer-driven data acquisition system. The luminescence of Eu^{2+} in $SrSO_4$ was excited with a Seoul Optodevice UV LED T9B28C (280 nm, 0.6 mW of optical power). Radiation-induced optical absorption bands were obtained by measuring diffuse reflectance spectra before and after X-irradiation. The spectra were recorded at least twice, then averaged. Absorption bands were extracted by dividing the spectrum of X-irradiated sample by the spectrum measured before X-irradiation. The halogen incandescent lamp Narva 55133 HLWS5 was used as a light source for diffuse reflectance measurements. It was powered by a regulated-voltage stabilized source. The lamp was forced up to 28 W to obtain more light in a UV-region.

Optical depopulation of traps was studied at three different wavelengths using three powerful LEDs: LED LUXEON III STAR LXHL- LB3C (peak emission at 470 nm, about 500 mW of optical power, used for $SrSO_4$:Eu), LED HEXAGON H2A1-H365 (365 nm, 25 mW of optical power, used for $Li_2B_4O_7$:Mn), and LED HEXAGON H2A1-H395 (395 nm, 95 mW of optical power, used for $Li_2B_4O_7$:Mn,Be). The LEDs were powered by specially designed stabilized-current source with automatic selection of working current for each particular LED.

OSL spectra were measured using a 1000 W Xenon-arc lamp combined with the quartz monochromator SF-4 equipped with optical filters. The integrated emission was measured by PMT (FEU-39) with a quartz window. Two shutters were installed to separate the excitation and measuring periods of time: the first one at the entrance of monochromator, and the second one in front of the PMT. The latter opens automatically 0.05 s after the first shutter has been closed. The "dark" pause of 0.05 s was selected to separate the stimulated recombination luminescence from the directly excited one (intra-centre processes have a decay time of 10^{-5}–10^{-8} s). Thermal destruction of the OSL signal was studied by a pulse-step annealing, with a temperature of the pre-excited sample being rapidly raised to a desired temperature point, then the sample kept at that point for time of 2 min, and after that quickly cooled down to room temperature to measure the OSL intensity.

EPR measurements were performed both at room temperature and at liquid nitrogen temperature, using an X-band (9.1 GHz) spectrometer with a 975 kHz magnetic field modulation. The signals of a sample-holder and quartz dewar flask were subtracted from EPR spectra of Mn^{2+} in $Li_2B_4O_7$. The measurements conditions (microwave power, magnetic field modulation amplitude) were optimized to observe either Eu^{2+} (in $SrSO_4$) or Mn^{2+} (in $Li_2B_4O_7$).

Magnetic susceptibility of samples was studied using the quantum magnetometer equipped with a superconductive magnet and a superconductive screen (Physics Chair of D. Mendeleev University of Chemical Technology of Russia). The thermal insulation of sample from liquid He environment makes the measurements possible in a wide range of temperatures (2–350 K).

RESULTS AND DISCUSSION

$SrSO_4$:Eu

The dose-dependence of the area under the TSL curve shows a very-close-to-linear behaviour[I.] (see Fig. 4). However, a saturation occurs at doses as low as

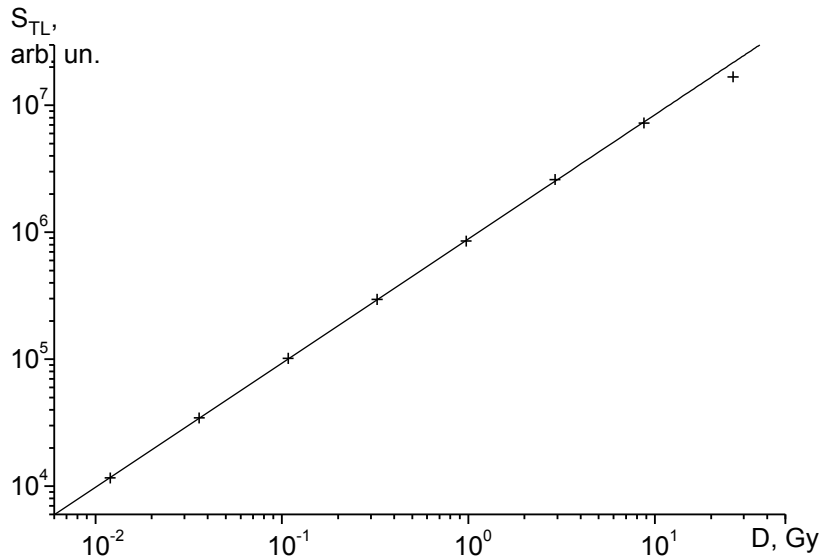

Fig. 4. The dose-dependence of the area under a TSL curve can be approximated by function $S = 8.88x10^5xD^{0.978}$. Sublinearity at low doses is almost negligible. However, a saturation is observed at doses higher than 20 Gy. The sample was irradiated using a $^{90}Sr/^{90}Y$ radiation source with a relatively small dose rate (about 0.01 Gy/s).

tens of Gray. This means probably that the traps of one kind only are becoming saturated, for example, the electron traps located somewhere in the vicinity of Eu^{2+}. The amount of trapped holes is restricted by the charge balance only: the hole centres are directly created by high-energy radiation trough ionizing SO_4^{2-} anions (see the EPR data below). The idea of limited number of electron traps and limited number of Eu^{2+} luminescence centres comes from the Eu^{2+} content in the $SrSO_4$ lattice being usually much lower than the amount of Eu added to a solution. We have suggested[I.] that europium sulphate does not precipitate well from the solution together with $SrSO_4$. Paramagnetic Eu^{2+} was observed by EPR. What concerns the luminescence studies, only Eu^{2+} luminescence band was recorded, while Eu^{3+} lines have never been seen in our samples (Fig. 5).

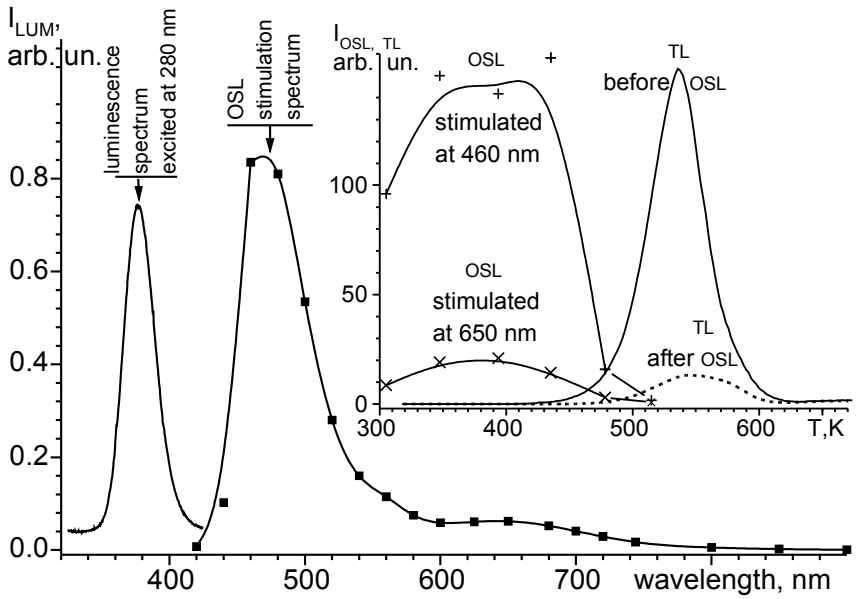

Fig. 5. Luminescence spectrum of Eu^{2+} in $SrSO_4$ measured at T = 300 K under a UV -LED excitation (280 nm). OSL stimulation spectrum is shown at the same plot, where luminescence intensity was measured using optical filters to separate the luminescence band of Eu^{2+}. The abrupt fall at UV edge of spectrum is caused by an optical filter used at the excitation side in addition to a monochromator. The insertion demonstrates the OSL efficiency versus pulse-step annealing temperature. The variations of stimulation efficiency at 460 nm (—+—) and at 650 nm (—x—) are shown separately. The TSL curves are placed here as well: before (solid line) and after (dashed line) optical stimulation with a powerful LED LXHL-LB3C (470 nm, 248 min at a distance of about 2 cm). The sample was excited with a $^{90}Sr/^{90}Y$ radiation source. The exposition dose of 1.2 Gy was given each time prior to either TSL measurement or prior to optical stimulation with the subsequent TSL measurement.

So, we decided, that the charge state of Eu entered into a $SrSO_4$ matrix should be mostly 2+. However, we are to mention here the data obtained by measuring the magnetic susceptibility χ as a function of temperature using a SQUID-magnetometer. The Curie constants were obtained by fitting the measured data with the Curie-Weiss law $\chi = \chi_0 + C(T-\theta)$. The concentrations of Eu^{2+} were calculated from Curie constants: $x = 3kMC/[S(S+1)g^2\mu_B^2N_A]$, where k is Boltzmann constant, M is molar mass of $SrSO_4$ (183.6842 g), C is Curie constant, S is a spin quantum number (7/2 for Eu^{2+}), g is g-factor Lande, μ_B is Bohr magneton, and N_A is Avogadro constant. With the introduced into solution

amount of Eu being 0.05 m%, the measured in $SrSO_4$ amount of Eu^{2+} occurred about 2.5 times lower compared to the expected one, would all the introduced Eu have precipitated as divalent europium sulphate together with $SrSO_4$. Ten times higher amount of Eu (0.5 m%) in solution increased the Eu^{2+} amount in luminophor only twice, the latter being yet 1/10 of the expected one. We decided that Eu has not precipitated efficiently together with $SrSO_4$. However, the behaviour of the χ_0 indicated another possibility. Yet remaining negative, the χ_0 constant has systematically increased with the increase of the added amount of Eu. This would be most obviously caused by the increase of the Eu^{3+} amount in the solid solution: Eu^{3+} is known as a Van-Vleck ion giving a weak temperature-independent paramagnetism. Hence, the reason why we have a very small amount of Eu^{2+} in our $SrSO_4$ would be connected with some redox reactions occurring at synthesis. The fact that Eu^{3+} is present is not so bad itself, but the optimum ratio of Eu^{2+} and Eu^{3+} is under the question. We shall yet discuss this point below.

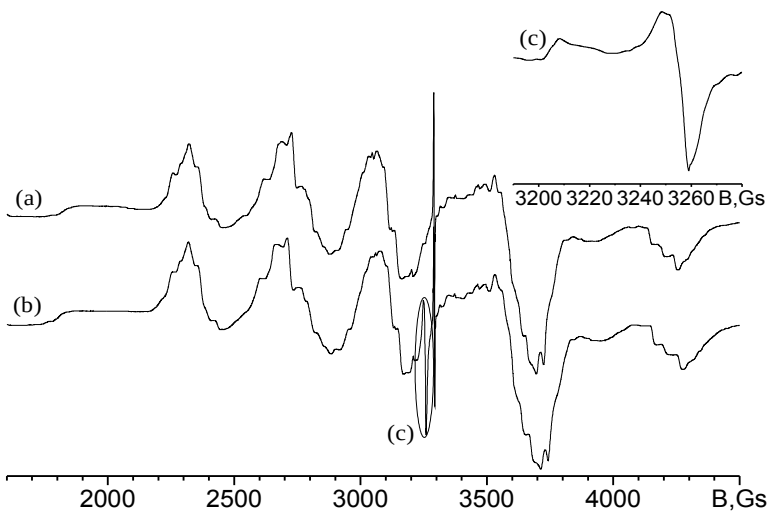

Fig. 6. EPR spectra (T = 300 K) of Eu^{2+} in $SrSO_4$: (a) – before irradiation; (b) – after X-raying (W-anode, U = 53 KV, 1 h = 60 kGy); (c) – the partially overlapping spectra of radiation-induced hole centres appeared after X-raying; the same spectral region is shown at the insertion, where the unchanged Eu^{2+} spectrum is subtracted. The hole centres are destroyed by annealing the samples at the temperature of dosimetric peaks. A sharp line at about 3300 Gs belongs to a reference signal of Cr^{3+} in MgO.

OSL stimulation spectrum consists of a strong band around 460 nm, and a lower shoulder at longer wavelengths[I.]. We could not use the time-resolved technique (OSA — optically stimulated afterglow) due to a very fast response of

the stimulated luminescence. However, the TSL peak destroying by stimulating light was relatively slow. An irradiation of the excited sample with a powerful (up to 0.5 W of light power) blue LED (470 nm) during 4 h has removed TSL peaks almost completely (Fig. 5). The TSL curve shows a pronounced structure when being partially destroyed by optical stimulation. At least, two overlapping each other peaks can be observed.

Our EPR studies revealed the number of Eu^{2+} ions being unchanged after X-irradiation with a dose of 60 000 Gy (Fig. 6). At the same time, EPR signals of radiation-induced centres were observed after irradiation[1]. The observed overlapping each other signals belong to anisotropic centres. For the dominating defect, we have determined roughly the following two principal g-tensor values, $g_1 \approx 2.031$ (with an essential positive shift), and $g_2 \approx 2.000$ (close to that for a free electron). The detailed analysis of all the observed defects requires additional studies. The signals disappear at annealing in the temperature range of basic TSL peaks, hence, they could be involved in TSL process. We suppose them to be hole centres created by radiation through ionisation of sulphate anions, some kind of $(SO_4)^-$ centres (Fig. 6(c)).

The 470-nm irradiation of the sample with already annealed basic TSL peak (but preserved very negligible TSL peaks at higher temperatures) causes the basic dosimetric peak to be restored in a very small fraction of the initial intensity. This fact can be explained by optically stimulated hole migration. Strontium sulphate is expected to have a complex structure of valence band composed of relatively narrow but partially overlapping sub-bands . This would slightly impede the optically stimulated hole transport. That is why it requires much time to clean the traps by optical stimulation. The process can be assisted by heating (see the increase stage of OSL at pulse-step annealing in Fig. 5). The fact of Eu^{2+} amount being unchanged during energy storage and release means that an electron should be captured somewhere in the vicinity of Eu^{2+} but does not cause charge transformations of the latter. A hole is delivered here either by thermally or by optically activated migration processes. Recombination causes Eu^{2+} to accept energy and produce the luminescence through its' well-known 5d — 4f radiative transition. There is some difference between optical and thermal activation of hole migration, and the details of processes should be additionally investigated. However, some ideas can be formulated on the basis of both our own data and the published by other researchers information.

The coexistence of both Eu^{2+} and Eu^{3+} ions in $SrSO_4$ favours the model of trapping centres stabilized by two opposite defects: Eu^{3+} would stabilize electron centres $(SO_4)^{3-}$, while a cation vacancy compensating Eu^{3+} charge would stabilize a hole centre $(SO_4)^-$. If the both occur not very far one from another, a quasi-intracentre recombination would be observed with the side recombinations being minimally involved into the TSL mechanism. The hole centres $(SO_4)^-$ are known to be less stable than electron centres $(SO_4)^{3-}$, hence, one would expect the recombination to occur at the electronic traps. However,

the Eu^{2+} should be present in the vicinity of Eu^{3+}, in order the recombination energy to be efficiently transferred to Eu^{2+}. Yet, some amount of either holes or electrons would be trapped rather far one from another. This causes the observed peculiarities in TSL and OSL. The balance between the amounts of Eu^{2+} and Eu^{3+} ions and their relative positions would depend on the redox reactions at the synthesis of luminophor. Regarding a cation vacancy to compensate a positive charge of two trivalent impurity ions, the optimum amount of Eu^{3+} would be either twice of the amount of the Eu^{2+} or at least the same, but not 10:1. It seems to be not very essential which trivalent ion would form an electron trap, so the necessary requirement is only that the impurity ion would not give luminescence transitions due to resonance energy transfer from recombination site. Hence, it would be possible to select a suitable redox pair for europium in order to direct the reaction to the desired scheme. Cation vacancies will be most probably involved both in the reaction and in the resulting complex centres. The additional studies are needed to find the optimum redox pairs and synthesis conditions. What concerns the optical stimulation, a thermo-optical readout should be tried in order to facilitate the transfer of holes in the stratified valence band. For the same reason, the optical stimulation with the quanta of somewhat higher energies should be tried.

CaF_2:Mn

One of the known disadvantages of CaF_2:Mn (commercially available as TLD-400) is a strong dependence of TSL curve on the concentration of Mn and low stability of the material against repeated annealing when it is re-used or re-calibrated. A low stability is caused by the precipitation of Mn from solid solution with further oxidation of Mn^{2+} to higher charge states. This occurs when Mn concentration exceeds the threshold of solid solution decomposition. However, the most suitable TSL curve with a narrow high-temperature peak is formed when concentration of Mn is very close to this threshold[47]. To avoid the undesirable effects, one needs to know the energy storage and thermoluminescence mechanisms in this material in order to design proper technology for thermoluminescent detectors.

We shall move towards understanding how it works by the thermoluminescence kinetics studies[II]. The sample with 2.36 m% of Mn has been chosen, possessing a narrow TSL peak centered at 585 K with only a small shoulder at lower temperatures. Pre-annealing at different temperatures caused TSL curve transformations: a low-temperature shoulder disappeared, and then peaks of lower intensity appeared at a higher temperature. The observed transformations required a long time, from several minutes to 3 hours. No «run-time» transformations have been observed when TSL curve was measured with a relatively low heating rate (0.325 K/s). This probably indicates that some ionic process is involved in TSL curve transformation at annealing. This could be either re-orientations or recapturing of fluorine displaced into interstitial

position at the irradiation with β-radiation source. The only known defect keeping fluorine above the room temperature in CaF_2 is a neutral F_2 molecule. It has been called as a "pair of self-trapped holes", being proved to exist in CaF_2:Sm[74]. What about electrons, they could be trapped at anion vacancies near Mn^{2+} according to a known model[42].

To study the TSL kinetics, isothermal afterglow curves were measured after the excited sample has been pre-annealed for 1 min at 520 K and then rapidly heated up to a fixed temperature[II]. The observed decay curves can be exactly approximated with two exponents at any fixed temperature (an isothermal decay at T= 559.25 K is shown in Fig. 7).

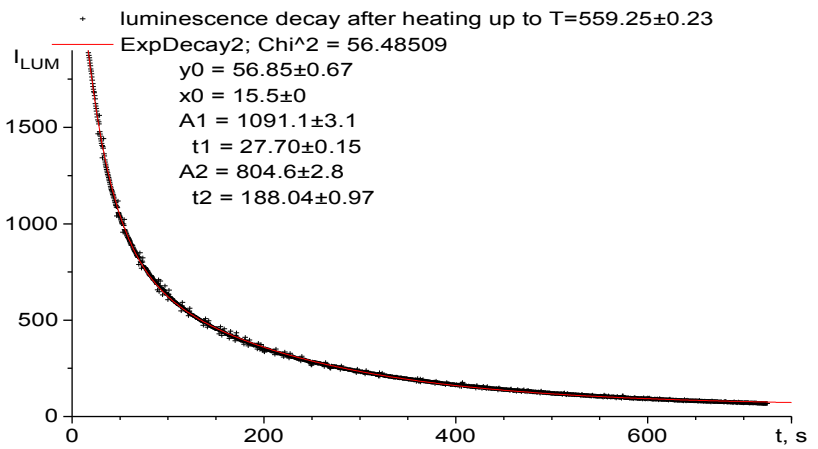

Fig. 7. Isothermal luminescence decay after fast heating the sample up to 559.25 K is approximated nicely with a sum of two exponents.

This means that recombination rate depends linearly on numbers of defects or excited states, but not on the products of these numbers. This kind of first-order kinetics indicates some kind of intra-centre energy storage and release. Also, no variations of Mn^{2+} number have been detected by EPR[47]. Hence, the transformation of TSL curve at partial annealing should be connected with re-arrangement of defects, without transfer of carriers to other recombination places. We suppose that TSL occurs at the return of fluorine to the initial place where from it has been removed by irradiation. A simple mathematical model can be suggested to describe the TSL kinetics. Let's designate by N_{ST} the number of excitations stored in a form of neutral F_2 interstitial molecules, and by N_{EX}, the number of thermally excited to dissociation F_2 molecules. We suppose also that the activation energy E of dissociation of F_2 essentially exceeds the activation energy of interstitial fluorine migration (about 0.35–0.4 eV for moving around trivalent impurities[75]). We neglect also any additional recombination barriers and re-localizations (that is true yet to some extent). So,

we have the following simplified equations considering only the probability of return of fluorine to the stored position, and the probability of recombination:

$$\frac{dN_{ST}}{dt} = -N_{ST}\cdot W_0\cdot e^{-E/kT} + N_{EX}\cdot W_C \quad (1)$$

$$\frac{dN_{EX}}{dt} = N_{ST}\cdot W_0\cdot e^{-E/kT} - N_{EX}\cdot W_C - N_{EX}\cdot W_R \quad (2)$$

where W_R and W_C are recombination and retrapping probabilities, and W_0 is a frequency factor, k is Boltzmann constant. The thermoluminescence intensity will be given by the recombination part: $I_{LUM} = -N_{EX}\cdot W_R$.

The solution of the system (1) and (2) is a sum of two exponents, $A_1\cdot e^{\lambda_1\cdot t} + A_2\cdot e^{\lambda_2\cdot t}$ The factors λ_1 and λ_2 under the exponents can be determined from the characteristic equation:

$\lambda^2 + \lambda\cdot(W_R + W_C + W_0\cdot e^{-E/kT}) + W_R\cdot W_0\cdot e^{-E/kT} = 0$ Using Viète theorem, we have: $\lambda_1 + \lambda_2 = -(W_C + W_R + W_{T0}\cdot e^{(-E/kT)})$ and $\lambda_1\cdot\lambda_2 = W_R\cdot W_{T0}\cdot e^{-E/kT}$ It is more convenient to represent the solution with a sum of two decaying exponents $A_1\cdot e^{-t/\tau_1} + A_2\cdot e^{-t/\tau_2}$ with decay times $\tau_1 = -1/\lambda_1$ and $\tau_2 = -1/\lambda_2$. The following equations for the parameters of kinetics can be derived from this solution:

$$\ln\left(\frac{1}{\tau_1}\cdot\frac{1}{\tau_2}\right) = \ln(W_R\cdot W_0) - \frac{E}{kT} \quad (3)$$

$$\frac{1}{\tau_1} + \frac{1}{\tau_2} = (W_C + W_R + W_0\cdot e^{(-E/kT)}) \quad (4)$$

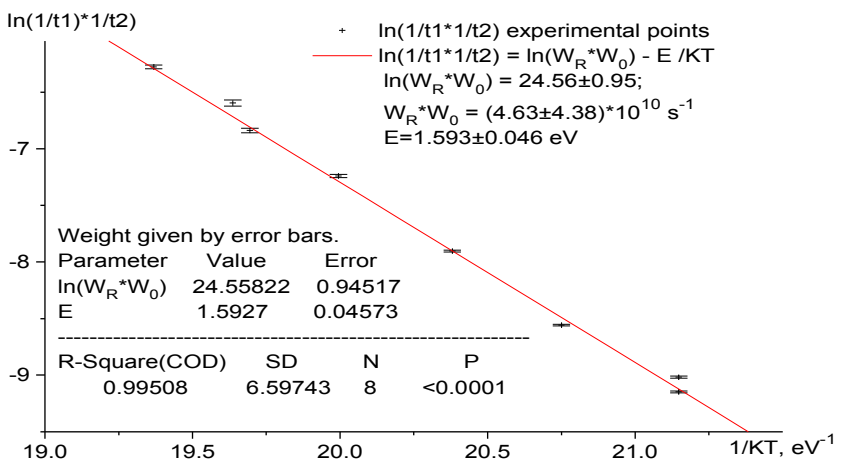

Fig. 8. Activation energy E and a product of W_0 and W_R are obtained by linear approximation of data according to the equation (3).

Activation energy E, recombination and recapture probabilities W_R and W_C, and frequency factor W_0, were determined according to (3) and (4) from the temperature dependence of the natural logarithm of the product of inverse decay time values, $1/\tau_1$ and $1/\tau_2$, and from the temperature dependence of their sum. The plots in Fig. 8 and Fig. 9 show the results in a corresponding form.

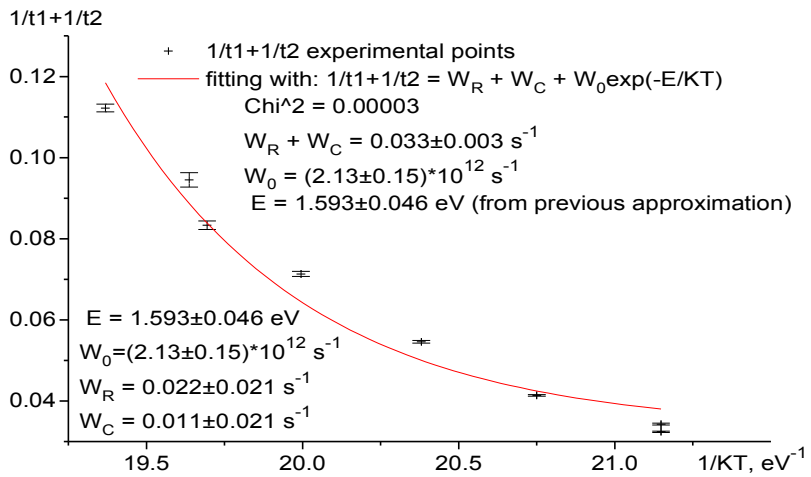

Fig. 9. Exponential approximation of the sum of inverse decay constants using both an activation energy and a product of W_0 and W_R obtained from a previous approximation.

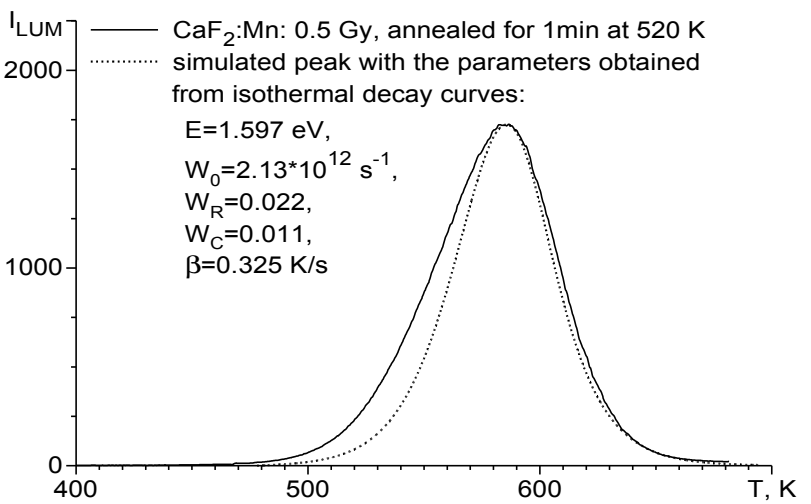

Fig. 10. Simulated and experimental TSL peaks.

Following the model, a TSL peak was digitally simulated, solving the equations with time substituted for temperature (linear heating, $T=T_0+\beta \cdot t$) by means of Runge-Kutta algorithm.

Fig. 10 shows a good correspondence of simulated peak and experimental curve, except for the low-temperature shoulder. A low-temperature shoulder could be due to the presence of molecules with a lower stability. Kinetics measurements are not severely affected by this shoulder, which is quickly annealed at a pre-annealing procedure before each measurement, and thus exerts a negligible influence on the decay curves. It is interesting that the TSL peak activation energy (1.597 eV) occurred surprisingly close to the energy of dissociation of a neutral F_2 gaseous molecule (1.606 eV[76]), and this energy exceeds all the previously known thermal decay activation energies for various intrinsic defects in CaF_2. This is an indirect evidence of the mechanism of thermoluminescence in CaF_2:Mn: such a high TSL activation energy is more characteristic for ionic processes in the radiation-damaged lattice, rather than for pure electron-hole processes. The co-incidence of thermal activation energies is not the only one. It is very interesting to know that the radiation-induced absorption band in the region of 280-300 nm[48], and also the OSL excitation spectral band in CaF_2:Mn[49], are very close to the measured absorption band of a free F_2 molecule[77]. Surely, the hypothesis of fluorine storage in the form of neutral interstitial F_2 molecules requires some additional examinations, however, it seems to be realistic.

We should note that the obtained retrapping probability value (0.011 s^{-1}) is high enough being only one-half of the recombination probability value of (0.022 s^{-1}). This means that the reverse to the dissociation of F_2 process is very strong even at high temperatures. Hence, the OSL efficiency cannot be very high at room temperature. "Warmed" OSL measurements would have better efficiency but probably it helps only partially. The best solution would be to improve the transport of released fluorine to the sites where from it has been removed at irradiation. This will require some better ordering in the impurity cluster. What does it mean?

First, one could ask about the different thermal stabilities of the F_2 molecules for different Mn concentrations: the changes in TSL curves structure have been observed together with changes of lattice constant[47]. To find an answer, we should remember a peculiar mechanism of rare-earth ions clusterization in CaF_2 lattice having been proved by a high-resolution optical spectroscopy[31,32]. The ordered structures of shifted towards interstitial positions fluorine ions and anion vacancies arise around the trivalent impurities. The matter is that we could not provide manganese entering the CaF_2 lattice in a divalent state exclusively. The amounts of Mn^{2+} and Mn^{3+} are at least comparable, as it is followed by magnetic susceptibility measurements. Hence, one could suppose the same clusterization mechanism for Mn^{3+} as it is proved to occur with trivalent rare-earth impurities. The ordered structures of different compositions

arise depending on the amount of triply charged metal in the cluster, and hence, depending on the concentration of impurity and on the synthesis conditions. In general, the tendency of impurity aggregation is very strong in CaF_2, as it has been proved by observing a non-random distribution of Mn^{2+} and Ce^{3+} impurities in CaF_2 by studying a resonance energy transfer[26–28]. The thermal stability of F_2 interstitial molecule is higher, when there is a proper space to adopt it without essential overlap of electronic clouds with the surrounding fluorine at regular sites in CaF_2 lattice. The more overlapped are electronic clouds, the less stable is chemical bond, and the lower is dissociation energy. This idea nicely accounts for the diversity of TSL peaks at lower Mn concentrations: there are different ordered structures formed, with the different size of a free space, and hence, with the different thermal stabilities of the interstitial F_2 molecules. Only when Mn concentration approaches the solid solution decomposition threshold, a highly ordered clusters with enough free space are formed to provide the highest thermal stability of F_2 and the minimal diversity of the activation energies.

We see, that redox transformation of Mn at the moment when solid solution is formed and ordered provide us with almost ideal complementary structure of traps suitable for storage of a large amount of excitation energy. The idea of redox transformations of impurity in the luminescent material at the moment of solid solution formation seems to be an essential point for designing effective storage phosphors. Moreover, this idea helps to find a solution how to avoid working near the decomposition threshold and essentially increase the life-time of CaF_2:Mn radiation detectors. The redox reactions between manganese and rare earth impurities could be the medicine solving a problem. Indeed, the transformations $Mn^{3+} \rightarrow Mn^{2+} + e^-$; $Re^{2+} + e^- \rightarrow Re^{3+}$ could be arranged in the CaF_2 lattice using the proper redox-complementary partners for Mn. Providing the closely-spaced complementary pairs for the reaction seems to be not a problem[26–28]. In this case, the structured clusters formation will be governed by the triply charged rare-earth, which makes much better results than the process with Mn having the unstable at synthesis charge state. The suggested solution will improve the properties of the CaF_2:Mn-based thermoluminescent detectors.

$Li_2B_4O_7$:Mn and $Li_2B_4O_7$:Mn,Be

Material characterization and structural features

The results of XRPD analysis are shown in Fig. 11. The finished detectors (tablets) demonstrate a very distinct pattern, corresponding to $Li_2B_4O_7$. The shapeless background of glassy phases is not seen for sintered tablets. There are no effects from either Mn or Be doping: concentration of added impurities is too low (about one impurity atom per hundred lattice units), so the XRPD pattern shows neither pronounced distortions nor separate phases. The insertion in Fig. 11 shows the improvement of $Li_2B_4O_7$ crystal lattice in tablets with sintering temperature increase. The effect is followed by the decrease of full-width-half-maximum (fwhm) parameter of the line of most separated reflex 202. The improvement is very pronounced when one compares raw material and sintered tablets. The next-level insertion (Fig. 11) shows the further improvement taking place up to melting point of $Li_2B_4O_7$.

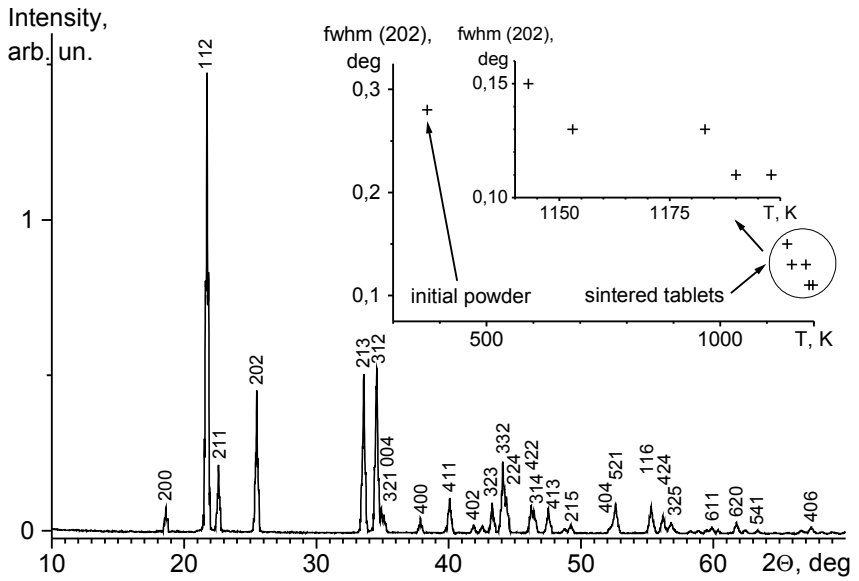

Fig. 11. XRPD pattern for a sintered tablet (1198 K) corresponds to $Li_2B_4O_7$, the characteristic reflexes of which are marked. The insertions demonstrate how the lattice structure improves with sintering temperature increase. Lattice improvement can be assessed by the decrease of the 202 reflex line-width (fwhm).

Li sites and space in helicoidal voids are regarded usually as the only possible places to be occupied by various impurities in lithium tetraborate. This comes

from the comparison of ionic radii of different impurities with the sizes of possible sites in $Li_2B_4O_7$ lattice. For example, Mn^{2+} in tetrahedral coordination (80 pm) is drastically larger than B^{3+} in tetrahedral coordination (25 pm). That is why a substitution of B^{3+} with Mn^{2+} seems to be scarcely possible. Nevertheless, we shall regard below the possibility of such substitution in order to explain some experimental data. Hence, we need some closer consideration of the question. The lengths of (B^{3+} - O^{2-}), (Mn^{2+} - O^{2-}), (Mn^{3+} - O^{2-}), (Be^{2+} - O^{2-}) bonds in some substances are compared in Table 1.

Table 1. Manganese-oxygen bond lengths in some substances

Structure and elements	Bond length, pm	Substances and references
Mn^{2+} - O^{2-} (4 closest O^{2-})	from 209.2 to 214.1	Manganese diborate MnB_4O_7[78], orthorhombic
Mn^{2+} - O^{2-} (distorted octahedral)	from 202 to 228	Jimboite $Mn_3(BO_3)_2$[79]
Mn^{2+} - O^{2-} (distorted octahedral)	from 208.6 to 224.7	Manganese(II,III) oxyborate Mn_2OBO_3[80], monoclinic
Mn^{3+} - O^{2-} (distorted octahedral)	from 188.1 to 197.7	Manganese(II,III) oxyborate Mn_2OBO_3[80], monoclinic
Be^{2+} -O^{2-} (tetrahedral)	from 168.5 to 168.6	Beryllium oxide BeO[81], wurtzite Mn^{2+} detected at Be^{2+} positions by EPR[82]
(B^{3+} + 4O) tetrahedra B2 - O1 B2 - O4 B2 - O3 B2 - O2	 145.0 145.3 150.2 150.5	Lithium tetraborate $Li_2B_4O_7$[54] (Fig. 3)
Li - O bonds Li - O1 Li - O2 Li - O3 Li - O3' Li - O4	 218.1 197.0 203.5 207.0 259.2	Lithium tetraborate $Li_2B_4O_7$[54] (Fig. 3)

(B^{3+} - O^{2-}) distances in lithium tetraborate tetrahedra vary from 145.0 to 150.5 pm. (Mn^{2+} - O^{2-}) distances usually exceed 200 pm in manganese-boron-oxides, while (Mn^{3+} - O^{2-}) distances are smaller. Hence, if manganese incorporation at tetrahedral boron sites is yet possible in lithium tetraborate, this should occur much easier for Mn^{3+} than for Mn^{2+} (there is also no need to compensate a charge). Incorporation of manganese in very tight tetrahedral environment is proved by EPR in BeO ceramics with the wurtzite crystal structure[82]. Mn^{2+} occupies Be^{2+} sites of tetrahedral symmetry in BeO despite of short rigid covalent bonds in this substance. Oxygen tetrahedra in $Li_2B_4O_7$ are less rigid compared to BeO lattice. B2 - O4 bond (Fig.3(a)) is the weakest one in

$Li_2B_4O_7$[83] and has the most pronounced variations of the length with temperature[54]. Would either Mn^{3+} or Mn^{2+} occur at the position of B2, the tetrahedron size could be increased mostly at the account of a weak bond with O4 atom. So, the incorporation of manganese into lithium tetraborate seems to be possible at Li positions without a doubt, and probably possible at B2 positions, too. We shall recall yet these ideas in the next sections.

According to the EPR spectra, there are two types of Mn^{2+} centres in $Li_2B_4O_7$:Mn (see the details below). EPR studies revealed the amount of Mn^{2+} ions to increase when sintering temperature is increased, until a complete melting occurs (Fig. 12). The studies have been performed with the samples created from the same precursor, the only difference was temperature of sintering.

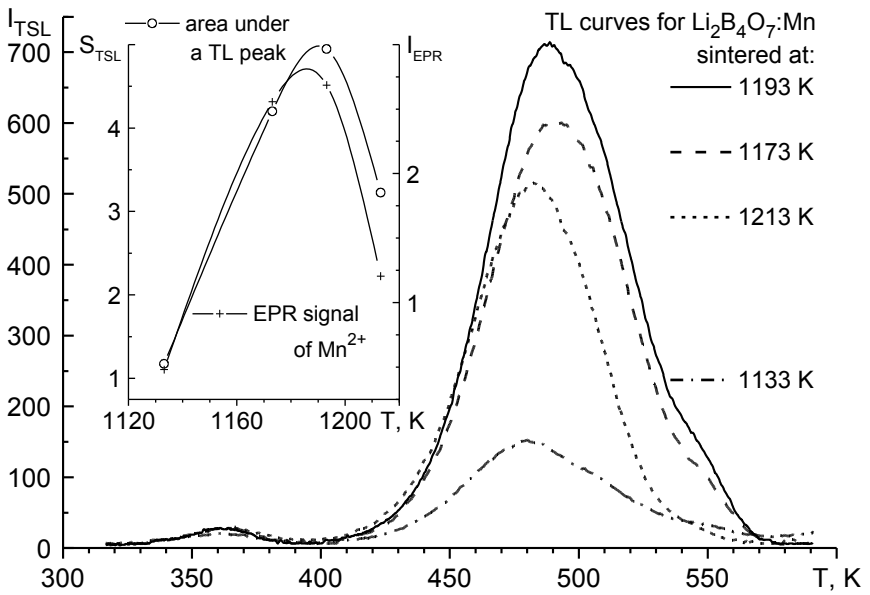

Fig. 12. The transformations of TSL curve with increasing sintering temperature of $Li_2B_4O_7$:Mn tablets. The insertion compares the area under dosimetric TSL peaks (400 K-570 K) with the intensity of EPR signal of Mn^{2+} as functions of sintering temperature of tablets. Better collection of light causes a slower decrease of TSL peak area compared to Mn^{2+} EPR signal at melting.

The EPR signal of Mn^{2+} in glass phase has a different structure and is less intensive. It cannot be observed with low manganese concentrations used in our studies. The increase of Mn^{2+} at annealing is connected with transformation of Mn^{3+} to Mn^{2+}. The reduction of manganese from 3+ to 2+ at sintering is deduced also from the magnetic susceptibility of samples. The derived from magnetic susceptibility Curie constant is only about 20% lower for the samples with 4.5

times lower Mn^{2+} content estimated by EPR. This could happen when initial Mn^{3+} is in a high-spin state, which is known for Mn^{3+} ions occupying sites with a distorted tetrahedral symmetry. Hence, the idea of Mn^{3+} substituting for B^{3+} in tetrahedral sites is quite reasonable. We shall give some more evidences for that below. When Mn^{3+} is reduced to Mn^{2+} at increased temperatures, the ratio between different Mn^{2+} centres remains constant.

The area under dosimetric peaks behaves the same way as the amount of Mn^{2+} ions does with sintering temperature increase (Fig. 12, insertion). Hence, trapping centres are likely to be somehow connected with Mn^{2+} in $Li_2B_4O_7$. Mn^{2+} does not change a charge state at energy storage and release, but the amount of stored and released energy is proportional to the Mn^{2+} concentration in detector. This fact indicates that trapping centres occur in the vicinity of Mn^{2+}, and the recombination of the charge carriers produces the excited state of Mn^{2+} through some kind of energy transfer or charge-transfer excitation.

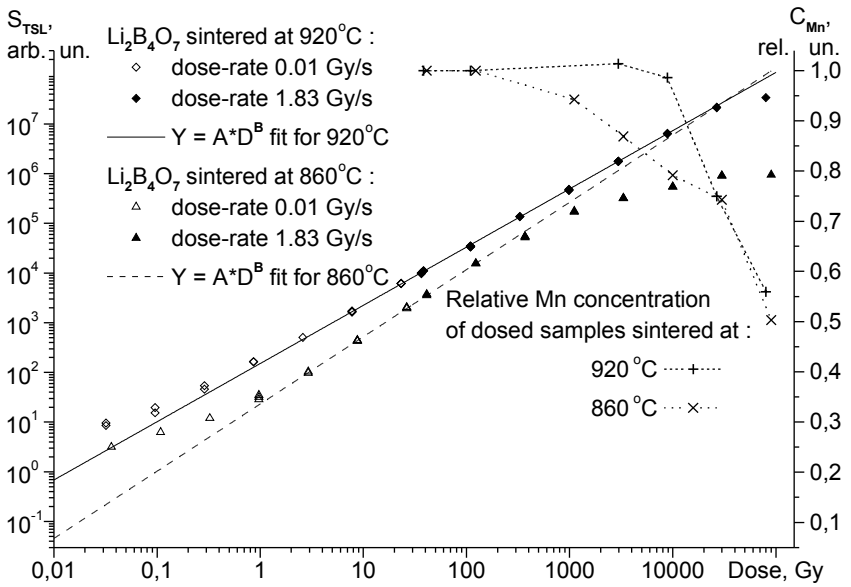

Fig. 13. The area under dosimetric peaks as a function of exposition dose is plotted for two batches of tablets with different sintering temperatures. Both show superlinearity at doses 1 Gy–500 Gy. Mn^{2+} amount decreasing by irradiations is shown at right axis. A saturation of dose dependence is well-correlated with a destruction (recharging) of Mn^{2+} by radiation. Yet Mn^{2+} amount stays unchanged at lower doses.

The dose dependences were studied in very large dose ranges, from 0.033 Gy to 60000 Gy, for two sets of samples with different Mn^{2+} concentration caused by different sintering temperatures (Fig. 13). EPR shows that Mn^{2+} amount is

affected neither by radiation energy storage nor by energy release in thermoluminescence, which behaviour being true only in the range of doses far from saturation effects. Saturation effects are accompanied with Mn^{2+} amount decrease, and occur at smaller doses for samples with a lower Mn^{2+} amount. This could be caused by electron-hole amount dynamical disbalance in a damaged by radiation lattice due to the large amount of radiation-induced electron traps. Excess of holes transferred to Mn^{2+} causes it to change the charge state. The amount of Mn^{2+} restores in several complex stages after annealing detectors up to 973 K. The restoration of Mn^{2+} amount is not connected with dosimetric TSL peaks.

A false-dose problem

The problem of the sensitivity of $Li_2B_4O_7$-based TLD to daylight was known previously[84–86], especially for $Li_2B_4O_7$:Cu. The effect of light on the dose stored in $Li_2B_4O_7$:Mn detectors was mentioned in two publications[87,88]. However, neither explanations nor models were suggested. We had encountered the day- light induced false dose in the case of only a few samples among a large set of detectors, but the situation repeated steadily from one set to another.

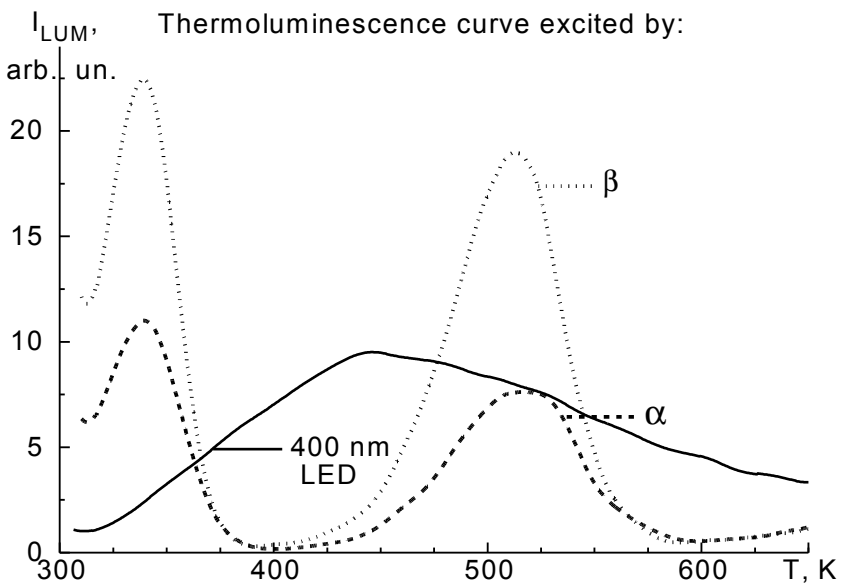

Fig. 14 Thermoluminescence curves of light-sensitive $Li_2B_4O_7$:Mn,Si detector excited by different means: α-particles (about $1.8 \cdot 10^7$ particles), β-particles (0.25 Gy), a 400 nm light-emitting diode (about $1.5 \cdot 10^{19}$ photons).

Thermoluminescence studies have demonstrated that both light-sensitive and light-insensitive samples have the same TSL curve when excited by either β- or α-particles[III]. What concerns the excitation by light, the most efficient to excite thermoluminescence has been found a 400 nm light emitting diode (LED).

However, the TSL curve excited by 400 nm is very different from that one

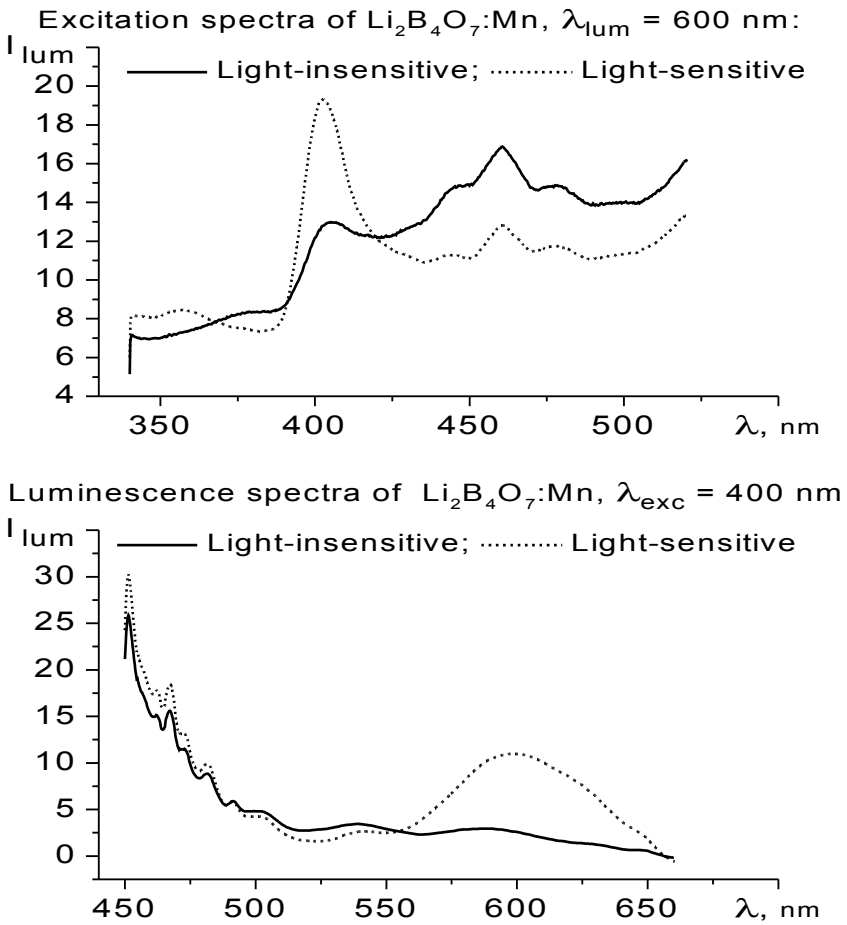

Fig. 15. Luminescence and luminescence excitation spectra of light-insensitive and light-sensitive samples of $Li_2B_4O_7$:Mn

excited by ionizing radiation (see Fig. 14). The TSL curve induced by light is very wide, it covers all the temperature range from 320 K to 650 K, having a broad maximum about 440 K. Some samples have demonstrated still broader curve, showing a strong afterglow at room temperature. The TSL curves induced either by β- or by α-particles are very similar: both have two peaks, one of them (near

510 K) being always used for dose measurements. Light is completely ineffective to excite these two TSL peaks, giving instead a broad curve. Hence, the mechanisms of energy storage should be completely different in cases when TSL is excited either by light or by ionizing radiation.

We have studied photoluminescence and photoluminescence excitation spectra of different samples of $Li_2B_4O_7$:Mn: either with pronounced sensitivity to daylight or without any daylight sensitivity[III]. The spectra are shown in Fig. 15. The luminescence of Mn^{2+} is excited in activator band similarly poorly either in light sensitive or light-insensitive samples. This is natural for the intracentre transitions of Mn^{2+} which are both spin and parity forbidden. However, light-sensitive samples show a luminescence band at 600 nm that is easily excited in the narrow peak at 400 nm. This luminescence band is similar to Mn^{2+} spectrum but is noticeably shifted towards longer wavelengths compared with Mn^{2+} in $Li_2B_4O_7$. This luminescence band could belong to either Mn^{2+} located somewhere in the other crystal field or to some impurity like a transition metal ion. When the samples are excited in the band at 400 nm, the luminescence of some oxygen complex (in the region of 460-470 nm; probably, borate clusters) is also observed in both cases, of light-insensitive and light-sensitive material. The excitation at 400 nm of a luminescence band with a maximum near 600 nm cannot occur through band-to-band transitions. It is essential to note that energy storage occurs in the light-sensitive samples just after the excitation in the narrow band at 400 nm where the luminescence of this unknown complex is excited. Hence, this is not a simple co-incidence. We can suppose that we deal with a charge-transfer excitation of some impurity, where the electron is taken from the closely coordinated anion complex. This means that the samples with light-sensitivity have such closely coordinated complex, while the light-insensitive samples have not. The structureless shape of TSL curve in case of photoexcitation is very characteristic for non-crystalline material. An increased charge-transfer excitation efficiency, a broad structureless TSL curve, a red-shifted luminescence band due to a weaker crystal field — everything indicates that the process takes place in a glass phase of thermoluminescent detector. This idea found confirmation when the false-dose creation by light disappeared completely after the sintering temperature has been increased — the crystal structure improves with the sintering temperature increase.

Thermoluminescence and its spectral composition

TSL curves of both $Li_2B_4O_7$:Mn (a) and $Li_2B_4O_7$:Mn,Be (b) are shown in Fig. 16. $Li_2B_4O_7$:Mn demonstrates two groups of TSL maxima. First one, a low-temperature (335-345 K) peak, decays very soon after excitation, so it cannot be used for dosimetry. The second group of TSL maxima (470-510 K) is used in dosimetry, it is stable for a long period of time (several months or even years). The TSL curve of $Li_2B_4O_7$:Mn demonstrates no essential differences from previously reported cases, both for TL detectors[IV] and for single crystals[68,83]. It

is essential to note that the two groups of TSL maxima have different spectral composition of luminescence. We have observed the difference by naked eye, and then tried to record the spectra.

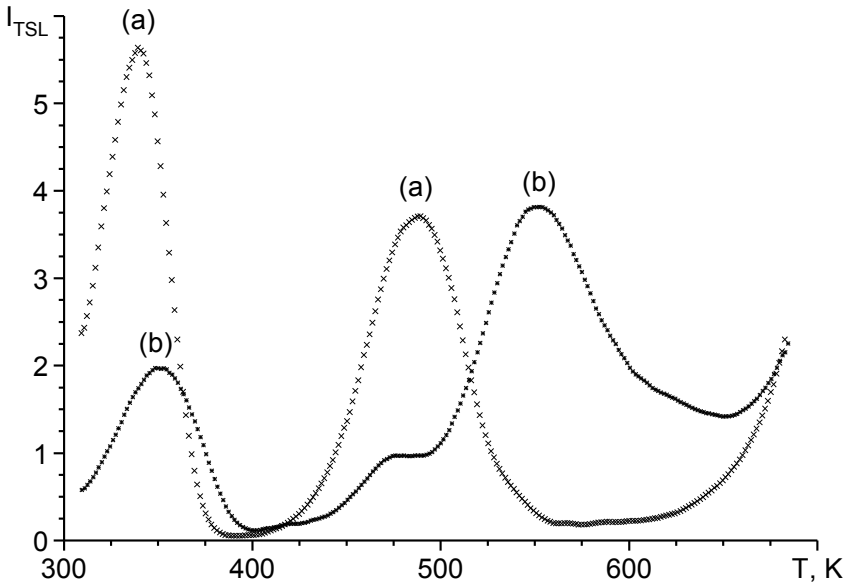

Fig. 16. TSL curves for $Li_2B_4O_7$:Mn (xxxx)(a1-a2) and $Li_2B_4O_7$:Mn,Be (****)(b1-b2). The samples were excited for 100 s with ^{239}Pu radiation source, then TSL measured after a pause of 100 s (to keep the same conditions for rapidly decaying first peak). The heating rate was 0.37 K/s. Thermal background produced by heater (above 625 K) is not subtracted. The insertion illustrates the difference in spectral composition of peaks (a1) and (a2) for $Li_2B_4O_7$:Mn.

The spectra of peaks (a1) and (a2) are shown in the insertion of Fig. 16. With the used installation being insufficiently sensitive, the recorded spectra are not enough demonstrative. So, we refer here to more accurate data of other researchers[68]. The low-temperature (335-345 K) TSL has a red luminescence band with a maximum at 608 ± 2 nm, while the high-temperature (470-510 K) TSL has an orange band with a maximum at 598 ± 2 nm[68]. Both luminescence bands can be attributed to $^4T_1$–$^6A_1$ radiative transitions of Mn^{2+} in distorted tetrahedral environments. There should be two different cases, with Mn^{2+} occupying different sites in the lattice of $Li_2B_4O_7$. The possibility for Mn^{2+} to occupy B^{3+} tetrahedral position (B2) was discussed in previous section, and some additional evidences will be given later. Let us consider now the Li^+ environment. Li atoms are surrounded by O1, O2, O3, O3 (the first coordination sphere). The distances to these four oxygen atoms are not equal and vary from

197.0 pm to 218.1 pm. Hence, the closest coordination of Li is a distorted tetrahedron, where Li is displaced from the centre in the direction of O4 atom (Li - O4 distance is 259.2 pm). The latter can be considered as the fifth top of Li - O polyhedron[54]. Hence, would Mn^{2+} occupy any of two positions, either of Li or of B2, in both cases it occurs in a distorted tetrahedral field of oxygen ligands. The tetrahedron of B + 4O is smaller than the tetrahedron of Li + 4O (Table 1). This implies the stronger field of oxygen ligands when Mn^{2+} occupies the tetrahedral position of B^{3+}. The electronic clouds of the d-electrons of Mn^{2+} overlap with clouds of the valence electrons of oxygen ligands. The larger overlap produces stronger screening between the d electrons and hence a larger reduction of the Racah parameters, resulting in a decrease in luminescence energy[89]. Hence, the Mn^{2+} at B^{3+} tetrahedral position could have the luminescence band at lower energy than that of Mn^{2+} at Li^{+} site. The luminescence bands of both types of Mn^{2+} are observed in the orange-red region. A tetrahedral Mn^{2+} is usually regarded to have mostly green-yellow luminescence contrary to Mn^{2+} in octahedral symmetry where a stronger field causes orange-red luminescence band. However, this idea should not be taken as a "universal approach", especially for distorted tetrahedral sites. Two excited levels *E* and *T* are valid yet for pure tetrahedral symmetry. Strong low-symmetry field of ligands (arranged as a distorted and very tight tetrahedral environment) causes the additional splitting of these levels. This results in the additional shifting of first excited state to lower energy thus decreasing the energy of radiative transition[90]. Hence, the red luminescence band (608 ± 2 nm[68]) should be attributed to Mn^{2+} in the tighter oxygen environment (probably, at B^{3+} tetrahedral site), while the orange band (598 ± 2 nm[68]) should belong to Mn^{2+} with a looser oxygen environment (most probably, at Li^{+} site).

If the idea of Mn^{2+} substitution for B^{3+} in B +4O tetrahedra is true, this should cause a weak bond of O4 atom with two tetrahedra to become yet weaker, and O4 will become a hole trap. Recombination at this trap should give red luminescence, while orange luminescence band at higher temperatures should be caused by recombination of released holes at some electron trap near Mn^{2+} at Li^{+} site (where oxygen environment is not so tight). We shall return to the discussion of TSL mechanisms later, after disclosing some evidences of two different Mn^{2+} centres obtained by EPR.

In case of $Li_2B_4O_7$:Mn,Be (see Fig. 16, curve (b1-b2)), the TSL peak at 470-510 K is essentially suppressed in favour of new intensive group of maxima created in the range of 525-625 K (b2). Smaller Be^{2+} would occupy the positions of tetrahedral B^{3+} much more efficiently than Mn^{2+}. This would cause the amount of Mn^{2+} at the position of B^{3+} to decrease, and the amount of Mn^{2+} at the position of Li^{+} to increase, respectively. We shall see below the correspondence of this supposition with our EPR data. Small Be^{2+} at B^{3+}

position would distort oxygen tetrahedron much less than Mn^{2+}, with O4 being displaced towards positive Li^{+} to a much lesser extent. Hence, the hole trap at O4 near Be^{2+} substituting for B^{3+} would be deeper than in case of Mn^{2+}. Indeed, the observed for $Li_2B_4O_7$:Mn,Be high-temperature TSL peak (525-625 K, see Fig. 16, (b2)) occurs at higher temperature than for $Li_2B_4O_7$:Mn, while the peak at 470-510 K (a2) is essentially suppressed.

EPR of Mn^{2+} in $Li_2B_4O_7$:Mn and $Li_2B_4O_7$:Mn,Be

The studies of EPR spectra of Mn^{2+} ions in lithium borate glasses and compounds have a long history. Many authors who have used the X-band EPR techniques mention in their works the EPR lines at low magnetic fields, formally corresponding to g≈4.3 and g≈3.3. These lines in the low-field region of spectra have been explained reasonably when using a 35 GHz spectrometer instead of a 9.4 GHz one[91]. The centre of the Mn^{2+} principal hyperfine sextet have been observed in that case only at the position of g≈2.0. The result was interpreted by assuming a spin-Hamiltonian containing crystal field terms comparable to the Zeeman energy at X-band[91]. A strong crystal field in lithium borate systems (including glasses) is expected at the distorted tetrahedral sites, both at Li^{+} and B^{3+} positions, either in crystal lattice or in glass network. The strong crystal field in the local surrounding of Mn^{2+} causes the EPR lines to be distributed in very wide range of magnetic fields in the X-band EPR spectra. This is true for various complex oxide systems and glasses. We refer here the EPR study of Mn^{2+} in $70TeO_2 \cdot 25B_2O_3 \cdot 5MO$ (MO is either SrO or SrF_2)[92], where boron-oxide structure is not a glass-former. The authors use the Mn^{2+} HFS splitting value to estimate the extent to which the bonds between Mn^{2+} and surrounding atoms are covalent[92]. Another interesting result of this study[92] concerns the clusterization of Mn^{2+} and formation of a strong broad line in the region of g ≈ 2.0.

Our EPR spectra of $Li_2B_4O_7$:Mn (a) and $Li_2B_4O_7$:Mn,Be (b) are shown in Fig. 17. A very intensive narrow line near 0.325 T is connected with the large radiation dose. A line has disappeared after annealing the sample at 700 K for 90 min, and it has not appeared again after X-irradiation with a dose of ≈ 1000 Gy. We shall not discuss in this paper the nature of this radiation-induced EPR defect.

Two different Mn^{2+} centres have been mentioned in our paper[IV]. An additional information is analysed in paper[V]. First, there are substantial differences in spectra recorded at room temperature (RT) and at liquid nitrogen temperature (LNT) (see Fig. 17). The LNT spectrum of $Li_2B_4O_7$:Mn (a, LNT) contains several groups of lines. The sextets near 0.25 T and also mutually overlapped sextets near 0.35 T are hyperfine structures (HFS) of Mn^{2+}. The spectrum in the region of 0.15 T contains several superimposed Mn^{2+} HFS lines belonging to different centres. At room temperature, the spectrum of the other type of Mn^{2+} centres is dominating, with the different fine structure and larger HFS splitting.

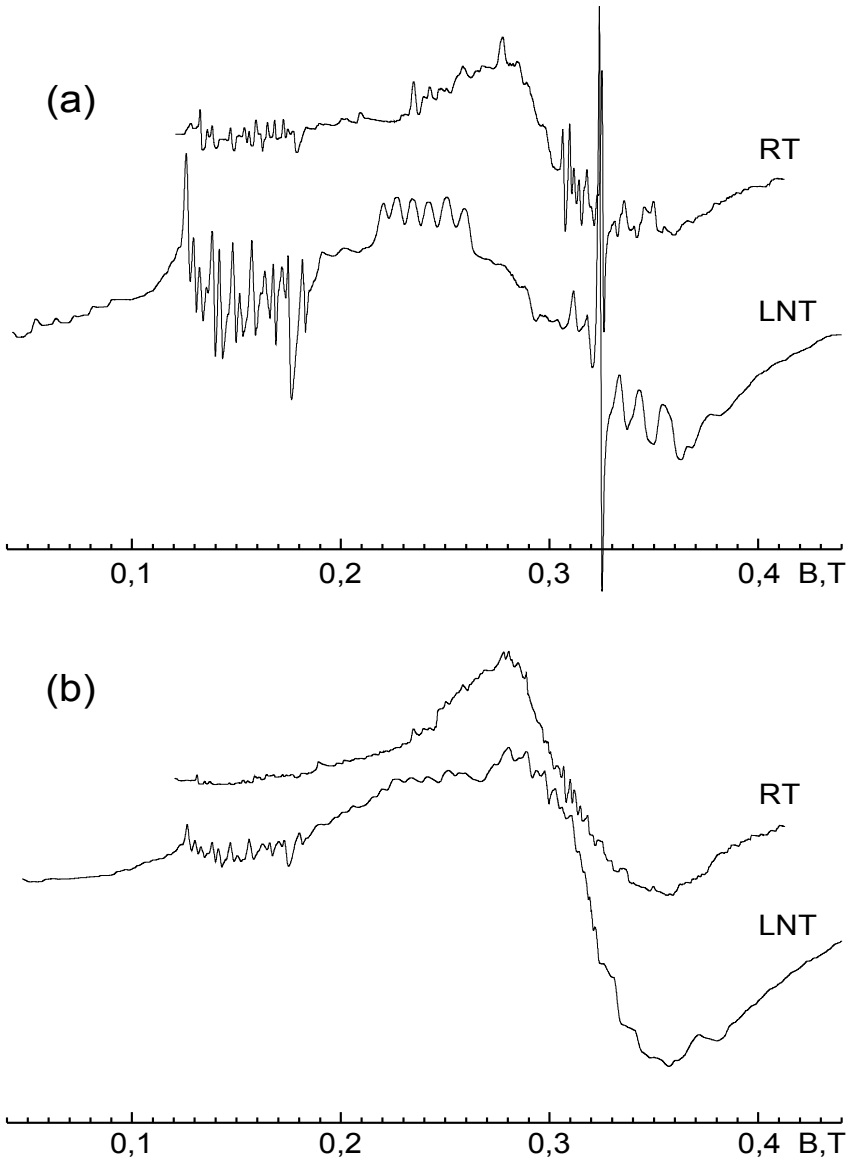

Fig. 17. EPR spectra of $Li_2B_4O_7$:Mn (a) and $Li_2B_4O_7$:Mn,Be (b) measured both at room temperature (RT, upper spectra) and at 77 K (LNT, lower spectra). Background signals of empty quartz Dewar flask and empty sample holder have been subtracted. The spectra are recorded at the same conditions (field modulation amplitude, microwave power) and are shown within the same scale.

These obvious differences in spectra of Mn^{2+} centres should be interpreted in terms of different interaction of Mn^{2+} with ligands. The stronger interaction of d-electrons of Mn^{2+} with p-electrons of oxygen ligands causes the stronger polarization effects in inner s-orbitals, and hence, a lower splitting in HFS[92]. Mn^{2+} centres possessing stronger (more covalent) bonds with surrounding oxygen atoms give dominating spectra at LNT. The average distance between HFS lines in the region of 0.22-0.26 T is ≈ 8.4 mT. It is interesting to note that the HFS of these centres is close to one observed for Mn^{2+} in BeO (about 8.2 mT[82]). Mn^{2+} at B^{3+} position in $Li_2B_4O_7$:Mn would be surrounded with tetrahedrally coordinated oxygen atoms but with a lower symmetry than it is in BeO. However, the HFS splitting is similar due to similarity of Mn – O distances in these two cases. The larger HFS splitting (about 9-9.5 mT) corresponds to Mn^{2+} at Li^+ position. There are larger Mn – O distances and less covalent bonds in this case, and also, the temperature dependence of EPR signal is less pronounced.

The two different luminescence bands observed in $Li_2B_4O_7$:Mn[68] are also connected with different interaction of Mn^{2+} with ligands in different surroundings (see text above). Here we have a good correlation of EPR and luminescence data. However, the detailed analysis of spectrum in the region of 0.30–0.38 T would be a complex task due to superimposed hyperfine structures from different centres. One encounters the same difficulties in the region of 0.12–0.19 T, where several different HFS structures overlap each other.

We have measured also the EPR spectra of samples containing the fourfold higher Mn amount. The amount of Mn^{2+} with lower HFS splitting (at B^{3+} position) increased only 1.5–2 times. The same was true for main TSL peak intensity. Here we have once again a good correlation of EPR and TSL data. The increase of Mn amount caused mostly a wide line to increase in the region of 0.28–0.37 T. This behaviour of Mn^{2+} is analogous to that one observed due to clusterization effects[92].

The HFS lines of Mn^{2+} are essentially suppressed in $Li_2B_4O_7$:Mn,Be (Fig. 17(b)). Figure shows the case when equal amounts of Be and Mn were added, while this tendency grows with the amount of Be being twice of the amount of Mn. While the HFS of Mn^{2+} almost disappeared, the wide line in the region of 0.28–0.37 T was the only increased one. The results can be explained by the suppression of incorporation of Mn^{2+} into B^{3+} positions (Be^{2+} takes these positions much easier), with the simultaneous increase of Mn clusterization effects in the voids of $Li_2B_4O_7$ lattice structure. These results are in good correlation with TSL data: a TSL peak connected with Mn is suppressed by Be, and a new TSL peak appears instead at higher temperatures.

Let us remember the correlation of TSL intensity and the amount of Mn^{2+} detected by EPR[IV.] (see Fig. 12) The amount of each of two type Mn^{2+} centres correlates with the dosimetric TSL peak intensity. We suggest the following explanation of the obtained result. At low temperature stages of synthesis

(during reaction in water and pre-heating at 823 K), Mn could substitute for B^{3+} as Mn^{3+} without any charge compensation required. This would cause yet smaller distortions of oxygen tetrahedron. When tablets are sintered at elevated temperatures, Mn^{3+} is reduced to Mn^{2+}, and then the tetrahedra containing Mn^{2+} are partially destroyed, exactly that part of them which is required for charge compensation: released Mn^{2+} occupies Li^{+} position somewhere in vicinity of Mn^{2+} that remains at B^{3+} position. This explains a simultaneous increase of amounts of both Mn^{2+} types with sintering temperature increase (as it has been observed by $EPR^{IV.}$). The idea of Mn_B - Mn_{Li} charge-compensating pairs is indirectly supported by strong exchange interactions observed with SQUID-magnetometer for X-ray excited samples (this material will be published separately). This kind of charge-compensation mechanism does not require Li vacancies to compensate Mn^{2+} at Li^{+} position. The idea of initial incorporation of manganese in form of Mn^{3+} is indirectly supported also by some chemical experiments. For example, $Li_2B_4O_7$:Mn with the same TSL properties was successfully obtained using $KMnO_4$ instead of $MnCO_3$. This fact demonstrates that the oxidation state of manganese is governed by the technological process itself and not by starting materials. After all, the idea of Mn^{3+} incorporation at position of B^{3+} with further transformation into Mn^{2+} during sintering process appears to be quite reasonable.

Thermoluminescence mechanisms and traps

Before we begin, let us exclude the possibility of Mn^{3+}-Mn^{2+} transformations and the resulting luminescence of Mn^{2+}. We speak here about relatively moderate doses (not exceeding 2000-3000 Gy) at which no Mn transformations were detected by $EPR^{IV.}$. EPR data and spectral composition of TSL peaks give an initial guess for the nature of TSL peaks.

The low-temperature (335-345 K) peak yields a red luminescence band centred at 608 ± 2 nm. This luminescence band should come from Mn^{2+} at the position of tetrahedral B^{3+}. We suppose a hole to be trapped at O4 near this Mn^{2+}. A hole trapped at O4 was studied by EPR and ENDOR[61], but in studied case it was stabilized by Li vacancy and had a low thermal stability (only up to 90 K). When Mn^{2+} substitutes for B^{3+}, the lack of positive charge at B^{3+} position produces much deeper hole trap at O4 oxygen. The hole trapped here causes a bond between two tetrahedra to get practically broken. Thermal stabilities of hole centres at broken oxygen bonds were shown to be very high in borate glasses[93]. Red luminescence band of Mn^{2+} at the position of tetrahedral B^{3+} is excited when captured at O4 hole undergoes recombination with some electron. So, the low-temperature TSL peak is caused by the recombination directly at the site where a hole is trapped. Oxygen O4 should efficiently transfer recombination energy to the Mn^{2+} at the position of tetrahedral B^{3+}. We shall discuss the nature and mechanism of these processes later.

Let us turn now to the next TSL peak (470-510 K). It shows orange

luminescence band (centred at 598 ± 2 nm) and would be connected with Mn^{2+} at Li^{+} position. This peak is used in dosimetry, the intensity of this TSL peak correlates with the amount of Mn^{2+} observed by EPR[IV]. It would be caused by recombination of released holes with captured near Mn^{2+} at Li^{+} position electrons. We suppose that the holes are released from O4 near Mn^{2+} substituting for B^{3+}. The traps responsible for this peak were destroyed after annealing sample in vacuum[83] due to the loss of O4, as the authors of paper[83] have concluded. We agree with this idea, and say more in favour of it: O4 has still weaker bonding when one of two tetrahedral B^{3+} is substituted with Mn^{2+}. Once O4 is removed, corresponding Mn^{2+} can be also released from the position of B^{3+}, making the destruction of some part of hole traps irreversible. Exactly that effect has been observed in the experiments[83]. Moreover, the amount of Mn^{2+} at position of Li^{+} has been increased after all annealing steps, thus giving a dominating orange band in radioluminescence[83].

Let us turn back to the TSL peak at 470-510 K in $Li_2B_4O_7$:Mn with no Be added. A hole released from O4 near Mn^{2+} at B^{3+} position would cause the luminescence of Mn^{2+} substituting for Li^{+} only if there is some electron trapped near the latter Mn^{2+}. Otherwise, neither a hole would be delivered against a repelling Coulomb force, nor recombination would occur. The orange luminescence band (centred at 598 ± 2 nm) of Mn^{2+} can be observed if recombination energy is efficiently transformed into the excited state of Mn^{2+} at Li^{+} position. Let us see how these two "ifs" could be realised. The first "if": what kind of an electron trap can exist in the vicinity of Mn^{2+} at Li^{+} position?

Li^{+} ions in $Li_2B_4O_7$ lattice are placed as spaced pairs in helicoidal voids of boron-oxide frame (see Fig. 3(b)). Hence, when Mn^{2+} substitutes for Li^{+}, the repelling Coulomb force is expected to shift the other closest Li^{+} out from its' regular position. Li would be probably moved to the closest interstitial position described in connection with mechanisms of ionic conductivity in $Li_2B_4O_7$[94]. The closest interstitial position for Li is situated at about 61 pm over the face of oxygen polyhedron surrounding regular Li site[94]. The extra positive charges of both Mn^{2+} and displaced Li^{+} would split off the trapping level from the bottom of conduction band. The states at the conduction band minimum are built of the antibonding BO_3-orbitals[59]. In our case, a BO_3 group would be close to both Mn^{2+} and displaced Li^{+}. We cannot speculate about the detailed structure of the electron trap, but some overlap of Mn^{2+} excited state with the wave function of a trapped electron seems to be very probable. This facilitates the transfer of recombination energy to Mn^{2+} and removes the second "if" in our model. The details of the structure of this electron trap could be studied by EPR, and this work is yet to be done.

However, we refer here to some electron traps observed by EPR in neutron-irradiated $Li_2B_4O_7$ with different isotope compositions[95]. The authors called these paramagnetic centres "Li^0 centres". The hyperfine structure in the EPR spectra of paramagnetic defects was surely caused either by ^6Li or ^7Li nuclei.

However, the reported splitting constant *A* value (about 1 mT) is too small compared with the cases when the wave function of electron is localised mostly on Li. For example, EPR of Li^0 deposited at the surface of MgO gives a value of 7.4 mT for hyperfine splitting of g-tensor[96]. Hence, the observed in $Li_2B_4O_7$ EPR signals[95] associated with Li^0 should be related rather to an electron located somewhere in the vicinity of Li, with the wave function of the electron overlapping the Li nucleus only partially. This case would be realised if the electron belonged mostly to some ligands in the vicinity of Li – probably, when Li is displaced to an interstitial position due to neutron irradiation. This seems to be very similar to our idea of electron trap in $Li_2B_4O_7$:Mn. So, we have probably a good initial guess for the future EPR studies.

The electron trap at BO_3 near positively charged Mn^{2+} at Li^+ site can be situated at several different distances from the hole trapped at bridging oxygen O4. A hole should be transferred from O4 to BO_3 ligand where an electron is trapped. Trapped electron screens a hole from extra positive charge (Mn^{2+} and Li^+) only partially. Hence, one could expect the Coulomb force to impede hole hopping to the recombination centre. Our kinetic studies have revealed the presence of an increased recombination barrier. However, we cannot also forget that a hole cannot be easily mobilized in $Li_2B_4O_7$ due to stratified structure of a valence band[59]. The valence band has a narrow sub-band at the top, composed mostly of the orbitals of BO_4 clusters (so, mostly of oxygen 2p states). A hole in the fairly narrow upper sub-band can turn into a small-radius polaron state[97]. This means that hole hopping itself requires a certain amount of activation energy. A similar case was described by Marcus/Emin/Holstein/Austin/Mott theory in various TiO_2 minerals, where hole also behaves as a small polaron[98]. In our case, there are non-equivalent states at different hole positions (non-adiabatic case), and also, we expect that Coulomb potential additionally impedes hole hopping. It is difficult to make exact calculations and to take into account all the factors, like deformation of valence band by a low-symmetry Coulomb force and so on. So we try a simplified model using a single Boltzmann exponent with some "effective" activation energy to describe hole hopping (the recombination rate contains Boltzmann factor, see below). What concerns a reciprocal square-root temperature-dependence $T^{-1/2}$ which is present in Marcus formula, it can be neglected as a “slow” function of temperature within a limited temperature range of each particular TSL peak. Let us take a look at the activation energy values for hole hopping either in $Li_2B_4O_7$ or in similar materials. The values found for TiO_2 vary from 0.17-0.25 eV for adiabatic polaron transfer to 0.55-0.62 eV for non-adiabatic cases[98]. Ionic-to-electronic conductivity transition was studied in gold-doped lithium borate glass ($20Li_2O{\cdot}80B_2O_3$)[99]. Two activation energies were observed, 1.05 and 0.34 eV. The lower of two values is related to hopping of small polarons[99]. The mixed polaronic-ionic conductivity was investigated for $Li_2B_8O_{13}$ glasses doped with different amounts of CuO[100]. The temperature of transition from polaronic to

ionic conductivity varied from 420 K to approximately 450 K depending on CuO concentrations, and activation energy of ionic conductivity varied from 0.8 to 1.22 eV[100]. The investigations of charge transport in undoped $Li_2B_4O_7$ single crystals and glasses[94] demonstrated high activation energy of conductivity through Li^+ ion hopping (1.22 eV). The lower value (0.71 eV) was found for $Li_2B_4O_7$ glass[94]. We can distinguish now between Li^+ ion hopping and polaron hopping activation energies when considering the published results of study[101] from our "partial" point of view. Short-living radiation-induced transient optical absorption bands were observed in LiB_3O_5, $Li_2B_4O_7$, and $Li_6Gd(BO_3)_3$ single crystals and connected with polarons[101]. Temperature dependence of the absorption decay kinetics was explained in the frame of diffusion model as a result of Li hopping activation. However, the authors consider, that the induced absorption can decrease not only through the ionic process of diffusion-limited annihilation of lithium vacancies with Li^0 interstitial atoms. The tunnel processes and polaron hopping are not excluded, too. The temperature dependences of kinetic parameters of the absorption decay are used to estimate respective activation energies. The results are: 0.54 eV for LiB_3O_5, 0.42 eV for $Li_2B_4O_7$, and 0.32 eV for $Li_6Gd(BO_3)_3$ single crystals[101]. We see, that the activation energies are lower than one expects for ionic hopping in these materials, but they suit well for polaron hopping. Probably, the induced transient absorption decay should be connected also with polarons hopping to some recombination centres? As for $Li_2B_4O_7$, one finds two different activation energies at the plot (Fig.3 b in paper[101]). The larger of two values would be relevant to ionic process, while the smaller one – to polaron hopping. Here we have a good estimation for polaron hopping activation energy in $Li_2B_4O_7$ with the value of 0.42 eV. As we shall see below, essentially larger values for recombination activation energies are obtained in our kinetic studies for dosimetric TSL peak (470-510 K) in $Li_2B_4O_7$:Mn and for the TSL peak at 525-625 K in case of $Li_2B_4O_7$:Mn,Be (Fig. 16). This is what we have expected from the suggested model of electron traps.

However, one should take into account several possible positions of a trapped electron relative to a trapped at O4 hole. The closest Li^+ site near Mn^{2+} at B^{3+} tetrahedral position (just behind O1 – O3 – O4 oxygen plane of the same tetrahedron, see Fig. 3(a)) could be too tight for Mn^{2+} due to deformation of the oxygen tetrahedron containing another Mn^{2+}. Would Mn^{2+} ever occur here at Li^+ position, neither a hole nor an electron would be trapped at room temperature due to very close charge compensation. When Mn^{2+} occurs at Li^+ position behind O1 – O3 – O4 oxygen plane of the B – 4O tetrahedron adjacent to that containing Mn^{2+} instead of B^{3+}, both a hole trapping at O4 and an electron trapping at an antibonding BO_3 orbital split off from the bottom of the conduction band would be possible in this complex. Due to the close positions of traps, the recombination would not require hole hopping, and also, a decreased activation energy for recombination is expected. The occupied with a

trapped electron antibonding BO_3 orbital is oriented mostly perpendicularly to a BO_3 plain. Thermal activation of the hole to an excited state causes the wave-functions of the trapped at O4 hole and the electron to overlap at temperature increase. As a result, the recombination would occur at oxygen O4, with the energy being transferred to Mn^{2+} at B^{3+} position instead of Mn^{2+} at Li^+ site. We shall see below, that the low-temperature peak (335-345 K) obeys a pure first-order kinetics, so it can be accounted for by the suggested model.

A high-temperature TSL peak (470-510 K) occurs when Mn^{2+} is situated at more distant Li^+ site after O2 (near a BO_3 plane, see Fig.3(a)). There are two such positions, and they are non-equivalent relative to O4 when Mn^{2+} is present instead of B^{3+} in one of two adjacent tetrahedra. Hence, slightly different hole hopping activation energies will be expected for hole transfer to these two non-equivalent positions. As we shall see below, a dosimetric TSL peak (470-510 K) is composed of two very close maxima, so the model accounts for the experimental data. The same is true for the TSL peak at 525-625 K in case of $Li_2B_4O_7$:Mn,Be.

Thermoluminescence kinetics

Let us turn to the kinetics data for high-temperature TSL peaks (470-510 K for $Li_2B_4O_7$:Mn and 525-625 K for $Li_2B_4O_7$:Mn,Be). Decay kinetics measured at each temperature point consist of two exponents, the faster one and the slower one. The time-constant of each exponent decreases with temperature increase. We have already encountered this behaviour in CaF_2:Mn^{II}. There should be some closed system of a hole and an electron, with a probability of side recombinations being negligibly low. Such closed system with bi-exponential decay can be described with two combined linear homogeneous differential equations. Let us designate by N_{ST} the amount of stored at O4 holes, by N_{EX} – the amount of holes thermally released from traps. W_T is the probability of trapped holes to be thermally released, $W_T = W_{T0} \cdot e^{(-E_T/kT)}$, where W_{TO} is usually called a frequency factor, E_T is thermal release activation energy, k is Boltzmann constant. W_C is retrapping probability (we do not exclude recapturing to the same trap from where a hole has been released). W_R is the recombination probability, and we should take into consideration here the temperature-dependent hole hopping probability to the recombination centre: $W_R = W_{R0} \cdot e^{(-E_R/kT)}$, where W_{R0} is not only a frequency factor but includes also all luminescence probability factors, and E_R is recombination activation energy. Actually, it is hole hopping activation energy. As we shall see from the results, E_R is larger than activation energy of polaron hopping (0.42 eV, Fig.3 b in paper[101]). We suppose it to be increased due to incompletely screened positive charges of Mn^{2+} and Li^+. The amount of stored holes decreases on the account of thermally released holes and increases due to recapturing released holes:

$$\frac{dN_{ST}}{dt} = -W_T \cdot N_{ST} + W_C \cdot N_{EX} \quad (1)$$

The amount of released from traps holes increases on the account of some more thermally released holes and decreases both due to recapturing and due to recombination:

$$\frac{dN_{EX}}{dt} = W_T \cdot N_{ST} - W_C \cdot N_{EX} - W_R \cdot N_{EX} \quad (2)$$

Luminescence intensity will be a product of recombination probability and the amount of released holes: $I_{LUM} = W_R \cdot N_{EX}$. The solution of combined equations (1) and (2) is a sum of two exponents: $A_1 \cdot e^{\lambda_1 \cdot t} + A_2 \cdot e^{\lambda_2 \cdot t}$. The factors λ_1 and λ_2 under the exponents can be determined from the characteristic equation:

$$\lambda^2 + \lambda \cdot (W_C + W_R + W_T) + W_R \cdot W_T = 0$$

Using Viète theorem, we have:

$$\lambda_1 + \lambda_2 = -(W_C + W_R + W_T) = -(W_C + W_{R0} \cdot e^{(-E_R/kT)} + W_{T0} \cdot e^{(-E_T/kT)})$$

and $\lambda_1 \cdot \lambda_2 = W_R \cdot W_T = W_{R0} \cdot W_{T0} \cdot e^{-(E_R+E_T)/kT}$

It is more convenient to represent the solution with a sum of two decaying exponents:

$A_1 \cdot e^{-t/\tau_1} + A_2 \cdot e^{-t/\tau_2}$, with the decay times $\tau_1 = -1/\lambda_1$ and $\tau_2 = -1/\lambda_2$. The following equations for the parameters of kinetics can be derived from this solution:

$$\ln\left(\frac{1}{\tau_1} \cdot \frac{1}{\tau_2}\right) = \ln(W_{R0} \cdot W_{T0}) - \frac{(E_R + E_T)}{kT} \quad (3)$$

$$\frac{1}{\tau_1} + \frac{1}{\tau_2} = (W_C + W_{R0} \cdot e^{(-E_R/kT)} + W_{T0} \cdot e^{(-E_T/kT)}) \quad (4)$$

The afterglow kinetics curves were approximated by two exponents at each temperature point. Then the logarithms of products of reciprocal time-constants and the sum of reciprocal time-constants were plotted against *1/kT* to obtain kinetics parameters. The results are shown in Fig. 18, (a) for $Li_2B_4O_7$:Mn, and (b) for $Li_2B_4O_7$:Mn,Be. The parameters obtained by approximations with functions according to equations (3) and (4) are given in Table 2.

Table 2. Kinetics parameters from decay curves and from TSL peak simulation.

	$Li_2B_4O_7$:Mn		$Li_2B_4O_7$:Mn,Be	
	from kinetics	from TSL simulation	from kinetics	from TSL simulation
E_T	0.78±0.08 eV	0.7577±0.0006 eV	0.921±0.017 eV	0.9174±0.0022 eV
W_{T0}	$(0.74\pm1.41)\cdot10^6$ s^{-1}	$(1.058\pm0.015)\cdot10^6$ s^{-1}	$(3.22\pm1.14)\cdot10^6$ s^{-1}	$(4.89\pm0.23)\cdot10^6$ s^{-1}
E_R	0.63±0.08 eV	0.6316±0.0008 eV	0.876±0.017 eV	0.8598±0.0021 eV
W_{R0}	$(0.31\pm0.57)\cdot10^6$ s^{-1}	$(0.391\pm0.007)\cdot10^6$ s^{-1}	$(8.27\pm2.72)\cdot10^6$ s^{-1}	$(15.6\pm0.6)\cdot10^6$ s^{-1}
W_C	$(0.72\pm3.51)\cdot10^{-3}$ s^{-1}	$(0.466\pm0.015)\cdot10^{-3}$ s^{-1}	$(0.08\pm0.72)\cdot10^{-3}$ s^{-1}	$(0.045\pm0.002)\cdot10^{-3}$ s^{-1}

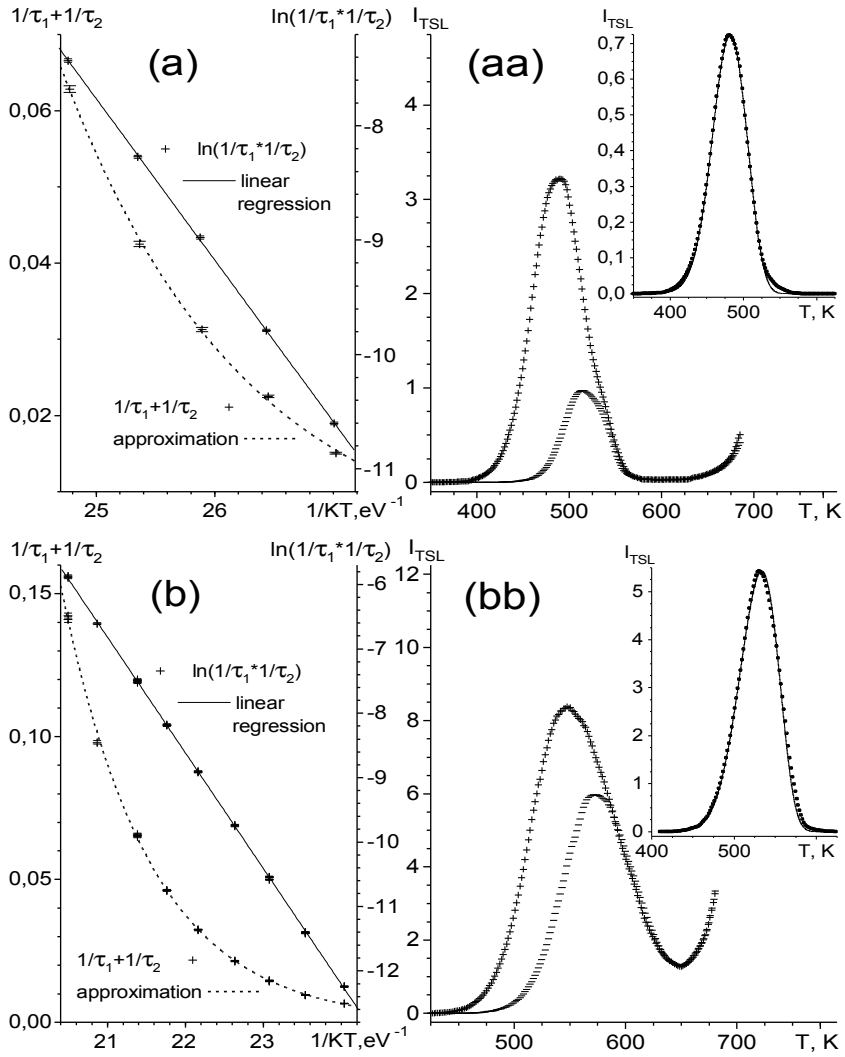

Fig. 18. Kinetics data {(a),(b)} and TSL peak simulation {(aa),(bb)} for $Li_2B_4O_7$:Mn {(a),(aa)} and $Li_2B_4O_7$:Mn,Be {(b),(bb)}. *ln(1/τ1 · 1/τ2)* is plotted as a function of *1/kT* (see equation (3)). Linear regression gives both the sum of activation energies, $E_R + E_T$, and $ln(W_{R0} \cdot W_{T0})$. The sum of reciprocal decay constants (*1/τ1 + 1/τ2*) is plotted against *1/kT*. It is approximated by the sum of two exponents (see equation (4)), with fixed sum of activation energies and fixed product of pre-exponential factors taken from the linear regression. TSL peaks {(aa) and (bb)} recorded after kinetics measurement (– – –) are subtracted from peaks recorded before kinetics measurements (+ + +). The difference peak was used for computer simulation. It is plotted in the insertions with dots (…), and the simulation result is plotted with a solid line (—).

TSL peaks before kinetics measurements (+ + +) and residual after measurements (– – –) are shown in Fig. 18: (aa) for $Li_2B_4O_7$:Mn, and (bb) for $Li_2B_4O_7$:Mn,Be. The residual after kinetics measurements TSL peak (together with thermal background) was subtracted from the initial one to obtain the "purified" TSL peak involved in measured afterglow. Following the model, this TSL peak was digitally simulated, solving the equations by the 4-th order Runge–Kutta method with time substituted for temperature (linear heating, $T = T_0 + \beta \cdot t$). A cloud of random values was generated around each parameter value, then the equations solved for each point in the cloud (Monte-Carlo simulation). The minimal difference between generated TSL peak and experimental curve was used as a criterion to select the best values for any next step. The difference was calculated only for the growing half of TSL peak (the accuracy of subtraction of the residual TSL peak and thermal background was not so good for the high-temperature part of studied peak being undistorted). During the Monte-Carlo calculations, the restrictions were applied: a sum of activation energies $E_T + E_R$ was fixed, and a product of frequency factors $W_{R0} \cdot W_{T0}$ was fixed, too (these parameters were taken from kinetics measurements). Variation of restricted parameters was allowed within the limits of experimental errors. The simulated TSL peaks together with the experimental data (TSL peak obtained after subtraction) are plotted in the insertions (Fig. 18). It is worth to note a surprisingly good accuracy of simulation of TSL peaks. This indicates the applicability of suggested kinetic model for the obtained experimental data. The values of kinetics parameters were improved after peak simulation, they are shown in Table 2 together with the initial values used as a starting point for calculations. The improved values occur mostly in the range of experimental errors of parameters initially determined (errors are large, however, for frequency factors W_{R0} and W_{T0} due to the exponential function). Low errors in final (obtained by TSL peak simulation) values are explained by very large Monte-Carlo flow (1500-2000 points in a cloud). 20 of the best results were selected to obtain average values of parameters and their standard deviations.

As we have mentioned above, the obtained recombination activation energy (E_R) exceeds 1.5-2 times the polaron hopping activation energy of 0.42 eV deduced from paper[101]. This fact is in the accordance with an idea of incomplete screening of positive charges in the vicinity of recombination centre near Mn^{2+} at Li^+ position: the hole hopping activation energy is increased due to a Coulomb force.

We have tried the same Monte-Carlo calculations procedure for the low-temperature peak in $Li_2B_4O_7$:Mn (335-345 K). The result shows a very essential difference for the low-temperature peak compared with the high-temperature one. First, there is no recombination (or hole hopping) activation energy: $E_R = 0$. At the same time, the recombination probability is relatively high ($W_R = 0.15$). Second, the recapturing probability W_C trends to become zero (about 1.4×10^{-16}).

Without a recapturing term, the two combined equations become independent ones and describe a "pure" first-order kinetics. The thermal activation energy of the process ($E_T = 0.45$ eV) is lower than in case of hole release from a trap, and the frequency factor is lower as well ($W_{T0} = 1.14 \times 10^5\ s^{-1}$). All these results indicate that we deal with quasi-intra-centre process, when both a hole and an electron are captured at a small distance, and thermally activated recombination occurs without transport of charge carriers. This would be expected when electron is trapped near Mn^{2+} substituting for Li^+ behind O1 – O3 – O4 oxygen plane of the B – 4O tetrahedron (adjacent to the tetrahedron with Mn^{2+} substituting for B^{3+}). The recombination occurs at O4 oxygen (where a hole is captured) when the wave-functions of the captured hole and the captured electron become overlapped due to a thermal activation of the hole to an excited state. More detailed model, however, will require more experimental and computational data.

X-ray induced absorption and optically stimulated cleaning of traps

X-irradiation causes the $Li_2B_4O_7$-based radiation detectors to acquire absorption bands. One can see the greyish colouring by a naked eye after the doses as large as 10 kGy/cm^2 or higher. The intensity of radiation-induced

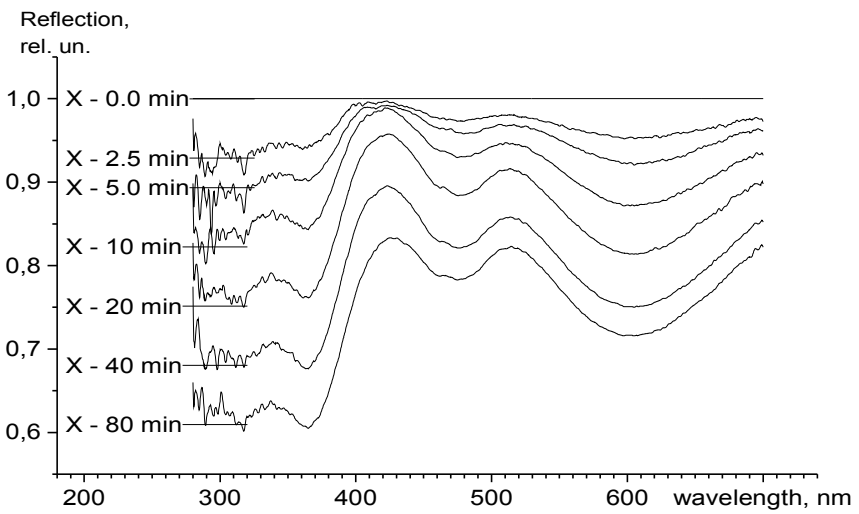

Fig. 19. X-irradiation induced (53 kV, 15 mA, W-anode) absorption bands in $Li_2B_4O_7$:Mn. A tablet was sintered at 1193 K. 1 minute of irradiation corresponds to 1900 Gy/cm^2 of exposition dose. Absorption bands saturation with dose increase correlates with a saturation of a TSL dependence (Fig. 13). Such radiation-induced absorption bands only appear when $Li_2B_4O_7$ is doped with Mn, and disappear after annealing samples above the temperature of dosimetric peaks. However, very high doses require higher temperatures.

absorption bands is proportional both to the dose and to the amount of Mn^{2+} in the sample. A family of reflection curves for different radiation doses is shown for $Li_2B_4O_7$:Mn in Fig. 19.

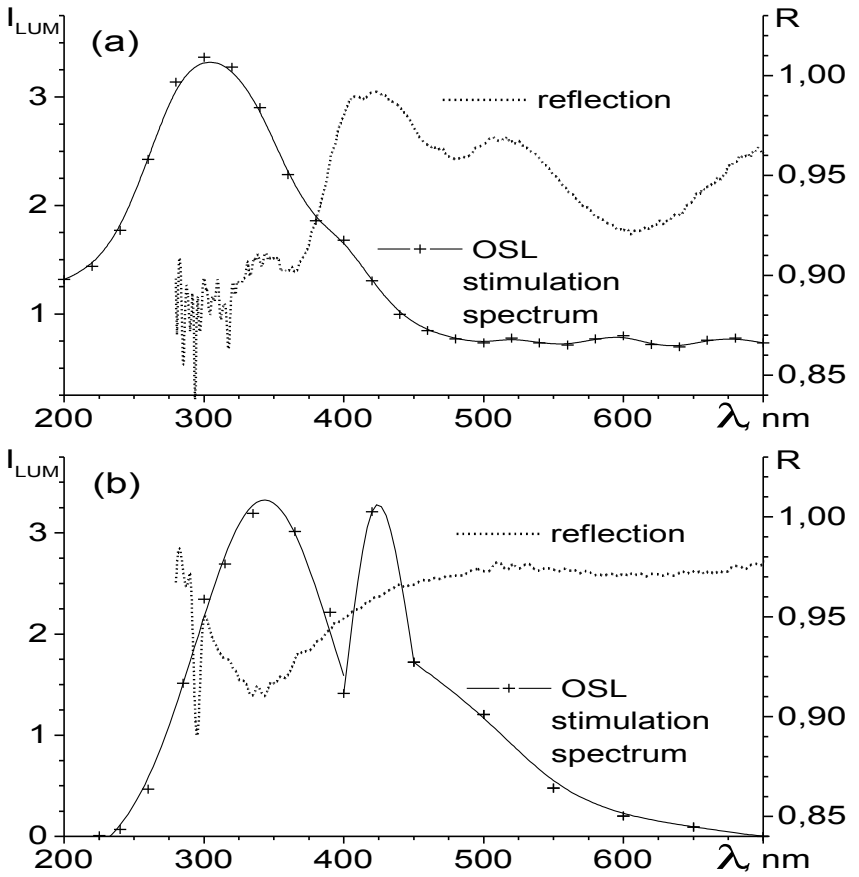

Fig. 20. Normalized reflection spectra (dotted line) after X-irradiation with a dose of 960 Gy/cm^2 for $Li_2B_4O_7$:Mn (a) and $Li_2B_4O_7$:Mn,Be (b). OSL stimulation spectra are shown at the same plots (–+–).

The normalized reflection spectra of the X-irradiated samples (960 Gy/cm^2) are shown in Fig. 20 ((a) for $Li_2B_4O_7$:Mn, and (b) for $Li_2B_4O_7$:Mn,Be). The OSL stimulation spectra are shown at the same plots to compare the absorption and stimulation bands. One can see the correlation of X-ray induced absorption and stimulation bands in the UV region. Both stimulation and absorption bands are shifted towards longer wavelengths in case of $Li_2B_4O_7$:Mn,Be. Also, there is a simpler structure of absorption band in case of $Li_2B_4O_7$:Mn,Be. This could be caused by more complex electronic structures in case of Mn^{2+} at B^{3+} position

compared to the Be^{2+} at B^{3+} site. At the same time, $Li_2B_4O_7$:Mn,Be has an additional narrow stimulation band peaked at 420 nm. We suppose that this additional band is connected with extra high doses (about 10^5 Gy) used for measuring the OSL stimulation spectra. Such high doses caused Mn recharging, and the peculiar stimulation band has appeared. This band is absent in the absorption induced by a two order of magnitude smaller radiation dose. So, this additional sharp band near 420 nm is not appropriate when OSL readout is used for practical doses.

The observed in pure $Li_2B_4O_7$ radiation-induced transient optical absorption bands[101] are similar to the absorption bands in UV region detected in our study for $Li_2B_4O_7$:Mn and $Li_2B_4O_7$:Mn,Be, with the essential difference in the stability: in our case, the radiation-induced absorption bands are stable for months at room temperature. However, in both cases the radiation-induced absorption bands are connected with holes (or polarons[101]). In both cases, this is an absorption of O^- centre, where a hole is captured at O4 oxygen. In our case, the hole is stabilized by Mn^{2+} (or Be^{2+}) substituting for B^{3+}, while the dynamically displaced Li^+ is supposed to stabilize the hole in pure $Li_2B_4O_7$[101]. The absorption should be connected with electron transition from the deeper valence-band layer to the level where a hole is trapped. The deeper valence band layer is connected with BO_3 groups and lies about 2-3 eV below the upper valence band layer[57–59]. The transitions occur from this sub-band to the level with a trapped hole, and the hole is transferred into the deeper sub-band connected with BO_3 groups, where a significant dispersion exists in the band structure[59]. This should cause a hole to acquire certain mobility resulting in hole transfer to a recombination centre. If this model is true, one should observe the cleaning of TSL peaks by proper UV radiation. This effect has been observed in our studies, and thus the radiation-induced absorption bands and OSL stimulation spectra were connected with the observed TSL peaks.

We have tried the irradiation of the excited samples with powerful LEDs emitting quanta exactly in the spectral region of radiation-induced absorption bands. The results are shown in Fig. 21. The low-temperature part of the dosimetric peak is easily cleaned with UV-radiation during one-two hours, while the maximum at higher temperature survives for longer UV-irradiation times. It is interesting to note that a low-temperature TSL peak (335-345 K) studied for $Li_2B_4O_7$:Mn.Be was cleaned out during tens of seconds, thus demonstrating much higher sensitivity to UV-irradiation compared to the dosimetric TSL curve area. The different efficiency of cleaning TSL peaks is in a good agreement with the model based on different relative positions of hole and electron trapping centres. When Mn^{2+} occurs at Li^+ position behind O1 – O3 – O4 oxygen plane of the B – 4O tetrahedron (adjacent to the tetrahedron containing Mn^{2+} instead of B^{3+}), a pronounced fading of corresponding TSL peak (335-345 K) is observed at room temperature, and also, a very fast cleaning of this peak observed when a hole is excited by UV-

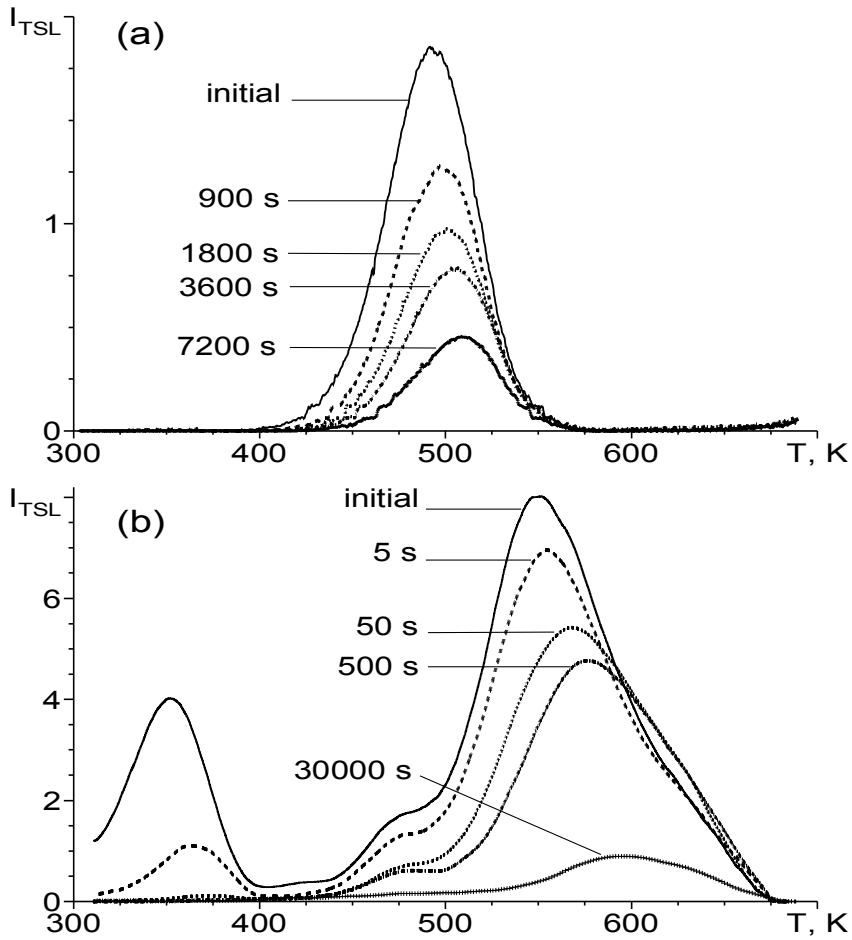

Fig. 21. Optical emptying of traps in $Li_2B_4O_7$:Mn (a) and $Li_2B_4O_7$:Mn,Be (b). Detectors were irradiated before each run with the same dose: $Li_2B_4O_7$:Mn with a dose of 1.5 Gy using the 90Sr/90Y radiation source, and $Li_2B_4O_7$:Mn,Be with a dose of about 0.28 Gy (230 s) using the ^{239}Pu radiation source. $Li_2B_4O_7$:Mn samples were pre-heated at 353 K for 30 min before UV-irradiation (365 nm, 25 mW) to remove the low-temperature peak, while $Li_2B_4O_7$:Mn,Be were immediately subjected to UV-light (395 nm, 95 mW) and then measured after a small pause. The UV-irradiation times are marked at the plots near corresponding TSL curves.

irradiation. The recombination is activated when the hole is either thermally or optically promoted to an excited state, with the wave-functions of the excited hole and the trapped electron being overlapped. When Mn^{2+} is located at Li^+ site after O2 (near a BO_3 plane), we have the "dosimetric" electron trap being cleaned due to recombination with a hole delivered either by thermal activation

or by optical stimulation. The electron traps of this kind are situated at two different distances. The more remote is Mn^{2+} at Li^{+} position from the captured at O4 hole, the higher is TSL maximum, and the more time is required to clean it optically. This indicates that optically stimulated release of a hole from a trap is insufficient for effective hole transport to recombination centre. A hole still needs an additional energy to overcome a hopping barrier. Hence, a thermo-optical stimulation should be studied for $Li_2B_4O_7$:Mn, with optical stimulation and simultaneous heating to temperatures close to 370 K to provide hole hopping activation.

Conclusive remarks on $Li_2B_4O_7$:Mn and $Li_2B_4O_7$:Mn.Be

The studied ceramic radiation detectors $Li_2B_4O_7$:Mn and $Li_2B_4O_7$:Mn,Be contain mostly polycrystalline lithium tetraborate, with the amount of glass phase being negligible. To avoid light-induced false dose, one needs to avoid the presence of Mn^{2+} in the glass phase. Usually this can be achieved by increasing temperature of sintering. The incorporation of Mn into the lattice structure of $Li_2B_4O_7$ is possible both at Li^{+} sites and at B^{3+} tetrahedral positions. The latter is possible due to the adaptation of the size of oxygen tetrahedron by displacement of bridging oxygen connecting two adjacent BO_4 tetrahedra. Two different luminescence bands observed for different TSL peaks[68] belong to these two different Mn^{2+} centres.

The different temperature dependences of observed EPR signals belonging to Mn^{2+} helped to reveal the two types of Mn^{2+} centres with different local surroundings. To prove the presence of Mn^{2+} at B^{3+} tetrahedral positions, an analogy with BeO:Mn^{2+} for the HFS value[70] is useful, due to the HFS splitting values for Mn^{2+} in BeO and in $Li_2B_4O_7$ being similar. EPR studies of Mn^{2+} in $Li_2B_4O_7$:Mn and $Li_2B_4O_7$:Mn,Be showed the suppression of Mn^{2+} at B^{3+} position in the presence of Be^{2+}, and also the increase of Mn^{2+} clusterization in which Mn^{2+} ions substituting for Li^{+} are involved, instead of increasing the number of isolated Mn_{Li} centres.

A hole is captured at O4 (the bridging oxygen of two adjacent BO_4 tetrahedra) when one of two adjacent tetrahedra contains Mn^{2+} instead of B^{3+}. The red luminescence of Mn^{2+} at B^{3+} tetrahedral position is actually a thermally activated quasi-intra-centre recombination. It occurs when the captured at O4 hole is recombined with an electron captured at closely situated electron trap. This trap is caused by Mn^{2+} at Li^{+} site behind O1 – O3 – O4 oxygen plane of the B – 4O tetrahedron adjacent to the tetrahedron containing Mn^{2+} instead of B^{3+}. The recombination is activated when the hole is thermally promoted to an excited state, with the wave-functions of the excited hole and the trapped electron being overlapped. The orange luminescence of Mn^{2+} at Li^{+} position occurs when a hole (released from O4 in case of TSL) recombines with an electron captured near Mn^{2+} situated at a more distant Li^{+} position from O4. There are two slightly different Mn^{2+} positions involved, both are situated at Li^{+}

site after oxygen O2 (near a BO_3 plane, see Fig. 3(a)). The electronic trapping level is connected with antibonding BO_3 orbital split off from the bottom of conduction band due to extra positive charge of Mn^{2+} at Li^+ position. Both luminescence bands (the red one and the orange one) can be attributed to $^4T_1 - {}^6A_1$ radiative transitions of Mn^{2+} in two different distorted tetrahedral environments.

The basic (dosimetric) TSL peak in $Li_2B_4O_7$:Mn is connected with the release of holes and occurs at 470-510 K. In case of $Li_2B_4O_7$:Mn,Be, this peak is essentially suppressed in favour of new intensive group of maxima created in the range of 525-625 K. Compared to $Li_2B_4O_7$:Mn, the deeper hole trap is formed in $Li_2B_4O_7$:Mn,Be at O4 when Be^{2+} is substituting for B^{3+}. Be^{2+} occupies the positions of tetrahedral B^{3+} much more efficiently than Mn^{2+}. This causes the amount of Mn^{2+} at the position of B^{3+} to decrease, and the amount of Mn^{2+} at the position of Li^+ to increase, respectively. This fact is supported also by comparative EPR studies of $Li_2B_4O_7$:Mn and $Li_2B_4O_7$:Mn,Be.

The TSL kinetics studied both for $Li_2B_4O_7$:Mn and $Li_2B_4O_7$:Mn,Be show a bi-exponential decay at each temperature point. A simple quasi-intra-centre model is suggested to account for the observed data, with side recombinations being neglected, and hole hopping barrier taken into account. The dosimetric TL peak was digitally simulated on the basis of suggested model, and the simulation results are almost coinciding with the experimental data. Kinetics parameters were determined in the frame of suggested model (see Table 2). The results demonstrated an increased barrier for the released hole hopping towards the recombination centre. This is in accordance with the suggested structural model: the captured near Mn_{Li} electron does not provide a complete screening of Mn^{2+} positive charge, so an additional Coulomb repelling force is expected which increases the “normal” polaron hopping activation energy.

The low-temperature TSL peak (335-345 K) with the red Mn^{2+} luminescence shows a "pure" first-order kinetics and occurs without hole hopping and without recapturing. The activation energy ($E_T = 0.45$ eV) is lower than in case of hole release. The close $Mn_B - Mn_{Li}$ pair is responsible for this peak, with a hole trapped at O4 bridging oxygen and an electron trapped near Mn^{2+} at Li^+ site behind O1 – O3 – O4 oxygen plane of the closest B – 4O tetrahedron (adjacent to that one containing Mn^{2+} instead of B^{3+}). The trapped electron occupies an antibonding BO_3 orbital split off the bottom of the conduction band. The wave-functions of the electron and the captured at O4 hole overlap each other with temperature increase, and the recombination occurs at O4, with the energy being transferred to Mn^{2+} at B^{3+} position yielding the red luminescence band.

The radiation-induced absorption bands and OSL stimulation spectra were studied both for $Li_2B_4O_7$:Mn and $Li_2B_4O_7$:Mn,Be. The absorption bands in UV region correlate with OSL stimulation spectra. OSL stimulation maximum is shifted towards longer wavelengths by 30-40 nm in case of $Li_2B_4O_7$:Mn,Be. The optical emptying of traps has been observed by stimulation with powerful LEDs

at corresponding wavelengths. The efficient cleaning of dosimetric TSL peaks requires additional energy for hole hopping activation. The obtained results will be useful for practical application of $Li_2B_4O_7$:Mn and $Li_2B_4O_7$:Mn,Be in dosimetry with OSL readout.

The arising of Mn^{2+} centres of two types in $Li_2B_4O_7$:Mn, and hence, the creation of suitable for dosimetry system of traps, entirely depends on the redox transformations of manganese. Here we have a possibility to try proper co-activators providing more control over the luminophor formation process.

SUMMARY

The studies of EPR and luminescence spectra, TSL, optically stimulated cleaning of TSL peaks, kinetics, radiation-induced absorption, and magnetic susceptibility of storage phosphors, and also an extensive analysis of the previously published information, have revealed the basic energy storage mechanisms in the practically important dosimetric materials: $SrSO_4$:Eu, CaF_2:Mn, $Li_2B_4O_7$:Mn.

The trapping centres in $SrSO_4$:Eu are connected with $(SO_4)^{2-}$ anions capturing either holes or electrons depending on the effective charge of lattice defect in their close vicinity. Eu is shown to enter the lattice both in divalent and trivalent state, with divalent one being recognized by EPR and luminescence, while a trivalent one being deduced from magnetic susceptibility measurements. The Eu^{3+} is created due to uncontrolled redox reactions at the moment of solid solution formation. Eu^{3+} plays a very essential role, dominating in the samples with the total amount of Eu exceeding 0.1 m %. With charge-compensation by cation vacancies, Eu^{3+} is responsible for closely spaced traps of the both sign: a hole is trapped at $(SO_4)^{2-}$ near a cation vacancy forming an axial $(SO_4)^{-}$ centre, while an electron is captured near Eu^{3+} at antibonding orbital of $(SO_4)^{2-}$ thus forming stable at high temperatures $(SO_4)^{3-}$ centre. The recombination of released either by heating or by optical stimulation holes occurs at the electronic traps, with the Eu^{2+} being excited by resonance energy transfer. Then, the luminescence of Eu^{2+} occurs. To improve the linearity range of dose-response, the idea to find the complementary redox partners for Eu is suggested. While Eu^{3+} acting as an oxidizer, some other rare-earth impurity should do as a reducer. As a result, a predictable ratio between the amounts of Eu^{2+} and complementary trivalent impurity would be obtained, being less dependent on casual conditions. The improvement of structure of complex trapping centres is expected due to a controlled formation of the luminophor structure.

The mechanism of energy storage and release in CaF_2:Mn is connected with rather ionic than electron-hole processes. At the first stage, Mn^{2+} is excited to a ^6D ($3d^4 4s$) excited level by a resonance energy transfer from "hot" excitons or electron-hole pairs transferring energy at the stage of thermalisation. The excited Mn^{2+} has an increased ionic radius, and shifts one of the closest fluorine atoms. The ^6D ($3d^4 4s$) excited state of Mn^{2+} is then deactivated nonradiatively, transferring energy to the shifted fluorine and thus creating a pair of F-centre and H-centre (an anion vacancy with a trapped electron and an interstitial fluorine). An interstitial fluorine either returns back to a vacancy or moves to an adjacent lattice cell where another interstitial fluorine is present as a charge-compensator for Mn^{3+} (both Mn^{2+} and Mn^{3+} are present in CaF_2 one near another in some ordered clusters). Two fluorine atoms form an interstitial molecule and release an electron (if there was initially a F^- at the interstitial position). The released electron is trapped by an anion vacancy (ordered pairs of anion

vacancies and interstitial F^- arise usually around the trivalent impurities). The stability of formed interstitial F_2 molecule depends on how much its' electronic cloud overlaps with that of the regular fluorine anions. The lower Mn concentration is, the smaller clusters are formed with the smaller free space available to place the F_2 molecules. When temperature increases, the molecule dissociates, and one of the fluorine atoms returns to the place from where fluorine has been removed due to irradiation. Ionic recombination produces energy which is transferred to Mn^{2+} driving it to a first excited state $^4T_{1g}$ (^4G) which is then radiatively deactivated giving the luminescence. The model is proved by kinetics measurements showing a quasi-intra-centre process with an activation energy (1.597 eV) being too high for CaF_2. The activation energy of dosimetric peak almost coincides with the thermal dissociation energy of a free F_2 molecule (1.606 eV). Also, both the OSL excitation band and radiation-induced UV band in CaF_2:Mn are very close to the first broad absorption band of the F_2 molecule. The values of kinetics parameters were obtained from isothermal decay curves and checked by digital simulation of the TSL peak. The retrapping probability is shown to be very high (0.011 s^{-1}) thus impeding the process of energy release, especially in case of optical stimulation at room temperature. The main problem of CaF_2:Mn thermoluminescent detectors is that the most uniform TSL peak with the highest temperature of maximum is obtained in the material with the concentration of Mn being close to the decomposition threshold of the solid solution. We suggest to find the redox-complementary rare-earth ions for Mn in order to improve the ordered structure of complex impurity clusters. Mn^{2+} will be responsible for the first step of energy storage and for the last stages of energy release, while the trivalent rare-earth impurity will be responsible for ordered structure with a suitable space for a F_2 molecule adaptation. At present, a certain ratio between Mn^{2+} and Mn^{3+} is formed by some intrinsic redox reaction which is hard to control. We suggest the way to control such reaction by introduction of complementary ions, thus improving the structure of the thermoluminophor.

Due to redox reaction at a moment of solid solution formation, manganese enters $Li_2B_4O_7$ lattice in two different positions, both in cationic and in anionic sublattice. At the first stage of synthesis, Mn^{3+} occurs in oxygen tetrahedron similar to BO_4 structure. Containing Mn^{3+} tetrahedra become a part of crystal lattice. Ceramics sintering causes partial transformation of Mn^{3+} to Mn^{2+}, with the higher part of Mn being reduced at higher sintering temperatures. As a result, one-half of formed Mn^{2+} leaves tetrahedral structures and substitutes for Li^+, providing charge compensation for the retained in oxygen tetrahedra Mn^{2+}. This mechanism creates self-compensated Mn^{2+} pairs. The total amount of Mn^{2+} increases with sintering temperature increase, whit the amounts of Mn^{2+} at B^{3+} positions and Mn^{2+} at Li^+ positions being always equal. The two types of Mn^{2+} centres have been distinguished both by their luminescence and EPR spectra. The presence of Mn^{2+} at tetrahedral B^{3+} position has been proved by observing a

hyperfine splitting constant value close to that for Mn^{2+} in BeO (where Mn^{2+} is substituting for Be^{2+} at a small site with a tetrahedral symmetry). A tetrahedral structures in lithium tetraborate are less rigid compared to BeO. They can be slightly adapted to Mn size due to a movable bridging oxygen connecting two tetrahedra in $Li_2B_4O_7$ lattice. This oxygen becomes an effective hole trap when Mn^{2+} is present instead of B^{3+} in one of the two adjacent tetrahedra. The electronic trapping level is connected with antibonding BO_3 orbital split off from the bottom of conduction band due to extra positive charge of Mn^{2+} at Li^+ position. Depending on the distance between the electronic and the hole traps, two different recombination mechanisms are suggested. From the four possible positions only three are playing role in thermoluminescence, while the closest position being too tight and impossible. The closest suitable position of electronic trap occurs just behind the oxygen plane of the adjacent tetrahedron which do not contain Mn^{2+} instead of B^{3+}. When temperature increases, a captured at bridging oxygen hole is thermally promoted to an excited state, with the wave-functions of the excited hole and the trapped electron being overlapped. The recombination is activated at the bridging oxygen, and thus, the energy is transferred to Mn^{2+} at the B^{3+} position yielding a red luminescence band. The corresponding thermoluminescence peak (335-345 K) shows a "pure" first-order kinetics and occurs without hole hopping and without retrapping. The activation energy (E_T = 0.45 eV) is lower than in case of hole release. When the traps are situated more remotely from each other, recombination occurs near the electronic trap after a hole having released, with the energy being transferred to the Mn^{2+} at Li^+ position. The corresponding TSL peak yields an orange luminescence band. TSL peak maximum occurs at a temperature of 470-510 K. In case of $Li_2B_4O_7$:Mn,Be, this peak is essentially suppressed in favour of new intensive group of maxima created in the range of 525-625 K. Compared to $Li_2B_4O_7$:Mn, the deeper hole trap is formed in $Li_2B_4O_7$:Mn,Be at bridging oxygen when Be^{2+} is substituting for B^{3+}. Be^{2+} occupies the positions of tetrahedral B^{3+} much more efficiently than Mn^{2+} and supplants Mn^{2+} from B^{3+} tetrahedral positions when $Li_2B_4O_7$:Mn is co-doped with Be. Both luminescence bands (the red one and the orange one) can be attributed to $^4T_1$–$^6A_1$ radiative transitions of Mn^{2+} in two different distorted tetrahedral environments. The TSL kinetics studied both for $Li_2B_4O_7$:Mn and $Li_2B_4O_7$:Mn,Be show a bi-exponential decay at each temperature point. A simple quasi-intra-centre model is suggested to account for the observed data, with side recombinations being neglected, and hole hopping barrier taken into account. The dosimetric TSL peak was digitally simulated on the basis of suggested model, and the simulation results are almost coinciding with the experimental data. Kinetics parameters were determined in the frame of suggested model, both for $Li_2B_4O_7$:Mn and $Li_2B_4O_7$:Mn,Be. The results demonstrated an increased barrier for the released hole hopping towards the recombination centre. This is in accordance with the suggested structural model: the captured near Mn_{Li} electron does not provide a complete screening

of Mn^{2+} positive charge, so an additional Coulomb repelling force is expected which increases the "normal" polaron hopping activation energy. The radiation-induced absorption bands and OSL stimulation spectra were studied both for $Li_2B_4O_7$:Mn and $Li_2B_4O_7$:Mn,Be. The absorption bands in UV region correlate with OSL stimulation spectra. OSL stimulation maximum is shifted towards longer wavelengths by 30-40 nm in case of $Li_2B_4O_7$:Mn,Be. The optical emptying of traps has been observed by stimulation with powerful LEDs at corresponding wavelengths. The efficient cleaning of dosimetric TSL peaks requires additional energy for hole hopping activation. The obtained results will be useful for practical application of $Li_2B_4O_7$:Mn and $Li_2B_4O_7$:Mn,Be in dosimetry with OSL readout.

In general, a good storage phosphor can be obtained when the redox transformations of doped luminescent impurities occur at the moment of solid solution formation in the way providing closely spaced electronic and hole traps — without overlapping, however, of the wave-functions of trapped carriers. The three different materials considered in present work demonstrate very interesting particular realizations of this basic principle.

REFERENCES

1 Jacobsen, S. D.; Sfyth, J. R.; Swope, R. J.; Downs, R. T. *Can. Mineral.* **1992**, *s6*, 1053.
2 Antao, S. M. *Am. Mineral.* **2012**, *97*, 661.
3 Ozawa, T.C.; Kang, S.J. *J. Appl. Cryst.* **2004**, *s7*, 679.
4 Zhuravlev, Yu. N.; Zhuravleva, L. V.; Poplavnoy, A. S. *Russ. Phys. J.* **2003**, *46*, 75.
5 Savikhin, F.; Kerikfäe, M.; Feldbach, E.; Lushchik, A.; Onishchik, D.; Rakhifov, D.; Tokbergenov, I. *Phys. Stat. Sol. (c)* **2005**, *2*, 252.
6 Tokbergenov, I.; Feldbach, E.; Kerikfäe, M.; Lushchik, A.; Nagirnyi, V.; Nurakhfetov, T.; Savikhin, F.; Vasil'chenko, E. *Radiat. Eff. Defect S.* **1999**, *150*, 103.
7 Tang, Q.; Zhang, C. X.; Luo, D. L.; Leung, P. L.; Xiong, Z. Y. *Radiat. Prot. Dosim.* **2006**, *119*, 238.
8 Van der Kolk, E.; Dorenbos, P.; Vink, A. P.; Perego . R. C.; van Eijk, C. W. E. *Phys. Rev. B* **2001**, 64, 195129 .
9 Morgan, M. D.; Stoebe, T. G. *Radiat. Prot. Dosim.* **1926**, *17*, 455.
10 Gérôfe, V.; Lapraz, D.; Iacconi, P.; Benabdesselaf, M.; Prévost, H.; Baufer, A. *Radiat. Prot. Dosim.* **1999**, *84*, 109.
11 Madhusoodanan, U.; Jose, M. T.; Lakshfanan, A. R. *Radiat. Meas.* **1999**, *s0*, 65.
12 Seshagiri, T. K.; Dalvi, A. G. I.; Sastry, M. D. *J. Phys C Solid State* **1922**, *21*, 5891 .
13 Dalvi, A. G. I.; Sastry, M. D.; Seshagiri, T. K.; Joshi , R.D. *J. Phys C Solid State* **1924**, *17*, 5865 .
14 Salah, N.; Sahare, P. D.; Kufar, P. *Phys. Stat. Sol. (a)* **2006**, *20s*, 898 .
15 Bhatt, B. C.; Dhabekar, B.; Kufar, R.; Gundu Rao, T. K.; Lakshfanan. A. R. *Radiat. Prot. Dosim.* **2006**, *119*, 53.
16 Ryabov, I. D.; Bershov, L. V.; Speranskiy, A. V.; Ganeev, I. G. *Phys. Chem. Miner* . **1923**, *10*, 21.
17 Ryabov, I. D. *Phys. Chem. Miner* . **1995**, *22*, 406.
18 Jesus, E. F. O.; Rossi , A. M.; Lopes, R. T. *Radiat. Prot. Dosim.* **2002**, *101*, 553.
19 Tang, Q.; Zhang C. X.; Luo, D. L.; Leung, P. L.; Xiong, Z. Y. *Radiat. Prot. Dosim.* **2006**, *119*, 238.
20 Sun, J.; Sun, R.; Du, H. *J. Alloy. Compd.* **2012**, *516*, 201.
21 Sun, J.; Sun, R.; Xia, Z.; Du, H. *CrystEngComm*, **2012**, *14*, 1111.
22 Shi, H.; Eglitis, R. I.; Borstel, G. *Phys. Rev. B* **2005**, *72*, 045109 .
23 Letz, M.; Parthier, L. *Phys. Rev. B* **2006**, 74, 064116 .

24 Rubloff , G. W. *Phys. Rev. B* **1972**, *5*, 662.
25 Atobe, K. *J. Chem. Phys.* **1979**, *71*, 2588.
26 Patel, J. L.; Cavenett, B.C.; Davies, J. J.; Hagston, W. E. *Phys. Rev. Lett.* **1974**, *33*, 1300.
27 Caldiño, U.; Muñoz, A. F.; Rubio, J. O. *J. Phys-Condens. Mat.* **1990**, *2*, 6071.
28 Caldiño, U. *J. Phys-Condens. Mat.* **2003**, *15*, 7127 .
29 Jassemnejad, B.; Abbundi, R. J.; Brown, M. D.; McKeever, S. W. S. *Phys. Stat. Sol. A* **1988**, *108*, 753 .
30 Hamers, R. J.; Wietfeldt, J. R.; Wright, J. C. *J. Chem. Phys.* **1982**, *77*, 683.
31 Cirillo-Penn, K. M.; Wright, J. C. *Phys. Rev. B* **1990**, *41*, 10799.
32 Cirillo-Penn, K. M.; Wright, J. C. *J. Lumin.* **1991**, *48-49*, 505.
33 Schulman, J. R.; Ginther, R. J.; Kirk, R. D.; Goulart, H. S. *Nucleonics*, **1960**, *18*, 92.
34 Fehl, D. L.; Muron, D. I.; Suijka, B. R.; Vehar, D. W.; Lorence, L. I.; Westfall, R. L.; Jones, S. C.; Sweet, I. A.; Braunlich , P. *Rev. Sci. Instrum.* **1994**, *65*, 3243.
35 Jain, V. K. *Radiat. Phys. Chem.* **1990**, *36*, 47 .
36 Alonso, P. J.; Alcala, R. *J. Lumin.* **1980**, *21*, 147.
37 Alcala, R.; Alonso, J. P.; Lalinde, G.; Carretero, A. *Phys. Stat. Sol. (b)* **1980**, *98*, 315.
38 Alonso, P .J.; Orera, V. M.; Alcala, R. *Phys. Stat. Sol. (b)* **1980**, *99*, 585 .
39 Alonso, P. J.; Alcala, R. *J. Lumin.* **1981**, *22*, 321.
40 Jain, V. K.; Shah Jahan, M. *Phys. Stat. Sol. (b)* **1985**, *131*, K161.
41 Jassemnejad, B.; McKeever, S. W. S.; Abbundi, R. J.; Mathur, V. K.; Brown, M. D. *Radiat. Prot. Dosim.* **1986**, *17*, 469.
42 McKeever, S. W. S.; Jassemnejad, B.; Landreth, J. F.; Brown, M. D. *J. Appl. Phys.* **1986**, *60*, 1124 .
43 Denks, V. P.; Kerikmyaé, M. P.; Lust, A. L.; Savikhina, T. I. *Phys. Solid State* **2000**, *42*, 261.
44 Barriuso, M. T.; Moreno, M. *Chem. Phys. Lett.* **1984**, *112*, 165.
45 Barkoumb, J. H.; Mansour, A. N. *Phys. Rev. B* **1992**, *46*, 8768 .
46 Pascual. J. L.; Seijo, L. J. Chem. Phys. 1995, 102.
47 Danilkin, M.; Lust, A.; Kerikmäe, M.; Seeman, V.; Mändar, H.; Must, M. *Radiat. Meas.* **2006**, *41*, 677 .
48 Allen, P.; McKeever. S. W. S. *Radiat. Prot. Dosim.* **1990**, *33*, 19.
49 Jaek, I.; Kerikmae, M.; Lust, A. *Radiat. Prot. Dosim.* **2002**, *100*, 459.
50 El-Faramawy, N. A.; Göksu, H. Y.; Panzer, W. *J. Radiol. Prot.* **2004**, *24*, 273.

51 Mobit, P.; Agyingi, E.; Sandison, G. *Radiat. Prot. Dosim.* **2006**, *119*, 497.
52 Maia, A. F.; Caldas, L. V. E. *Appl. Radiat. Isotopes* **2010**, *68*, 780.
53 Selvam, T. P.; Keshavkumar, B. *J. Appl. Clin. Med. Phys.* **2010**, *11(4)*, 70.
54 Sennova, N.; Bubnova, R.; Shepelev, Yu.; Filatov, S.; Yakovleva, O. *J. Alloy. Compd.* **2007**, *428*, 290.
55 Gorelik, V. S.; Vdovin, A. V.; Moiseenko, V. N. *J. Russ. Laser Res.* **2003**, *24*, 553.
56 Kuznetsov, A. Yu.; Kruzhalov, A. V.; Ogorodnikov, I. N.; Sobolev, A. B.; Isaenko, L. I. *Phys. Solid State* **1999**, *41*, 48.
57 Maslyuk, V. V.; Islam, M. M.; Bredow, T. *Phys. Rev. B* **2005**, *72*, 125101.
58 Islam, M. M.; Maslyuk, V. V.; Bredow, T.; Minot, C. *J. Phys. Chem. B* **2005**, *109*, 13597.
59 Adamiv, V. T.; Burak, Ya. V.; Wooten, D. J.; McClory, J.; Petrosky, J.; Ketsman, I.; Xiao, J.; Losovyj, Ya. B.; Dowben, P. A. *Materials* **2010**, *3*, 4550.
60 Wooten, D.; Ketsman, I.; Xiao, J.; Losovyj, Ya. B.; Petrosky, J.; McClory, J.; Burak, Ya. V.; Adamiv, V. T.; Brown, J. M.; Dowben, P. A. *Eur. Phys. J. Appl. Phys.* **2010**, *52*, 31601.
61 Swinney, M. W.; McClory, J. W.; Petrosky, J. C.; Yang, Sh.; Brant, A. T.; Adamiv, V. T.; Burak, Ya. V.; Dowben, P. A.; Halliburton, L. E. *J. Appl. Phys.* **2010**, *107*, 113715.
62 Corradi, G.; Watterich, A.; Polgár, K.; Nagirnyi, V.; Hofstaetter, A.; Rakitina, L. G.; Meyer, M. *Phys. stat. sol. (c)* **2007**, *4*, 1276.
63 Corradi, G.; Nagirnyi, V.; Kotlov, A.; Watterich, A.; Kirm, M.; Polgár, K.; Hofstaetter, A.; Meyer, M. *J. Phys. Condens. Mat.* **2008**, *20*, 025216.
64 Corradi, G.; Nagirnyi, V.; Watterich, A.; Kotlov, A.; Polgár, K. *J. Phys. Conf. Ser.* **2010**, *249*, 012008.
65 Podgórska, D.; Kaczmarek, S. M.; Drozdowski, W.; Wabia, M.; Kwaśny, M.; Warchoł, S.; Rizak, V. M. *Molecul. Phys. Rep.* **2004**, *39*, 199.
66 Kelemen, A.; Ignatovych, M.; Holovey, V.; Vidoczy, T.; Baranyai, P. *Radiat. Phys. Chem.* **2007**, *76*, 1531.
67 Podgórska, D., Kaczmarek, S.M., Drozdowski, W., Berkowski, M., Worsztynowicz, A. *Acta Phys. Pol. A* **2005**, *107*, 507.
68 Holovey, V. M.; Popovich, K. P.; Goyer, D. B.; Krasylynets, V. M.; Gomonnai, A. V. *Radiat. Eff. Defect. S.* **2011**, *166*, 522.
69 Rawat, N. S.; Kulkarni, M. S.; Tyagi, M.; Ratna, P.; Mishra, D. R.; Singh, S. G.; Tiwari, B.; Soni, A.; Gadkari, S. C.; Gupta, S. K. *J. Lumin.* **2012**, *132*, 1969.

70 Kerikmäe, M.; Danilkin, M.; Lust, A. Pat. appl. of University of Tartu. Priority: 29.01.2010. Intern. Public. Nr. WO 2011/091803 A1.
71 Lust, A.; Paama, L.; Kerikmäe, M.; Must, M.; Perämäki, P. *Proc. Est. Acad. Sci. Chem.* **2002**, *51*, 126.
72 Mändar, H.; Felsche, J.; Mikli, V.; Vajakas, T. *J. Appl. Crystallogr.* **1999**, *32*, 345.
73 Rodriguez-Carvajal, **1997**. J. FULLPROF version 3.5. Laboratoire Leon Brillouin (CEA-CNRS), F-91191 Gif sur Yvette, France (http://www.ill.eu/sites/fullprof/php/reference.html).
74 Beck, W.; Fedorov, V. V.; Ricard, D.; Flytzanis ,C.; Basiev, T. T. *J. Lumin.* **1998**, *79*, 241.
75 Nauta-Leeffers, Z. C.; den Hartog, H. W. *Phys. Rev. B* **1979**, *19*, 4162.
76 Yang, J.; Hao, Y.; Li, J.; Zhou, Ch.; Mo, Yu. *J. Chem. Phys.* **2005**, *122*, 134308.
77 Steunenberg, R. K.; Vogel, R. C. *J. Am. Chem. Soc.* **1956**, *78*, 901.
78 Abrahams, S. C.; Bernstein, J .L.; Gibart, P.; Robbins, M.; Sherwood, R. C. *J. Chem. Phys.* **1974**, *60*, 1899.
79 Sadanaga, R.; Nishimura, T.; Watanabe, T. *Mineralogical Journal* **1965**, *4*, 380.
80 Norrestam, R., Kritikos, M., Sjödin, A. *J. Solid State Chem.* **1995**, *114*, 311.
81 Smith, D.K.; Cline, C. F.; Austerman, S. B. *Acta Cryst.*, **1965**, *18*, 393.
82 Milsch, B.; Kerbe, F. *Phys. stat. sol. (a)* **1987**, *103*, K141.
83 Holovey, V. M.; Sidey, V. I.; Lyamayev, V. I.; Birov, M. M. *J. Phys. Chem. Solids,* **2007**, *68*, 1305.
84 Prokic, M. *Rad. Prot. Dosim.* **2002**, *100*, 265.
85 Takenaga, M.; Yamamoto, O.; Yamashita, T. *Nucl. Instrum. Methods.* **1980**, *175*, 77.
86 Sristava, J. K.; Supe, S. J. *J. Phys. D* **1989**, *22*, 1537.
87 Christensen, P. Risó Report N.161, **1967**.
88 Gesell, T. F. *Transactions on Nuclear Science* **1982**, *NS-29*, 1225.
89 Biernacki, S.; Kutrowski, M.; Karczewski, G.; Wojtowicz, T.; Kossut, J. *Semicond. Sci. Technol.* **1996**, *11*, 48.
90 Duan, C. J.; Delsing, A. C. A.; Hintzen, H. T. *Chem. Mater.* **2009**, *21*, 1010.
91 Griscom, D. L.; Griscom, L. E. *J. Chem. Phys.* **1967**, *47*, 2711.
92 Ardelean, I.; Peteanu, M.; Mureşan, N.; Ioncu, V.; Ciorcas-Delille, F. *J. Optoelectron. Adv. M.* **2005**, *7*, 2661.
93 Shkrob, I. A.; Tadjikov, B. M.; Trifunac, A. D. *J. Non-cryst. Solids* **2000**, *262*, 6.

94 Rizak, I. M.; Rizak, V. M.; Baisa, N. D.; Bilanich, V. S.; Boguslavskii, M. V.; Stefanovich, S. Yu.; Golovei, V. M. *Crystallogr. Rep.* **2003**, *48*, 676.
95 Burak, Ya. V.; Padlyak, B. V.; Shevel, V. M. *Radiat. Eff. Defect. S.* **2002**, *157*, 1101.
96 Lian, J. C.; Finazzi, E.; Di Valentin, C.; Risse, T.; Gao, H.-J.; Pacchioni, G.; Freund, H.-J. *Chem. Phys. Lett.* **2008**, *450*, 308.
97 Ogorodnikov, I. N.; Pustovarov, V. A.; Kruzhalov, A. V.; Isaenko, L. I.; Kirm, M.; Zimmerer, G. *Phys. Solid State* **2000**, *42*, 464.
98 Deskins, N. A.; Dupuis, M. *J. Phys. Chem. C* **2009**, *113*, 346.
99 Jain, H.; Issa, A.; Anavekar, R. V.; Böhmer, R., Kanert, O., Küchler, R. *Appl. Phys. Lett.* **2009**, *95*, 142908.
100 Khalil, M. M. I. *Appl. Phys. A-Mater.* **2007**, *86*, 505.
101 Ogorodnikov, I. N.; Poryvay, N. E.; Pustovarov, V. A. *IOP Conf. Ser.: MSE* **2010**, *15*, 012016.

SUMMARY IN ESTONIAN

Energia salvestamine ja ülekanne dosimeetrilistes luminestsentsmaterjalides

Selgitati välja praktilises kasutamises tähtsate dosimeetriliste materjalide $SrSO_4$:Eu, CaF_2:Mn ja $Li_2B_4O_7$:Mn peamised energia salvestamise mehhanismid. Selleks uuriti nende fosfooride EPR ja luminestsentsi spektreid, TSL ja selle optilist kustutamist, TSL signaali kustumise kineetikat, kiirguslikult indutseeritud neeldumist ja magnetilist vastuvõtlikkust, mida võrreldi varempublitseeritud informatsiooniga.

Haardetsentrid materjalis $SrSO_4$:Eu on seotud $(SO_4)^{2-}$ anioonidega, mis sõltuvalt nende lähiümbruse kristallvõre defektide efektiivsest laengust haaravad kas elektrone või auke. Näidati, et Eu on kristallvõres nii laenguolekus Eu^{2+}, mida kinnitavad EPR ja luminestsentsispektrid kui ka laenguolekus Eu^{3+}, nagu järeldati magnetilise vastuvõtlikkuse mõõtmisest. Tahke lahuse moodustumisel tekib Eu^{3+} kontrollimatute redoksreaktsioonide käigus, mängides tähtsat osa ja domineerides üle 0,1 m% Eu sisalduse korral näidistes. Koos katioonvakantside laengukompensatsiooniga on Eu^{3+} vastutav lähedalpaiknevate mõlema märgiga haardenivoode eest. Auk haaratakse katioonvakantsi lähedal paikneva $(SO_4)^{2-}$ juures moodustades telgsümmeetrilise $(SO_4)^{-}$ tsentri, kuna aga elektron haardub Eu^{3+} lähedal paikneva $(SO_4)^{2-}$ juures moodustades kõrgetel temperatuuridel stabiilse $(SO_4)^{3-}$ tsentri. Soojuslikult või optiliselt vabastatud aukude relaksatsioon toimub elektrontsentril energia resonantsülekandega Eu^{2+}-le, kust energia vabaneb luminestsentsina. Pakuti välja idee materjali dosimeetriliste omaduste parandamiseks. Kuna Eu^{3+} toimib oksüdeerijana, tuleb leida mingi haruldane muldmetall lisandina, mis toimides kontrollitava taandajana võimaldaks reguleerida Eu^{2+} kogust kolmevalentse lisandi suhtes.

Energia salvestamise ja vabastamise mehhanism CaF_2:Mn korral on seotud pigem iooniliste kui elektron-aukprotsessidega. Esmalt toimub Mn^{2+} ergastamine ^6D ($3d^4$ 4s) ergastatud olekusse resonantse energiaülekande kaudu „kuumadelt“ eksitonidelt või elektron-aukpaaridelt termalisatsioonistaadiumis. Ergastatud Mn^{2+} on suurema ioonraadiusega ja nihutab kohalt ühe lähima fluoriidiaatomi. Selline mittekiirguslik energiaülekanne tekitab paaris F-ja H-tsentri (anioonvakantsi, mis on haaranud elektroni ja võrevahelise fluori). Võrevaheline fluor kas pöördub tagasi vakantsele kohale või naabruses oleva võrevahelise fluori juurde, mis toimib laengukompensaatorina Mn^{3+} juures (Mn moodustab CaF_2:Mn korral korrastatud klastreid mõlemas laenguolekus). Kaks võrevahelist fluoriidiaatomit moodustavad võrevahelise fluorimolekuli, mille stabiilsus sõltub tema elektronpilve kattumisest naaberaatomite omaga. Mida väiksem on Mn kontsentratsioon, seda väiksemad klastrid moodustuvad ja seda vähem jääb ruumi fluori molekulide jaoks. Temperatuuri tõusuga molekulid

dissotsieeruvad ja aatomid pöörduvad tagasi vakantsetele kohtadele. Rekombinatsiooniprotsessis vabanev energia kandub üle Mn^{2+}-ile, kust see esimesest ergastatud olekust $^4T_{1g}$ (^4G) kiirguslikult vabaneb, andes luminestsentsi. See mudel on kinnitatud TSL isotermilise kustumise kineetika mõõtmisega, mille kohaselt kvaasi-tsentrisisene protsess dosimeetrilise piigi aktivatsioonienergiaga 1,597eV on liiga suur CaF_2 jaoks, kuid on lähedane vaba F_2 molekuli dissotsiatsioonienergiale (1,606 eV). Samuti nii OSL stimulatsiooni kui kiirguslikult indutseeritud CaF_2:Mn neeldumisriba on lähedased fluori molekuli neeldumisribale. TSL kõvera simuleerimine arvutil andis väga kõrge tagasihaaramise tõenäosuse ($0{,}011s^{-1}$), mis takistab energia vabastamist optilise stimulatsiooniga, eriti toatemperatuuril. Peamiseks raskuseks CaF_2:Mn detektorite korral on asjaolu, et optimaalse TSL kõvera korral läheneb Mn kontsentratsioon tahke lahuse lagunemise lävele. Sisemiste redoksreaktsioonide tasakaaluga määratud Mn^{2+} ja Mn^{3+} vahekorda on raske kontrollida. Pakuti välja võimalus leida redoksomadustelt sobiv lantanoidioon keeruka lisandikompleksi korrastamiseks. Mn^{2+} osaleb energia salvestamise esimesel, ja energia vabanemise viimasel etapil, kolmevalentne lisand aga loob tingimused võrevahelise fluorimolekuli paigutumiseks.

Tahke lahuse moodustumise ajal toimuvte redoksreaktsioonide tõttu siseneb Mn $Li_2B_4O_7$ kristallvõresse kahel erineval positsioonil nii katioon kui anioon alamvõres. Sünteesi algetapil paikneb Mn^{3+} hapniku tetraeedris sarnaselt BO_4 struktuurile. Kõrgetemperatuuriline detektori paagutamine põhjustab Mn^{3+} osalise transformeerumise Mn^{2+}, eriti kõrgematel temperatuuridel. Pooled moodustunud Mn^{2+} ioonid lahkuvad tetraeedrist ja asendavad Li^+ laengu kompensatsiooniks tetraeedris oleva Mn^{2+} laengule. Nii moodustuvad isekompenseeritud Mn^{2+} paarid. Kuigi Mn^{2+} üldkogus temperatuuri tõusuga kasvab, jäävad B^{3+} ja Li^+ positsioonis olevate Mn^{2+} kogused omavahel võrdseks. Mõlemat tüüpi tsentrid on eristatavad nende luminestsentsi ja EPR spektrite järgi. Mn^{2+} paiknemine B^{3+} tetraeedrilises positsioonis tõestati ülipeenstruktuuri konstandi väärtuse järgi, mis vastab sellele Mn^{2+} jaoks BeO puhul, kus Mn^{2+} asendab Be^{2+} tetraeedrilises positsioonis. Võrreldes BeO juhuga on aga tetraeedrilised struktuurid $Li_2B_4O_7$ kristallvõres vähem jäigad tänu tetraeedreid siduvale sild-hapnikule. Kui ühes tetraeedris on Mn^{2+} paiknemas B^{3+} asemel, loob hapnik haardenivoo augu jaoks. Haardenivoo elektroni jaoks on seotud ekstra positiivse laenguga, mis on tekkinud Mn^{2+} paiknemisest Li^+ asemel. Sõltuvalt haardenivoode vahemaast pakuti välja kaks erinevat rekombinatsiooni mehhanismi. Neljast võimalikust positsioonist vaid kolm osalevad termoluminestsentsis. Lähem positsioon elektroni haaramiseks on just Mn^{2+} sisaldava tetraeeedri naabri – regulaarse tetaeedri hapniku tasandi taga. Auk aktiveeritakse termiliselt ja elektronpilvede kattumise järel kantakse energia üle Mn^{2+}-ile, mis paikneb B^{3+} positsioonis ja vabaneb punase luminestsentsina. Vastav termoluminestsentsi maksimum (335-345K) on puhta esimest järku kineetikaga, toimub tagasihaardeta ja ilma augu hüppamiseta. Aktivatsiooni

energia on 0,45eV, madalam, kui augu vabastamiseks vaja. Kui laengukandjad haardenivoodel paiknevad kaugematel positsioonidel, toimub energia vabanemine augu vabastamise järel energia ülekandega Mn^{2+}-ile, mis paikneb Li^{+} positsioonis. Kiirgus vabaneb oranži luminestsentsina, vastava TSL maksimumiga 470-510K. $Li_2B_4O_7$:Mn,Be korral on see termoluminestsentsi maksimum alla surutud ja moodustunud uus maksimum temperatuuride vahemikus 525-625K. Võrreldes $Li_2B_4O_7$:Mn moodustub sügavam auktsenter sildhapniku juures kui Be^{2+} asendab B^{3+}. Luminestsentskiirgus on mõlemal juhul seostatav üleminekuga $^4T_1$-$^6A_1$ Mn^{2+} deformeerunud tetraeedrilises ümbruses. Kineetika mõõtmise tulemusi tõlgendati mõlemal juhul $Li_2B_4O_7$:Mn ja $Li_2B_4O_7$:Mn,Be lihtsa kvaasi-tsentrisisese mudeli alusel, võttes arvesse aktivatsioonibarjääri olemasolu augu hüppamisele rekombinatsioonitsentri suunas. Vastavalt väljapakutud kristallstruktuuri arvestavale mudelile Mn lähedal haardunud elektron ei taga Mn^{2+} positiivse laengu täielikku varjestamist ning vastav kuloniline tõukejõud suurendab polaroni hüppamise aktivatsiooni energiat. Mõõdeti ka mõlema materjali $Li_2B_4O_7$:Mn ja $Li_2B_4O_7$:Mn,Be OSL stimulatsiooni ja kiirguslikult stimuleeritud neeldumise spektreid UV piirkonnas. Vastavad neeldumisribad korreleerusid stimulatsioonispektriga. OSL stimulatsiooni spekter oli nihutatud 30-40 nm pikemate lainepikkuste poole $Li_2B_4O_7$:Mn,Be korral. Jälgiti haardenivoode tühjendamist võimsa valgusdioodiga kiiritamisel. Efektiivne dosimeetrilise TSL signaali kustutamine nõuab täiendavat energiat augu hüppamise aktiveerimiseks. Saadud tulemused on kasulikud $Li_2B_4O_7$:Mn ja $Li_2B_4O_7$:Mn,Be rakendamisel OSL dosimeetrias.

Üldjuhul on hea salvestava luminofoori saamiseks tarvilikud lisandite redokstransformatsioonid tahke lahuse moodustumisel, mis viivad lähestikku paiknevate, kuid siiski lainefunktsioonidelt mittekattuvate erimärgiliste haardenivoode süsteemide formeerumisele. Kolm vaadeldud materjali demonstreerivad nende üldpõhimõtete rakendamise erijuhtumeid.

ACKNOWLEDGEMENTS

I would like to thank the University of Tartu and Institute of Chemistry for the support and interest of the present work. I would also like to thank my supervisors, senior researcher Dr Mikhail Danilkin and researcher Dr Mihkel Kerikmäe for the inspiration. I am very grateful for my family for understanding and letting me spend my time in lab. I would like to acknowledge the help of our research group of luminescence, specially researcher Aime Lust and senior researcher Viktor Seeman for fruitful discussions.

Finally I would like to thank the Graduate School on Functional Materials and Technologies (GSFMT), University of Tartu and Tallinn University of Technology, EU Social Funds project 1.2.0401.09-0079 for making this work possible.

PUBLICATIONS

CURRICULUM VITAE

I. Personal particulars

1. First and last name: **Arno Ratas**
2. Date of birth: May 17, 1952.
3. Citizenship: Estonia
4. Address: Pärna, Puhja county, Tartumaa 61302
   +372 55675217; arno.ratas@gmail.com
5. Current position: Tartu Vocational Centre, teacher

6. Education:

1970 – 1975 University of Tartu, M.Sc.(physics)
1995 – 1998 University of Tartu, an English teacher in-service training
2002 – 2005 University of Tartu, the teachers' professional
2004 – 2008 University of Tartu, Ph.D. student
2010 – 2012 University of Tartu, Ph.D. student (Chemistry)

7. Language skills: estonian, russian, english

8. Professional career:

2002 – to present Tartu Vocational Centre, teacher
2000 – 2002 Agrobiocentre, technologist
1994 – 1999 Ulila Basic School, teacher
1977 – 1992 University of Tartu, Chair of Analytical chemistry, researcher
1975 – 1977 Institut of Physics, engineer

II. Research and development work

1. Main fields of research
   Luminescence of solids, dosemetry and cathodoluminescence.
2. A list of publications:
   1. Arno Ratas, Mikhail Danilkin, Mihkel Kerikmäe, Aime Lust, Hugo Mändar, Viktor Seeman, Georg Slavin „$Li_2B_4O_7$:Mn for dosimetry applications: traps and mechanisms“ *Proc. Est. Acad. Sci.,* accepted for publication.
   2. M. Kerikmäe, M. Danilkin, I. Jaek, M. Must, A. Ots, L. Pung, E. Pärnoja, A. Ratas, V. Seeman, T. Tõnutare „ OSL and TSL interrelations in $SrSO_4$:Eu“ *Radiat. Meas.* 43 (2008) 559
   3. M. Danilkin, I. Jaek, M. Kerikmäe, A. Lust, H. Mändar, L. Pung, A. Ratas, V. Seeman, S. Klimonsky, V. Kuznetsov „Storage

mechanism and OSL-readout possibility of $Li_2B_4O_7$:Mn (TLD-800)“ *Radiat. Meas.* 43 (2008) 562

4. M. Danilkin, A. Lust, A. Ratas, V. Seeman, M. Kerikmäe „Afterglow kinetics and storage mechanism in CaF_2:Mn (TLD-400)“ *Radiat. Meas.* 43 (2008) 300
5. Mikhail Danilkin, Mihkel Kerikmäe, Aleksei Kirillov, Aime Lust, Arno Ratas, Lilli Paama, and Viktor Seeman „Thermoluminescent dosimeter $Li_2B_4O_7$:Mn,Si – a false-dose problem“ *Proc. Est. Acad. Sci. Chemistry*. 55 (2006) 123
6. Mikhail Danilkin, Aleksei Kirillov, Sergei Klimonsky, Vyacheslav Kuznetsov, Aime Lust, Hugo Mändar, Vladimir Nikiforov Arno Ratas, Aleksandr Ruchkin, Viktor Seeman „Magnetic manifestations of thermoluminescence exitation in CaF_2:Mn (TLD-400)“ *Radiat. Meas.* 42 (2007) 594
7. Ch.B. Luschik, I. Kuusmann, P.Liblik, G. Liidja, N.E. Luschik, V.G. Plekhanov, A. Ratas, T. Soovik „Edge luminescence of exitons in ionic crystals“ *Journal of Luminescence*, 11 (1976) 285

3. Other activities:
    1. Conference on Knowledge-based Materials and Technologies for Sustainable Chemistry; Tallinn, Estonia, 2005, poster presentation
    2. 15th Solid State Dosimetry Conference (SSD15), Delft, Netherlands, 2007, poster presentation

ELULOOKIRJELDUS

I. Üldandmed

1. Ees- ja perekonnanimi: **Arno Ratas**
2. Sünniaeg: 17. mai 1952.
3. Kodakondsus: Eesti
4. Aadress: Pärna talu, Puhja vald, Tartumaa 61302
   +372 55675217; arno.ratas@gmail.com
5. Praegune töökoht: Tartu Kutsehariduskeskus, õpetaja
6. Haridus:
   - 1970 – 1975 Tartu Ülikool, M.Sc.(füüsika)
   - 1995 – 1998 Tartu Ülikool, inglise keele õpetaja täienduskoolitus
   - 2002 – 2005 Tartu Ülikool, õpetajakoolituse kutseaasta
   - 2004 – 2008 Tartu Ülikool, doktoriõpe
   - 2010 – 2012 Tartu Ülikool doktoriõpe (keemia)
7. Teenistuskäik:
   - 2002 – praeguseni Tartu Kutsehariduskeskus, õpetaja
   - 2000 – 2002 EMPÜ Agrobiokeskus, tehnoloog
   - 1994 – 1999 Ulila Põhikool, õpetaja
   - 1977 – 1992 Tartu Ülikool, Analüütilise keemia kateeder, teadur
   - 1975 – 1977 TA Füüsika Instituut, insener
8. Keelteoskus: eesti, vene, inglise

II. Teaduslik ja arendustegevus

1. Peamised uurimisvaldkonnad: Tahkiste luminestsents ja selle rakendused. Katoodluminestsents, Luminestsentsdosimeetria
2. Publikatsioonide loetelu:
   1. Arno Ratas, Mikhail Danilkin, Mihkel Kerikmäe, Aime Lust, Hugo Mändar, Viktor Seeman, Georg Slavin „$Li_2B_4O_7$:Mn for dosimetry applications: traps and mechanisms“ *Proc. Est. Acad. Sci.,* accepted for publication.
   2. M. Kerikmäe, M. Danilkin, I. Jaek, M. Must, A. Ots, L. Pung, E. Pärnoja, A. Ratas, V. Seeman, T. Tõnutare „ OSL and TSL interrelations in $SrSO_4$:Eu“ *Radiat. Meas.* 45 (2010) 559

3. M. Danilkin, I. Jaek, M. Kerikmäe, A. Lust, H. Mändar, L. Pung, A. Ratas, V. Seeman, S. Klimonsky, V. Kuznetsov „Storage mechanism and OSL-readout possibility of $Li_2B_4O_7$:Mn (TLD-800)“ *Radiat. Meas.* 45 (2010) 562
4. M. Danilkin, A. Lust, A. Ratas, V. Seeman, M. Kerikmäe „Afterglow kinetics and storage mechanism in CaF_2:Mn (TLD-400)“ *Radiat. Meas.* 43 (2008) 300
5. Mikhail Danilkin, Mihkel Kerikmäe, Aleksei Kirillov, Aime Lust, Arno Ratas, Lilli Paama, and Viktor Seeman „Thermoluminescent dosimeter $Li_2B_4O_7$:Mn,Si – a false-dose problem“ *Proc. Est. Acad. Sci. Chemistry*. 55 (2006) 123
6. Mikhail Danilkin, Aleksei Kirillov, Sergei Klimonsky, Vyacheslav Kuznetsov, Aime Lust, Hugo Mändar, Vladimir Nikiforov Arno Ratas, Aleksandr Ruchkin, Viktor Seeman „Magnetic manifestations of thermoluminescence exitation in CaF_2:Mn (TLD-400)“ *Radiat. Meas.* 42 (2007) 594
7. Ch.B. Luschik, I. Kuusmann, P.Liblik, G. Liidja, N.E. Luschik, V.G. Plekhanov, A. Ratas, T. Soovik „Edge luminescence of exitons in ionic crystals“ Journal of Luminescence, 11 (1976) 285

3. Konverentsiettekanded:
    1. Conference on Knowledge-based Materials and Technologies for Sustainable Chemistry; Tallinn, Estonia, 2005, stendiettekanne
    2. 15th Solid State Dosimetry Conference (SSD15), Delft, Netherlands, 2007, stendiettekanne

DISSERTATIONES CHIMICAE UNIVERSITATIS TARTUENSIS

1. **Toomas Tamm.** Quantum-chemical simulation of solvent effects. Tartu, 1993, 110 p.
2. **Peeter Burk.** Theoretical study of gas-phase acid-base equilibria. Tartu, 1994, 96 p.
3. **Victor Lobanov.** Quantitative structure-property relationships in large descriptor spaces. Tartu, 1995, 135 p.
4. **Vahur Mäemets.** The ^{17}O and ^{1}H nuclear magnetic resonance study of H_2O in individual solvents and its charged clusters in aqueous solutions of electrolytes. Tartu, 1997, 140 p.
5. **Andrus Metsala.** Microcanonical rate constant in nonequilibrium distribution of vibrational energy and in restricted intramolecular vibrational energy redistribution on the basis of slater's theory of unimolecular reactions. Tartu, 1997, 150 p.
6. **Uko Maran.** Quantum-mechanical study of potential energy surfaces in different environments. Tartu, 1997, 137 p.
7. **Alar Jänes.** Adsorption of organic compounds on antimony, bismuth and cadmium electrodes. Tartu, 1998, 219 p.
8. **Kaido Tammeveski.** Oxygen electroreduction on thin platinum films and the electrochemical detection of superoxide anion. Tartu, 1998, 139 p.
9. **Ivo Leito.** Studies of Brønsted acid-base equilibria in water and non-aqueous media. Tartu, 1998, 101 p.
10. **Jaan Leis.** Conformational dynamics and equilibria in amides. Tartu, 1998, 131 p.
11. **Toonika Rinken.** The modelling of amperometric biosensors based on oxidoreductases. Tartu, 2000, 108 p.
12. **Dmitri Panov.** Partially solvated Grignard reagents. Tartu, 2000, 64 p.
13. **Kaja Orupõld.** Treatment and analysis of phenolic wastewater with microorganisms. Tartu, 2000, 123 p.
14. **Jüri Ivask.** Ion Chromatographic determination of major anions and cations in polar ice core. Tartu, 2000, 85 p.
15. **Lauri Vares.** Stereoselective Synthesis of Tetrahydrofuran and Tetrahydropyran Derivatives by Use of Asymmetric Horner-Wadsworth-Emmons and Ring Closure Reactions. Tartu, 2000, 184 p.
16. **Martin Lepiku.** Kinetic aspects of dopamine D_2 receptor interactions with specific ligands. Tartu, 2000, 81 p.
17. **Katrin Sak.** Some aspects of ligand specificity of P2Y receptors. Tartu, 2000, 106 p.
18. **Vello Pällin.** The role of solvation in the formation of iotsitch complexes. Tartu, 2001, 95 p.

19. **Katrin Kollist.** Interactions between polycyclic aromatic compounds and humic substances. Tartu, 2001, 93 p.
20. **Ivar Koppel.** Quantum chemical study of acidity of strong and superstrong Brønsted acids. Tartu, 2001, 104 p.
21. **Viljar Pihl.** The study of the substituent and solvent effects on the acidity of OH and CH acids. Tartu, 2001, 132 p.
22. **Natalia Palm.** Specification of the minimum, sufficient and significant set of descriptors for general description of solvent effects. Tartu, 2001, 134 p.
23. **Sulev Sild.** QSPR/QSAR approaches for complex molecular systems. Tartu, 2001, 134 p.
24. **Ruslan Petrukhin.** Industrial applications of the quantitative structure-property relationships. Tartu, 2001, 162 p.
25. **Boris V. Rogovoy.** Synthesis of (benzotriazolyl)carboximidamides and their application in relations with *N*- and *S*-nucleophyles. Tartu, 2002, 84 p.
26. **Koit Herodes.** Solvent effects on UV-vis absorption spectra of some solvatochromic substances in binary solvent mixtures: the preferential solvation model. Tartu, 2002, 102 p.
27. **Anti Perkson.** Synthesis and characterisation of nanostructured carbon. Tartu, 2002, 152 p.
28. **Ivari Kaljurand.** Self-consistent acidity scales of neutral and cationic Brønsted acids in acetonitrile and tetrahydrofuran. Tartu, 2003, 108 p.
29. **Karmen Lust.** Adsorption of anions on bismuth single crystal electrodes. Tartu, 2003, 128 p.
30. **Mare Piirsalu.** Substituent, temperature and solvent effects on the alkaline hydrolysis of substituted phenyl and alkyl esters of benzoic acid. Tartu, 2003, 156 p.
31. **Meeri Sassian.** Reactions of partially solvated Grignard reagents. Tartu, 2003, 78 p.
32. **Tarmo Tamm.** Quantum chemical modelling of polypyrrole. Tartu, 2003. 100 p.
33. **Erik Teinemaa.** The environmental fate of the particulate matter and organic pollutants from an oil shale power plant. Tartu, 2003. 102 p.
34. **Jaana Tammiku-Taul.** Quantum chemical study of the properties of Grignard reagents. Tartu, 2003. 120 p.
35. **Andre Lomaka.** Biomedical applications of predictive computational chemistry. Tartu, 2003. 132 p.
36. **Kostyantyn Kirichenko.** Benzotriazole – Mediated Carbon–Carbon Bond Formation. Tartu, 2003. 132 p.
37. **Gunnar Nurk.** Adsorption kinetics of some organic compounds on bismuth single crystal electrodes. Tartu, 2003, 170 p.
38. **Mati Arulepp.** Electrochemical characteristics of porous carbon materials and electrical double layer capacitors. Tartu, 2003, 196 p.

39. **Dan Cornel Fara.** QSPR modeling of complexation and distribution of organic compounds. Tartu, 2004, 126 p.
40. **Riina Mahlapuu.** Signalling of galanin and amyloid precursor protein through adenylate cyclase. Tartu, 2004, 124 p.
41. **Mihkel Kerikmäe.** Some luminescent materials for dosimetric applications and physical research. Tartu, 2004, 143 p.
42. **Jaanus Kruusma.** Determination of some important trace metal ions in human blood. Tartu, 2004, 115 p.
43. **Urmas Johanson.** Investigations of the electrochemical properties of polypyrrole modified electrodes. Tartu, 2004, 91 p.
44. **Kaido Sillar.** Computational study of the acid sites in zeolite ZSM-5. Tartu, 2004, 80 p.
45. **Aldo Oras.** Kinetic aspects of dATPαS interaction with $P2Y_1$ receptor. Tartu, 2004, 75 p.
46. **Erik Mölder.** Measurement of the oxygen mass transfer through the air-water interface. Tartu, 2005, 73 p.
47. **Thomas Thomberg.** The kinetics of electroreduction of peroxodisulfate anion on cadmium (0001) single crystal electrode. Tartu, 2005, 95 p.
48. **Olavi Loog.** Aspects of condensations of carbonyl compounds and their imine analogues. Tartu, 2005, 83 p.
49. **Siim Salmar.** Effect of ultrasound on ester hydrolysis in aqueous ethanol. Tartu, 2006, 73 p.
50. **Ain Uustare.** Modulation of signal transduction of heptahelical receptors by other receptors and G proteins. Tartu, 2006, 121 p.
51. **Sergei Yurchenko.** Determination of some carcinogenic contaminants in food. Tartu, 2006, 143 p.
52. **Kaido Tämm.** QSPR modeling of some properties of organic compounds. Tartu, 2006, 67 p.
53. **Olga Tšubrik.** New methods in the synthesis of multisubstituted hydrazines. Tartu. 2006, 183 p.
54. **Lilli Sooväli.** Spectrophotometric measurements and their uncertainty in chemical analysis and dissociation constant measurements. Tartu, 2006, 125 p.
55. **Eve Koort.** Uncertainty estimation of potentiometrically measured ph and pK_a values. Tartu, 2006, 139 p.
56. **Sergei Kopanchuk.** Regulation of ligand binding to melanocortin receptor subtypes. Tartu, 2006, 119 p.
57. **Silvar Kallip.** Surface structure of some bismuth and antimony single crystal electrodes. Tartu, 2006, 107 p.
58. **Kristjan Saal.** Surface silanization and its application in biomolecule coupling. Tartu, 2006, 77 p.
59. **Tanel Tätte.** High viscosity $Sn(OBu)_4$ oligomeric concentrates and their applications in technology. Tartu, 2006, 91 p.

60. **Dimitar Atanasov Dobchev**. Robust QSAR methods for the prediction of properties from molecular structure. Tartu, 2006, 118 p.
61. **Hannes Hagu**. Impact of ultrasound on hydrophobic interactions in solutions. Tartu, 2007, 81 p.
62. **Rutha Jäger.** Electroreduction of peroxodisulfate anion on bismuth electrodes. Tartu, 2007, 142 p.
63. **Kaido Viht.** Immobilizable bisubstrate-analogue inhibitors of basophilic protein kinases: development and application in biosensors. Tartu, 2007, 88 p.
64. **Eva-Ingrid Rõõm.** Acid-base equilibria in nonpolar media. Tartu, 2007, 156 p.
65. **Sven Tamp.** DFT study of the cesium cation containing complexes relevant to the cesium cation binding by the humic acids. Tartu, 2007, 102 p.
66. **Jaak Nerut.** Electroreduction of hexacyanoferrate(III) anion on Cadmium (0001) single crystal electrode. Tartu, 2007, 180 p.
67. **Lauri Jalukse.** Measurement uncertainty estimation in amperometric dissolved oxygen concentration measurement. Tartu, 2007, 112 p.
68. **Aime Lust.** Charge state of dopants and ordered clusters formation in CaF_2:Mn and CaF_2:Eu luminophors. Tartu, 2007, 100 p.
69. **Iiris Kahn**. Quantitative Structure-Activity Relationships of environmentally relevant properties. Tartu, 2007, 98 p.
70. **Mari Reinik.** Nitrates, nitrites, N-nitrosamines and polycyclic aromatic hydrocarbons in food: analytical methods, occurrence and dietary intake. Tartu, 2007, 172 p.
71. **Heili Kasuk.** Thermodynamic parameters and adsorption kinetics of organic compounds forming the compact adsorption layer at Bi single crystal electrodes. Tartu, 2007, 212 p.
72. **Erki Enkvist.** Synthesis of adenosine-peptide conjugates for biological applications. Tartu, 2007, 114 p.
73. **Svetoslav Hristov Slavov**. Biomedical applications of the QSAR approach. Tartu, 2007, 146 p.
74. **Eneli Härk.** Electroreduction of complex cations on electrochemically polished Bi(*hkl*) single crystal electrodes. Tartu, 2008, 158 p.
75. **Priit Möller.** Electrochemical characteristics of some cathodes for medium temperature solid oxide fuel cells, synthesized by solid state reaction technique. Tartu, 2008, 90 p.
76. **Signe Viggor.** Impact of biochemical parameters of genetically different pseudomonads at the degradation of phenolic compounds. Tartu, 2008, 122 p.
77. **Ave Sarapuu.** Electrochemical reduction of oxygen on quinone-modified carbon electrodes and on thin films of platinum and gold. Tartu, 2008, 134 p.
78. **Agnes Kütt.** Studies of acid-base equilibria in non-aqueous media. Tartu, 2008, 198 p.

79. **Rouvim Kadis.** Evaluation of measurement uncertainty in analytical chemistry: related concepts and some points of misinterpretation. Tartu, 2008, 118 p.
80. **Valter Reedo.** Elaboration of IVB group metal oxide structures and their possible applications. Tartu, 2008, 98 p.
81. **Aleksei Kuznetsov.** Allosteric effects in reactions catalyzed by the cAMP-dependent protein kinase catalytic subunit. Tartu, 2009, 133 p.
82. **Aleksei Bredihhin.** Use of mono- and polyanions in the synthesis of multisubstituted hydrazine derivatives. Tartu, 2009, 105 p.
83. **Anu Ploom.** Quantitative structure-reactivity analysis in organosilicon chemistry. Tartu, 2009, 99 p.
84. **Argo Vonk.** Determination of adenosine A_{2A}- and dopamine D_1 receptor-specific modulation of adenylate cyclase activity in rat striatum. Tartu, 2009, 129 p.
85. **Indrek Kivi.** Synthesis and electrochemical characterization of porous cathode materials for intermediate temperature solid oxide fuel cells. Tartu, 2009, 177 p.
86. **Jaanus Eskusson.** Synthesis and characterisation of diamond-like carbon thin films prepared by pulsed laser deposition method. Tartu, 2009, 117 p.
87. **Marko Lätt.** Carbide derived microporous carbon and electrical double layer capacitors. Tartu, 2009, 107 p.
88. **Vladimir Stepanov.** Slow conformational changes in dopamine transporter interaction with its ligands. Tartu, 2009, 103 p.
89. **Aleksander Trummal.** Computational Study of Structural and Solvent Effects on Acidities of Some Brønsted Acids. Tartu, 2009, 103 p.
90. **Eerold Vellemäe.** Applications of mischmetal in organic synthesis. Tartu, 2009, 93 p.
91. **Sven Parkel.** Ligand binding to 5-HT_{1A} receptors and its regulation by Mg^{2+} and Mn^{2+}. Tartu, 2010, 99 p.
92. **Signe Vahur.** Expanding the possibilities of ATR-FT-IR spectroscopy in determination of inorganic pigments. Tartu, 2010, 184 p.
93. **Tavo Romann**. Preparation and surface modification of bismuth thin film, porous, and microelectrodes. Tartu, 2010, 155 p.
94. **Nadežda Aleksejeva.** Electrocatalytic reduction of oxygen on carbon nanotube-based nanocomposite materials. Tartu, 2010, 147 p.
95. **Marko Kullapere.** Electrochemical properties of glassy carbon, nickel and gold electrodes modified with aryl groups. Tartu, 2010, 233 p.
96. **Liis Siinor.** Adsorption kinetics of ions at Bi single crystal planes from aqueous electrolyte solutions and room-temperature ionic liquids. Tartu, 2010, 101 p.
97. **Angela Vaasa.** Development of fluorescence-based kinetic and binding assays for characterization of protein kinases and their inhibitors. Tartu 2010, 101 p.

98. **Indrek Tulp.** Multivariate analysis of chemical and biological properties. Tartu 2010, 105 p.
99. **Aare Selberg.** Evaluation of environmental quality in Northern Estonia by the analysis of leachate. Tartu 2010, 117 p.
100. **Darja Lavõgina.** Development of protein kinase inhibitors based on adenosine analogue-oligoarginine conjugates. Tartu 2010, 248 p.
101. **Laura Herm.** Biochemistry of dopamine D_2 receptors and its association with motivated behaviour. Tartu 2010, 156 p.
102. **Terje Raudsepp.** Influence of dopant anions on the electrochemical properties of polypyrrole films. Tartu 2010, 112 p.
103. **Margus Marandi.** Electroformation of Polypyrrole Films: *In-situ* AFM and STM Study. Tartu 2011, 116 p.
104. **Kairi Kivirand.** Diamine oxidase-based biosensors: construction and working principles. Tartu, 2011, 140 p.
105. **Anneli Kruve.** Matrix effects in liquid-chromatography electrospray mass-spectrometry. Tartu, 2011, 156 p.
106. **Gary Urb.** Assessment of environmental impact of oil shale fly ash from PF and CFB combustion. Tartu, 2011, 108 p.
107. **Nikita Oskolkov.** A novel strategy for peptide-mediated cellular delivery and induction of endosomal escape. Tartu, 2011, 106 p.
108. **Dana Martin.** The QSPR/QSAR approach for the prediction of properties of fullerene derivatives. Tartu, 2011, 98 p.
109. **Säde Viirlaid.** Novel glutathione analogues and their antioxidant activity. Tartu, 2011, 106 p.
110. **Ülis Sõukand.** Simultaneous adsorption of Cd^{2+}, Ni^{2+}, and Pb^{2+} on peat. Tartu, 2011, 124 p.
111. **Lauri Lipping.** The acidity of strong and superstrong Brønsted acids, an outreach for the "limits of growth": a quantum chemical study. Tartu, 2011, 124 p.
112. **Heisi Kurig.** Electrical double-layer capacitors based on ionic liquids as electrolytes. Tartu, 2011, 146 p.
113. **Marje Kasari.** Bisubstrate luminescent probes, optical sensors and affinity adsorbents for measurement of active protein kinases in biological samples. Tartu, 2012, 126 p.
114. **Kalev Takkis.** Virtual screening of chemical databases for bioactive molecules. Tartu, 2012, 122 p.
115. **Ksenija Kisseljova**. Synthesis of aza-β^3-amino acid containing peptides and kinetic study of their phosphorylation by protein kinase A. Tartu, 2012, 104 p.
116. **Riin Rebane.** Advanced method development strategy for derivatization LC/ESI/MS. Tartu, 2012, 184 p.

117. **Vladislav Ivaništšev.** Double layer structure and adsorption kinetics of ions at metal electrodes in room temperature ionic liquids. Tartu, 2012, 128 p.
118. **Irja Helm.** High accuracy gravimetric Winkler method for determination of dissolved oxygen. Tartu, 2012, 139 p.
119. **Karin Kipper.** Fluoroalcohols as Components of LC-ESI-MS Eluents: Usage and Applications. Tartu, 2012, 164 p.